Modeling and Applications of High-speed VCSEL-MMF Links for Next-generation Data Centers

Shanglin Li

Department of Electrical & Computer Engineering
McGill University
Montréal, Québec, Canada

February, 2022

A thesis submitted to McGill University in partial fulfillment of the requirements of the degree of

Doctor of Philosophy

Abstract

Recently, the fast development of cloud computing, big data, and Internet of Things (IoT) puts higher demands on high-speed data center communications. Vertical-cavity surface-emitting laser (VCSEL)-multimode fiber (MMF) links dominate the interconnect within the data center because of their low cost and high energy efficiency. Next-generation 800 Gb/s and 1.6 Tb/s VCSEL based MMF links have been proposed by IEEE 802.3 Ethernet Working Group, while 200 G and 400 G Ethernet standards are currently in use.

This thesis presents an accurate and efficient system-level VCSEL-MMF link model. Then, analytical expressions for power coupling coefficients into graded-index fibers are derived, facilitating the calculation of the mode power distribution in the aforementioned model. Based on the model, a mode partition noise (MPN) mitigation method is investigated by optimizing the beam launch condition into the MMF. These contributions are detailed as follows.

My first work is to propose a versatile compact equivalent circuit model for the multiple-quantum-well (MQW) VCSEL. The dynamics of carriers and photons are analyzed with comprehensive rate equations of the MQW VCSEL, which are strongly dependent on the number of quantum wells. To speed up the simulation, these comprehensive rate equations are then manipulated into a simplified set of rate equations. Therefore, the number of equations and extracted parameters is significantly reduced, which improves the calculation efficiency of the VCSEL model.

Secondly, a spectral-dependent electronic-photonic model of high-speed VCSEL-MMF links is built. In this system-level model, five modules are included: 1) the VCSEL; 2) the coupling from the VCSEL to the MMF; 3) the MMF transmission link; 4) the coupling from the MMF to the photodetector (PD); and 5) the PD. The split-step small-segment method simulates the signal evolution over the MMF link based on the concept of fiber mode groups. The proposed model, which is validated by a 25 Gbps NRZ transmission experiment, also analyzes the influence of the launch conditions on the mode power distribution in the fiber.

As the third contribution of my thesis, the closed-form analytical expressions of power coupling coefficients into the graded-index fiber are derived for the key launch conditions—central launch, offset launch, tilted launch, and generalized launch, which avoids the heavy numerical computation of the conventional numerical method. With analytical expressions, the calculation time is reduced by six orders of magnitude for the low-order fiber modes and at least four orders of magnitude for the high-order fiber modes.

At last, with the above-mentioned VCSEL-MMF model, a mode-partition-noise (MPN) mitigation method is realized by tuning the launch condition. This idea is validated using the simulation and measurement, respectively. In the simulation, the MPN dependence on the mode power distribution is theoretically assessed. After that, the MPN suppression is experimentally observed from the frequency and time domain. The technique efficiently improves the transmission performance of high-speed VCSEL-MMF links, reducing the complexity of the equalizer and forward error correction (FEC) algorithms.

Abrégé

Récemment, le développement rapide de l'informatique en nuage, des mégadonnées et de l'Internet des objets (IoT) impose des exigences plus élevées sur les communications à haut débit des centres de données. Les liaisons laser à cavité verticale émettant par la surface (VCSEL)-fibre multimode (MMF) dominent l'interconnexion au sein du centre de données en raison de leur faible coût et de leur efficacité énergétique élevée. Les nouvelles générations de liaisons MMF à 800 Gbps et 1,6 Tbps VCSEL ont été proposées par le groupe de travail Ethernet IEEE 802.3, tandis que les normes Ethernet 200 G et 400 G sont actuellement utilisées.

Cette thèse présente d'abord un modèle de lien VCSEL-MMF précis et efficace au niveau du système. Ensuite, des expressions analytiques pour les coefficients de couplage de puissance dans les fibres à gradient d'indice sont dérivées, facilitant le calcul de la distribution de puissance de mode dans le modèle susmentionné. Basée sur ce modèle, une méthode d'atténuation du bruit de partition de mode (MPN) est étudiée en optimisant la condition de lancement du faisceau dans le MMF. Ces contributions sont détaillées comme suit.

Ma première contribution a été de proposer un modèle de circuit équivalent compact et polyvalent pour le VCSEL à puits quantiques multiples (MQW). La dynamique des porteurs et des photons est analysée avec des équations de vitesse complètes du MQW VCSEL, qui dépendent fortement du nombre de puits quantiques. Pour accélérer la simulation, ces équations de taux complètes sont ensuite dérivées en un ensemble simplifié d'équations de taux. Par conséquent, le nombre d'équations et de paramètres extraits est considérablement réduit, ce qui améliore l'efficacité de calcul du modèle VCSEL.

Deuxièmement, nous développons un modèle électro-photonique dépendant du spectre des liaisons VCSEL-MMF à grande vitesse. Dans ce modèle, cinq modules sont inclus : 1) le VCSEL ; 2) le couplage du VCSEL au MMF ; 3) la liaison de transmission MMF ; 4) le couplage du MMF au photodétecteur (PD) ; et 5) le PD. La méthode de segments à pas fractionnés simule l'évolution du signal sur la liaison MMF sur la base du concept de groupes de modes fibre. Le modèle proposé et validé par une expérience de transmission NRZ à 25 Gbps analyse également l'influence des conditions de lancement sur la distribution de puissance de mode dans la fibre.

Pour la troisième contribution de ma thèse, les expressions analytiques de forme fermée des coefficients de couplage de puissance dans la fibre à gradient d'indice sont dérivées pour les conditions de lancement clés suivantes — lancement central, lancement décalé, lancement incliné et lancement généralisé, ce qui évite le calcul numérique lourd de la méthode numérique classique. Avec des expressions analytiques, le temps de calcul est réduit de six ordres de grandeur pour les modes fibre d'ordre faible et d'au moins quatre ordres de grandeur pour les modes fibre d'ordre élevé.

Enfin, avec le modèle VCSEL-MMF mentionné ci-dessus, une méthode d'atténuation du bruit de partition de mode (MPN) est réalisée en ajustant la condition de lancement. Je valide cette idée en utilisant respectivement la simulation et la mesure. Dans la simulation, la dépendance du MPN en fonction de la distribution de puissance de mode est évaluée théoriquement. Après cela, la suppression MPN est observée expérimentalement à partir du domaine fréquentiel et temporel. La technique améliore efficacement les performances de transmission des liaisons VCSEL-MMF à grande vitesse, réduisant la complexité de l'égaliseur et des algorithmes de correction d'erreur.

Acknowledgements

First of all, I would like to express my sincere and utmost gratitude to my supervisor, Prof. Odile Liboiron-Ladouceur for supporting my Ph.D. study at McGill University. As a knowledgeable scientist in the field of optics and photonics, she always gives me very constructive guidance and advice to keep my research on a correct direction. As leader of the Photonic DataCom Team, she makes me feel the warmth of home during the five years of studying in the McGill Photonic DataCom Team.

Second, I would like to thank my Ph.D. supervisory committee, Prof. Lawrence Chen and Prof. Dennis Giannacopoulos, for the insightful comments on my research. I also acknowledge all professors from the Photonic Systems Group for their kind help in the use of experimental equipment.

Next, I would like to thank Dr. Mohammadreza Sanadgol Nezami, a Postdoc fellow in the team, for numerous discussions about my research and Smiths Interconnect Canada Inc. for providing me VCSEL chips. The team members really help me a lot since I joined the Photonic DataCom Team. Here, I would like to extend my thanks to Hassan Rahbardar Mojaver, Bahaa Radi, Guowu Zhang, Ajaypal Singh Dhillon, and Shubhankar Mishra.

Finally, a heartfelt appreciation goes to my parents and my wife. Their support makes me full of energy all the time during the journey towards the Ph.D. degree. Thank you, Dad, Mom and Rita.

Contents

List of Figures

List of Tables

List of Acronyms

BER	Bit error rate
B2B	Back-to-back
CCD	Charge-coupled device
CMOS	Complementary metal-oxide semiconductor
FEC	Forward error correction
GI	Graded-index
ISI	Inter-symbol interference
LP	Linearly polarized
MCG	Multi-core fiber
MDM	Mode division multiplexing
MGDM	Mode group division multiplexing
MPD	Mode power distribution
MPN	Mode partition noise
MQW	Multiple quantum well

NRZ	Non-return-to-zero
OAM	Orbital angular momentum
OSC	Oscilloscope
PCC	Power coupling coefficient
PD	Photodetector
PPG	Pulse pattern generator
QW	Quantum well
RI	Refrative index
RIN	Relative intensity noise
RMS	Root-mean-square
SCH	Heterostructure
SDM	Spatial division multiplexing
SLM	Spatial light modulator
SNR	Signal-to-noise ratio
SWDM	short wavelength division multiplexing

TDR	Time-domain reflectometer
VCSEL	Vertical cavity surface emitting laser
WKB	Wentzel-Kramers-Brillouin

Chapter 1

Introduction

This Ph.D. dissertation includes theoretical and experimental research contributions. In this chapter, Section 1.1 explains the motivation of this thesis. After that, the thesis objectives are detailed in Section 1.2. Section 1.3 enumerates the contributions included in this thesis as well as the peer-reviewed publications during my Ph.D. study. Furthermore, the thesis structure is summarized in Section 1.4.

1.1 Motivation

The Internet applications, such as streaming video, cloud computing, and big data, have created a fast-growing need for datacenter infrastructures. Based on the forecast by Cisco [1], the global IP traffic will reach 4.8 zettabytes per year by 2022 and have a three-fold increase from 2017 to 2022. Therefore, next-generation high-speed data center systems are required to support such a large-scale traffic. The traffic staying inside the data center occupies 85% of the total datacenter traffic [2]. Thus, the intra-datacenter high-speed link is vitally essential to transmit such a high capacity. Due to low cost and high power efficiency, vertical-cavity surface-emitting laser (VCSEL)-multimode fiber (MMF) interconnects are widely utilized in over 85% of short-reach datacenter links [3].

Several techniques have been proposed to improve the transmitted data rate over the VCSEL-MMF link. First, the VCSEL bandwidth and the MMF performance are enhanced to support such a high-speed transmission. The bandwidth of the VCSEL has reached above 30 GHz [4], and MMF has evolved into the fifth generation (i.e., OM-5 MMF) with an effective modal bandwidth of 4700 MHz·km. Second, some channel multiplexing schemes, such as short wavelength division multiplexing [5], mode group division multiplexing [6], and spatial division multiplexing [7], are proposed to increase the transmission capacity by using multiple channels. In addition, digital signal processing techniques and advanced modulation formats are also utilized to improve the transmission performance. In application scenarios of short-reach VCSEL-MMF interconnects, the cost and energy efficiency play a vital role and must be considered carefully. Considering mode selective excitation has superior performances in cost and power consumption, it is exceptionally promising and potential to optimize the MMF-VCSEL link.

The modeling and simulation of VCSELs and VCSEL-based MMF links have attracted increasing research interest from industry and academia in design, test and optimization of next-generation high-speed interconnects since 1990s. In particular, P. V. Mena proposed a comprehensive VCSEL model [8] and a simple rate-equation-based thermal VCSEL model [9]. In addition, a rate-equation-based model of asymmetric multiple-quantum-well lasers was proposed in [10]. In recent years, researchers have presented several advanced VCSEL models to provide high-accuracy simulation. For example, a large-signal equivalent circuit VCSEL model, realized in Keysight Advanced Design System, showed a satisfactory agreement between simulation and experimental measurement [11]. In addition, based on the measured VCSEL small-signal response and RIN spectra, the parameters of the rate-equation model were extracted using a genetic algorithm [12]. Moreover, a VCSEL-MMF link model was developed, consisting of a VCSEL model, an MMF model, and a receiver model [13], and the measured bit-error-rate (BER) results validated the link model with the transmission data rate of 10 Gbps.

To meet the requirements of next-generation high-speed VCSEL-MMF interconnects, a comprehensive link model with high accuracy and short computation time is expected. Designers and engineers can mimic the link transmission performance using the proposed model and do not need to implement complicated on-site measurements. Additionally, with this advanced model, the technique to improve the transmission capacity is explored by tuning the launch condition between the VCSEL and the MMF. The launch-condition-tuning technique shows advantages of low power consumption and easy implementation over other methods, like digital signal processing.

1.2 Thesis objectives

The first objective of this thesis is to build a reliable modeling platform for the VCSEL-MMF link. More specifically, the model is focused on five essential parts of the VCSEL-MMF link to realize highly accurate and efficient simulation:

- a compact VCSEL model insensitive to the number of the quantum wells;
- a VCSEL-MMF-coupling model showing the influence of the launch condition on fiber mode power distribution;
- an MMF model based on the concept of mode groups rather than modes;
- an MMF-PD-coupling module considering the beam diffraction;
- a PD model with noise effects.

The VCSEL model is expected to accommodate a flexible number of quantum wells, allowing the freedom to simulate an arbitrary VCSEL in the system-oriented opto-electronic simulation platform. The VCSEL-MMF-coupling model reflects the beam coupling from the laser source to the MMF input surface considering the diameter difference between the VCSEL active region and the MMF core. The MMF model investigates the modal and chromatic effects on signal integrity. The MMF-PD-coupling model discusses beam diffraction in the free space. The PD model explores the equivalent circuit model and analyzes the noise effects inside the photodetector. To this end, an advanced equivalent circuit model of the multiple-quantum-well (MQW) VCSEL is proposed and detailed [14]. Afterward, a comprehensive spectral-dependent electronic-photonic VCSEL-MMF link model is presented [15].

In the model platform, the calculation of coupling coefficients adopts the numerical method to obtain accurate solutions. Unfortunately, the conventional numerical method, such as the finite difference method, takes much time to compute. Therefore, the second objective in this thesis is to derive analytical expressions for coupling coefficients into graded-index fibers with launch conditions of center launch, offset launch, tilt launch and generalized launch.

Mode partition noise (MPN) originates from mode competition and performs as low-frequency relative intensity noise after a dispersive link. Unfortunately, conventional equalization techniques enhance MPN due to nonlinearity and randomness of the noise. Although some techniques have been presented to mitigate MPN, these schemes typically require new components, increasing the cost of the short-reach transmission. Therefore, as the third objective, the launch-condition-tuning method is utilized to mitigate MPN.

To sum up, these objectives are summarized below along with the outcomes:

- Develop a spectral-dependent electronic-photonic model of high-speed VCSEL-MMF links.
    - Developed an advanced and compact high-efficient equivalent circuit model for

    the multi-quantum-well VCSEL with the noise included.
  - Developed a complete VCSEL-MMF link model from the view of mode groups, which significantly reduces the scale of the matrix calculation.
  - Obtained analytical expressions for the coupling coefficients between the Laguerre-Gaussian beams and the MMF linearly-polarized modes.

- Implement measurement based on the VCSEL-MMF link to validate and apply the proposed model.
  - A 25 Gbps VCSEL-MMF link transmission is performed to validate the proposed VCSEL-MMF link model.
  - Mode partition noise is mitigated by optimizing the beam launch condition at the fiber input surface.

1.3 Claim of Originality

This Ph.D. dissertation aims to provide a complete and efficient VCSEL-MMF link model, allowing designers and researchers to develop and optimize the VCSEL-based MMF link. With the proposed model, a launch-condition-tuning method is presented to suppress mode partition noise. The contributions are detailed below.

- A compact equivalent circuit model with noise effects is presented for high-speed MQW VCSELs. The model comprehensively accounts for the carrier and photons dynamisms of a MQW structure, which includes separate confinement SCH layers, barrier layers, and quantum well layers. The proposed model is generalized to various VCSEL designs and accommodates a flexible number of quantum wells. Experimental validation of the model is performed at 25 Gbps with a self-wire-bonded 850 nm VCSEL. This work has been published as a journal paper in Applied Sciences [14].

- Spectral-dependent electronic-photonic modeling of VCSEL-MMF links is presented for next-generation high-speed interconnects. The beam coupling processes between the VCSEL and the MMF and between the MMF and the PD are discussed, with spectral-dependent three-dimensional launch conditions analyzed. The model accounts for fiber effects on the transmission performance, specifically modal attenuation, dispersion, mode mixing, and mode partition noise. An advanced split-step small-segment (4-S) method simulates the signal evolution over the MMF with high accuracy and efficiency. Experimental validation at 25 Gbps confirms the high accuracy of the VCSEL-MMF link model. The model reveals that larger radial offsets can further excite lower-order mode groups reducing the power distributed to higher-order groups when a tilted beam couples to the input fiber facet. With an optimized misalignment launch, the modal bandwidth is greatly improved by 3.8-fold compared to the conventional center launch. The model helps determine the optimum launch condition to improve link performance metrics such as the transmission reach. This work has been published as a journal paper in Optics Express [15].

- The closed-form analytical expressions of the power coupling coefficients are derived for a Laguerre-Gaussian beam coupled into a graded-index (GI) fiber with either central, offset, or tilted launch. The expressions are further generalized to an arbitrary launching condition with the radial offset and the three-dimension angular tilt simultaneously. The analytical results are in good agreement with the numerical ones and can be applied to manufactured graded-index multimode fibers with an index exponent parameter from 1.8 to 2.2. The largest time cost using the derived analytical expressions is 10 ms; thus the computation time shortens by at least a four-order of magnitude compared to 20 s for the conventional numerical method. This work has been published as a journal paper in IEEE Journal of Lightwave Technology [16].
- The multimode characteristics of vertical cavity surface emitting laser (VCSEL) sources lead to mode partition noise (MPN), impairing high-speed multimode fiber (MMF) links. A low-cost and straightforward MPN mitigation scheme is proposed by optimizing the VCSEL-MMF launch condition. The dependence of MPN on launch conditions is theoretically assessed. Simulation shows that the mode power redistribution induced by rearranging the launch condition has excellent potential to reduce MPN. Experiments are carried out to demonstrate the MPN reduction. By using a 15-μm radial offset between the VCSEL and the MMF, efficient noise suppression is observed in frequency and time domains. The work has been published

as a journal paper in IEEE Photonics Technology Letters [17].

The main contents of this thesis are published in four journal articles [14–17] and detailed in Chapters 3 to 6, respectively. The following is my list of publications and contributions. In addition, four conference papers not related to this thesis are published as the first author or co-author [18–21].

Published journal papers:

[14] S. Li, M. S. Nezami, D. Rolston, and O. Liboiron-Ladouceur, "A compact high-efficient equivalent circuit model of multi-quantum-well vertical-cavity surface-emitting lasers for high-speed interconnects,"Applied Sciences, vol. 10, no. 11, pp. 1–13, 2020.

S. Li: proposed the idea, modelled the VCSEL, performed the validation experiment, and wrote the draft.

M. S. Nezami: performed the validation experiment.

D. Rolston: provided the measurement device, and helped revise the manuscript.

O. Liboiron-Ladouceur: supervised the project and funding, and reviewed the manuscript.

[15] S. Li, M. S. Nezami, S. Mishra, and O. Liboiron-Ladouceur, "Spectral-dependent electronic-photonic modeling of high-speed VCSEL-MMF links for optimized launch conditions,"Optics Express, vol. 29, no. 2, pp. 2738–2756, 2021.

S. Li: proposed the idea, modelled the VCSEL-MMF link, performed the validation experiment, and wrote the draft.

M. S. Nezami: assisted with the proposal and experimental measurement.

S. Mishra: assisted with the manuscript revision.

O. Liboiron-Ladouceur: supervised the project and funding, and reviewed the manuscript.

[16] S. Li, M. S. Nezami, and O. Liboiron-Ladouceur, "Analytical expressions for power coupling coefficients into graded-index fibers with generalized beam launch conditions,"Journal of Lightwave Technology, vol. 39, no. 22, pp. 7259-7273, 2021.

S. Li: proposed the idea, derived the analytical expressions, wrote the script, and drafted the manuscript.

M. S. Nezami: assisted with the manuscript revision.

O. Liboiron-Ladouceur: supervised the project and funding, and reviewed the manuscript.

[17] S. Li, M. S. Nezami, and O. Liboiron-Ladouceur, "Mitigation of mode partition noise in VCSEL-MMF links by optimizing launch conditions,"IEEE Photonics Technology Letters, vol. 33, no. 23, pp. 1313–1316, 2021.

S. Li: proposed the idea, ran the simulation, performed the experiment, and wrote the draft.

M. S. Nezami: assisted with the measurement.

O. Liboiron-Ladouceur: supervised the project and funding, and reviewed the manuscript.

Published papers not included in this thesis:

[18] S. Li, M. S. Nezami, B. Bourouf, D. Rolston, and O. Liboiron-Ladouceur, "A Verilog-A based VCSEL model for next generation high-speed interconnects," in 2019 Photonics North (PN), vol. CFP1909V-ART, pp. 1–1, 2019.

S. Li: proposed the idea, modelled the VCSEL, performed the experiment, wrote the draft, and made an oral presentation.

M. S. Nezami: assisted with the model design.

B. Bourouf: assisted with the model design.

D. Rolston: provided the measurement devices, and helped revise the manuscript.

O. Liboiron-Ladouceur: supervised the project and funding, and reviewed the manuscript.

[19] S. Li, M. S. Nezami, and O. Liboiron-Ladouceur, "Reach extension in short-reach VCSEL-MMF interconnects using a coupling-weighted approach," in 2020 IEEE Photonics Conference (IPC), pp. 1–2, 2020.

S. Li: proposed the idea, performed the experiment, wrote the draft, and made an oral presentation.

M. S. Nezami: assisted with the experimental measurement.

O. Liboiron-Ladouceur: supervised the project and funding, and reviewed the manuscript.

[20] S. Li, H. R. Mojaver, and O. Liboiron-Ladouceur, “Tilted-beam-enabled optical equalization for PAM-4 transmission in VCSEL-MMF links,” in 2021 OSA Advanced Photonics Congress(APC), pp. 1–2, 2021.

S. Li: proposed the idea, performed the experiment, wrote the draft, and made an oral presentation.

H. R. Mojaver: assisted with the experimental measurement.

O. Liboiron-Ladouceur: supervised the project and funding, and reviewed the manuscript.

[21] H. R. Mojaver, S. Li, V. Tolstikhin, K.-W. Leong, and O. Liboiron-Ladouceur, “High radix SOA-based lossless optical switch prototyping for 25 GBaud PAM4 transmission in modern intra-datacenter applications,” in 2021 Optical Fiber Communications Conference and Exhibition (OFC), pp. 1–3, 2021.

H. R. Mojaver: proposed the idea, performed the experiment, wrote the draft, and made an oral presentation.

S. Li: assisted with the measurement.

V. Tolstikhin: assisted with the paper revision.

K.-W. Leong: assisted with the paper revision.

O. Liboiron-Ladouceur: supervised the project and funding, and reviewed the manuscript.

1.4 Thesis Organization

The thesis is organized as follows. Chapter 2 reviews the background knowledge for the VCSEL-MMF link. Some advanced techniques to improve the transmission performance are introduced. Chapter 3 presents an advanced MQW VCSEL model based on the rate equations. Compared to the conventional MQW VCSEL model, the scale of the rate-equation set is significantly reduced, resulting in high computation efficiency. Chapter 4 reports a spectral-dependent electronic-photonic VCSEL-MMF link model, which is validated using a 25 Gbps NRZ transmission experiment. Measured eye diagrams and bit error rates show good agreement with the simulation. In Chapter 5, closed-form analytical expressions are derived for coupling coefficients into the multimode fiber with the launch conditions of the central launch, the offset launch, the tilted launch, and the generalized launch. The analytical expressions help qualitative understanding of the coupling mechanisms and parametric dependencies. Additionally, the analytical expressions avoid heavy numerical computations leading to significantly reduced computation time. Chapter 6 exploits a launch-condition-tuning method to mitigate mode partition noise. The efficiency of the method is confirmed by simulation and measurement. The proposed technique has advantages of low cost and easy implementation because no external devices, such as the spatial light modulator (SLM), are needed. Chapter 7 concludes the thesis and highlights the contribution of each chapter. The possible future works are also presented.

Chapter 2

Background

This chapter presents the theoretical background of the VCSEL-MMF link. Section 2.1 is an overview of the VCSEL-MMF link. In this section, the applications of the link are introduced. As essential components of the link, VCSELs and MMFs have achieved significant progress recently, and Section 2.2 introduces the recent progress and development of VCSELs and MMFs, followed by presenting several techniques to improve the transmission performance. Section 2.3 showcases the multiplexing techniques, including spatial division multiplexing and wavelength division multiplexing. With the increase of the transmitted data rate, digital signal processing and advanced modulation formats have been utilized in the short-reach interconnects, as detailed in Section 2.4. Mode selective excitation, with advantages of low cost and low power consumption, improves the link bandwidth. The methods for mode selective excitation are indicated in Section 2.5.

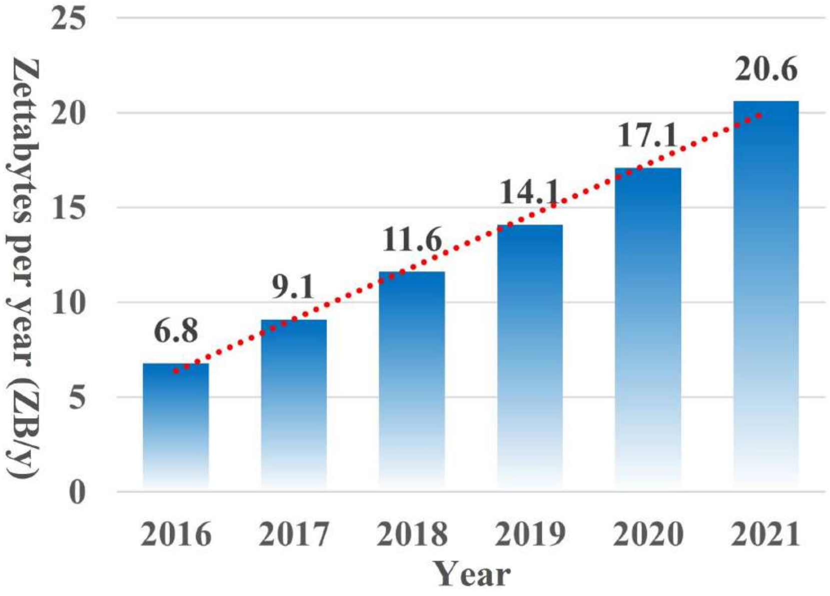

Fig. 2.1: Global data center traffic, 2016-2021. [22]

2.1 An overview of the VCSEL-MMF link

The data center traffic has dominated the overall Internet traffic since 2018. Driven by applications such as streaming video, social networking, and cloud computing, the datacenter traffic reaches 20.6 zettabytes per year (ZB/y) in 2021 from 6.8 ZB/y in 2016 [22]. The data center traffics from 2016 to 2021 are presented in Fig. 2.1, showing a linear growth trend. Accordingly, the datacenter interconnects are facing challenges of high speed, low fabrication cost, and low power consumption. Based on the Cisco white paper [22], the traffic within the data center accounts for 71% of the data center traffic, as illustrated in Fig. 2.2.

The technologies used in the data center are listed in Table 2.1. VCSEL-MMF

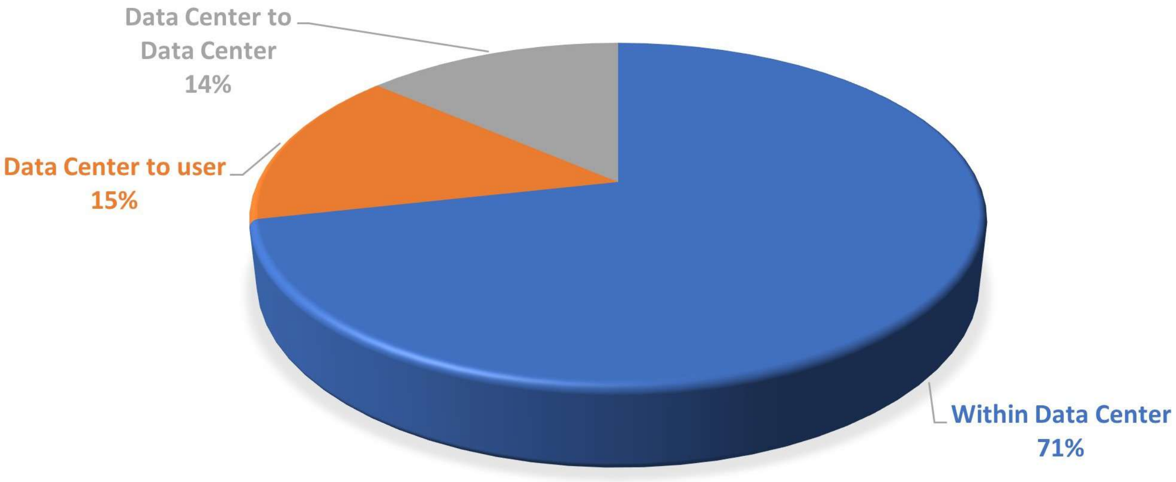

Fig. 2.2: Global data center traffic by destination in 2021. [22]

interconnects are utilized in over 85% of intra-datacenter links [3]. Over 90% of links have a length of less than 100 m [23]. Therefore, VCSEL-based MMF links are dominating short-reach intra-datacenter interconnects and will for several years still.

Table 2.1: Technologies used in current data centers [23].

Reach	Fiber Type	Loss Budget	Technology	Wavelength
0 - 100 m	Multi-mode	3 dB	VCSEL	850 nm
100 m - 300 m	Multi-mode	3 dB	VCSEL	850 nm
300 m - 1000 m	Single-mode	3 - 4 dB	DML, Si Photonics	1310/1550 nm
1000 m - 10 km	Single-mode	6.5 dB	EML, DML	1310/1550 nm

200 G and 400 G Ethernet standards are currently used, while speeds of 800 Gbps and 1.6 Tbps are expected possible between 2023 and 2025. Up to now, researchers have made

much progress to improve the transmission speed of the single lane. To realize an over 100 Gbps transmission, a PAM4 signal was modulated over the VCSEL because of its excellent spectral efficiency [24]. With the help of digital signal processing, a 100 Gbps data sequence was transmitted over a 100-m OM4 MMF and a next-generation wideband MMF. In 2021, an 850-nm VCSEL based 200-Gbps PAM-4 transmission over 100-m OM4 MMF was demonstrated [25]. This is the first demonstration of a 200 Gbps single-lane transmission using the VCSEL-MMF link. Furthermore, J. Lavrencik, *et al.* demonstrated the feasibility of scaling the link capacity to 1 Tbps [26]. The performance improvement of the link requires device optimization and the use of advanced techniques. Up to now, the VCSEL bandwidth has been extended to over 30 GHz. With the improved fabrication process, MMF has evolved into the fifth generation OM-5, supporting short wavelength division multiplexing (SWDM). With the OM-5 MMF, the fiber effective modal bandwidth reaches 4700 MHz·km at 850 nm and 2470 MHz·km at 953 nm. Additionally, multiplexing techniques, digital signal processing (DSP), advanced modulation formats, and mode selective excitation techniques are also adopted to improve the channel capacity and the transmission performance. The background knowledge of these techniques will be introduced in the following sections.

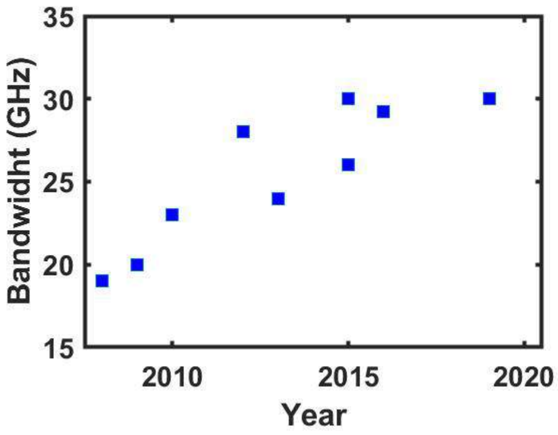

Fig. 2.3: A schematic describing the VCSEL bandwidth improvement over years 2008-2019.

2.2 Progress in VCSELs and MMFs

Since 2000, the VCSEL design and fabrication have made a significant breakthrough. The research on large-bandwidth VCSELs has attracted much concern from academia and industry. Fig. 2.3 shows the advances of VCSELs in recent years. The bandwidth increased to over 30 GHz in 2019, while the reported bandwidth was only 19 GHz in 2008.

According to ambient temperatures, the VCSEL has cryogenic, room-temperature (RT), and high-temperature applications, respectively. The recent advances for the VCSELs are listed in Table 2.2. The cryogenic VCSELs are usually used for focal plane arrays operating at 77 K and superconducting computers operating at 4 K. W. Fu, *et al.* developed a cryogenic VCSEL in [27], which bias current and bandwidth at the cryogenic temperature of 82 K are 0.3 mA and 50 GHz, respectively. Utilizing this 50 GHz cryogenic VCSEL, the authors successfully implemented a 51.56 Gbps PAM-4 signal transmission at

77 K. Based on their results, one finds that the cryogenic VCSEL could have a bandwidth far larger than that at RT, providing a possible insight into the operation temperature of the future data center system. The bandwidths of most VCSELs are limited to approximately 30 GHz at room temperature and high temperature. In 2020, researchers from UT Austin published their results at Conference on Lasers and Electro-Optics(CLEO) 2020 [28]. A multiple-transverse coupled-cavities VCSEL was proposed with an ultra-large 3 dB modulation bandwidth of 45 GHz. However, more information, such as the emission wavelength and static DC response, were not reported.

Table 2.2: VCSEL advancements since 2005. T: temperature (°C); λ: emission wavelength (nm); f: bandwidth (GHz).

Designer	**Year**	**T**	λ	f	**Ref.**	**Designer**	**Year**	**T**	λ	f	**Ref.**
NEC	2006	RT	1100	20	[29]	**NEC**	2007	RT	1100	24	[30]
NEC	2008	RT	1100	24	[31]	**TUB**	2008	120	980	11	[32]
Finisar	2008	RT	850	19	[33]	**UCSB**	2009	RT	980	> 20	[34]
CUT	2009	RT	850	20	[35]	**TUB**	2009	RT	850	20	[36]
CUT	2010	RT	850	23	[37]	**Finisar**	2012	95	850	10	[38]
CUT	2012	RT	850	28	[39]	**NCU**	2012	RT	850	22.4	[40]
NCU	2012	85	850	22.4	[40]	**SEDU**	2013	85	850	16	[41]
CUT	2013	85	850	21	[42]	**CUT**	2013	RT	850	24	[43]
TIT	2013	RT	980	29	[44]	**UIUC**	2013	RT	850	21.2	[45]
TUB	2014	85	980	18	[46]	**TUB**	2014	85	980	23	[47]

TUB	2014	RT	980	24.7	[47]	**NCU**	2015	85	850	20	[48]
IBM	2015	85	850	21	[49]	**NCU**	2015	RT	850	26	[48]
CUT	2015	RT	850	30	[4]	**UIUC**	2016	RT	850	29.2	[50]
UIUC	2016	85	850	24.5	[50]	**TUB**	2016	RT	980	26.6	[51]
TUB	2016	85	980	24.5	[51]	**NCU**	2016	RT	850	24∼29	[52]
CUT	2017	85	1060	16	[53]	**CUT**	2017	RT	1060	22	[53]
TUB	2017	RT	980	31	[54]	**TUB**	2017	85	980	25	[54]
TUB	2018	RT	980	35.5	[55]	**UIUC**	2019	115	850	21	[56]
UIUC	2019	RT	850	30	[56]	**VIS**	2020	RT	850	30	[57]
BCM	2020	75	850	28	[58]	**UTA**	2020	RT	–	45	[28]
UIUC	2021	−190	880	50	[27]						

Note:
TUB: Technische Universität Berlin; UCSB: University of California, Santa Barbara;
CUT: Chalmers University of Technology; NCU: National Central University;
SEDU: Sumitomo Electric Device Innovations USA; TIT: Tokyo Institute of Technology;
UIUC: University of Illinois at Urbana-Champaign; VIS: VI Systems GmbH;
BCM: Broadcom Inc.; UTA: The University of Texas at Austin.

The conventional VCSELs are generally based on the multi-quantum-well structure. To obtain a larger-bandwidth VCSEL, other structures, such as the coupled-cavity and the quantum-dot, are being investigated. For example, authors in [59] proposed a quantum-dot-based VCSEL and applied this VCSEL to realize a 40 Gbps NRZ transmission at a high temperature of 150 °C. Although no specific bandwidth data was indicated in the paper, the quantum-dot-based VCSEL did lead to a much clearer eye diagram than the conventional quantum-well-based VCSEL. This implies that the quantum-dot-based VCSEL is able to provide a broader bandwidth.

Table 2.3: Comparison between different kinds of multimode fibers.

Category	Core/Cladding Diameter (μm)	Overfilled Modal Bandwidth @ 850 nm (MHz·km)	Effective Modal Bandwidth @ 850 nm (MHz·km)	Effective Modal Bandwidth @ 953 nm (MHz·km)
OM1	62.5/125	200	Not specified	Not specified
OM2	50/125	500	Not specified	Not specified
OM3	50/125	1500	2000	Not specified
OM4	50/125	3500	4700	Not specified
OM5	50/125	3500	4700	2470

Benefiting from optimized manufacturing procedures, the bandwidth of the MMF also improves. The comparisons between different generations of the MMF are shown in Table 2.3. The graded-index structure has less modal dispersion compared to the step-index structure. Thus, the MMF for telecommunication purposes has a graded-index profile. Overfilled modal bandwidth and effective modal bandwidth characterize fiber modal dispersion. Overfilled modal bandwidth is measured using light sources exceeding the numerical aperture of the fiber such as light-emitting diodes, where fiber modes are equally excited. Effective model bandwidth is measured using the VCSEL sources and the differential mode delay technique as standardized in FOTP-220 [60].The first-generation OM1 MMF has a core diameter of 62.5 μm, which overfilled modal bandwidth at 850 nm is 200 MHz·km. The OM2 MMF has a smaller core diameter of 50 μm and a better overfilled modal bandwidth of 500 MHz·km.

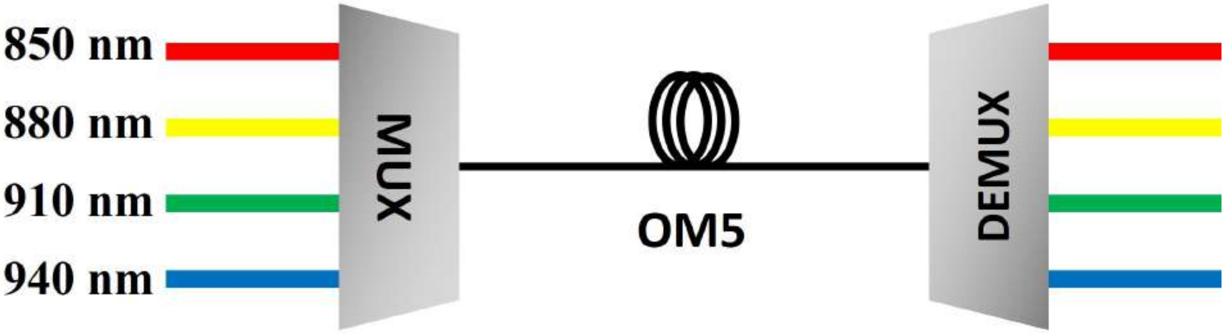

Fig. 2.4: The illustration of SWDM.

With a more precise refractive index profile, the laser-optimized OM3 and OM4 MMF evolve into a larger bandwidth compared to the OM2 MMF. Especially, the OM4 MMF is designed to minimize the modal dispersion, leading to an overfilled modal bandwidth of 3500 MHz·km and an effective modal bandwidth of 4700 MHz·km. To suit the need for the high-capacity data transmission, the SWDM technique is proposed, in which the spacing between adjacent wavelength channels is 30 nm. Unfortunately, the OM4 MMF has no clear specifications in wavelength ranges beyond 850 nm; thus, the wide-band MMF, also called the OM5 MMF, is fabricated to provide a stable bandwidth of over 2470 MHz·km from 850 nm to 953 nm. The SWDM technique over the OM5 MMF is illustrated in Fig. 2.4, where a single fiber can support simultaneous transmission of multiple wavelength channels. As such, the cost of the entire transmission infrastructure is significantly reduced in comparison with the case where a bulky fiber ribbon cable is used. Therefore, the SWDM technique has been applied in the 100 Gigabit Ethernet [61, 62].

2.3 Multiplexing Techniques

The channel multiplexing techniques enable transmission capacity enhancement. More specifically, the VCSEL-MMF short-reach interconnects mainly adopt spatial division multiplexing (SDM) and wavelength division multiplexing (WDM).

Spatial division multiplexing has three realization methods. The first method is to use a fiber array ribbon with multiple independent fiber lanes. This method is more easily implemented but takes up space for data centers. The second method is to transmit data signals over a multi-core fiber (MCF); in this case, each core of the MCF acts as one channel. For this method, the critical concern is to manage the core distribution inside the cladding to have the maximum core number and the minimum inter-core crosstalk. The third method is to use the few-mode (FF) or multimode (MM) fiber. With this method, the signals are modulated to the guided fiber modes or mode groups given various mode field distributions. Moreover, the few-mode-multi-core fiber also attracts much attention and further extends the transmission capacity by combining the second the third methods. These fibers for spatial division multiplexing are sketched in Fig. 2.5.

In light of the inter-core coupling strength, MCFs have two categories: the weakly-coupled MCF and the strongly-coupled MCF. The widely used weakly-coupled MCF is a 7-core fiber. To have weak coupling, a trench structure between adjacent cores was proposed to reduce the inter-core crosstalk of the MCF [63], with crosstalk value of -35 dB over 100 km at 1550 nm.

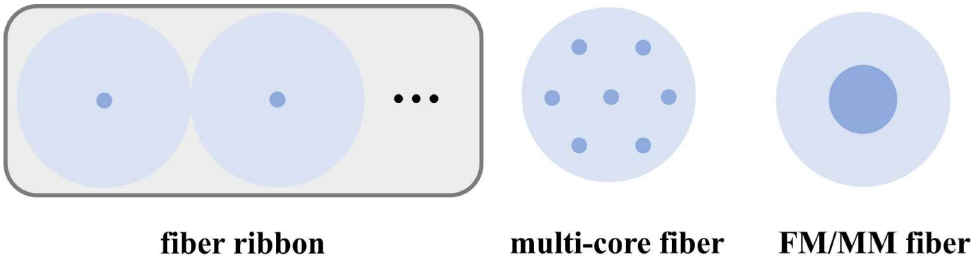

Fig. 2.5: Fibers used for spatial division multiplexing.

The strongly-coupled MCF has a more dense core distribution but higher inter-core crosstalk strength. Due to the smaller core-to-core distance of less than 30 μm, the coupling coefficient between cores is generally larger than 0.1, and the induced crosstalk needs to be overcome using DSP techniques.

Mode/mode group division multiplexing, adopted by the third method, uses diverse spatial intensity distribution patterns of the fiber linearly polarized modes, illustrated in Fig. 2.6. To excite the required mode channels in fiber, spatial optical devices, such as phase plates and spatial light modulators, shape the wavefront of the optical signal. This method has a simple implementation, facilitating laboratory research. However, the technique based on spatial optical devices remains challenging in deployed VCSEL-MMF links due to devices' large size, high insertion loss, and high cost. As alternatives, fiber-based devices, such as long-period fiber gratings, photonic lanterns, or mode-selective couplers, act as mode multiplexers/demultiplexers. Compared with the bulky spatial optical devices, fiber-based devices have the advantages of low insertion loss, compact size, and better compatibility with the MMF link.

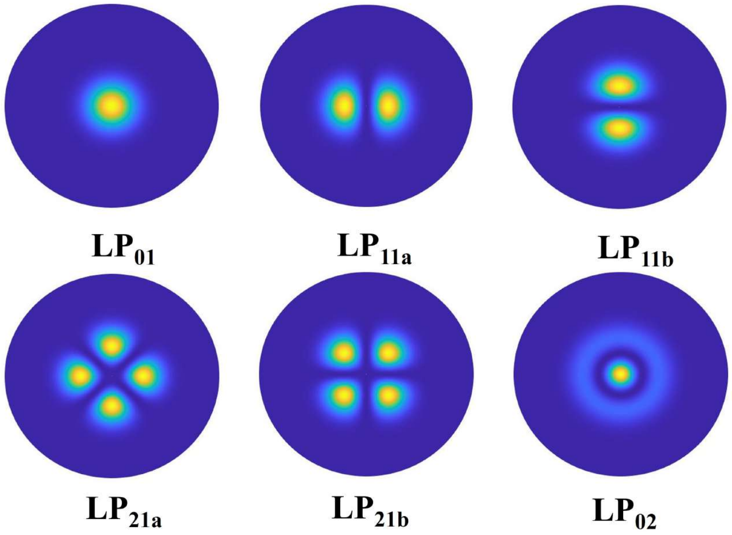

Fig. 2.6: Spatial power distribution of fiber linearly polarized modes.

It is worth noting that orbital angular momentum (OAM) multiplexing is a special kind of MDM. By multiplexing the beams with different topological charges, OAM MDM is an attractive and promising solution to increase the link capacity considering the orthogonality of OAM beams. The OAM multiplexing usually focuses on the use of the azimuthal indices, while the importance of radial indices is underestimated. Recently, a group from the University of Southern California investigated the multiplexing of Laguerre–Gaussian beams with different radial indices [64]. Their experiment demonstrated a 200 Gbps free-space transmission system with two Laguerre-Gaussian beams LG_{00} and LG_{01}. To some extent, the idea proposed for free-space optics should provide some inspirations for the fiber-based transmission.

The targets of MDM are the individual modes over fiber; thus, the mode coupling phenomenon is the major restriction of the signal performance. The modes within the same mode group share the same propagation constant, leading to severe mode coupling. As a result, a signal processing process is required to mitigate the distortion, and an ASIC chip designed for signal processing consumes additional power.

In addition to MDM, mode group division multiplexing (MGDM) uses mode groups rather than modes as independent channels. Due to divergent propagation constants, the crosstalk between adjacent mode groups is negligible, especially for the short-reach interconnect. The modes included in the first five mode groups are shown in Fig. 2.7. Owing to the low mode mixing, the MIMO processing module can even be removed from the receiver side. However, one drawback of MGDM is the limited number of channels compared to MDM. Two schemes are proposed to realize the MGDM. One is to use external devices such as multi-plane light converters (MPLCs) and mode-selective couplers (MSCs) to excite the mode groups [65]. Moreover, as the second scheme, launch conditions are tuned to excite multiple mode groups acting as a so-called “super mode group”. A lens between the optical source and the fiber is optional to assist the mode group selective excitation. The first method results in more channel quantities, but with a complicated setup. The second method can be implemented more easily. However, several mode groups are combined as a complete channel, i.e. a super mode group; thus, the available channels are less than those when using the MPLC and the MSC.

In addition to SDM, short wavelength division multiplexing (SWDM) is another valuable

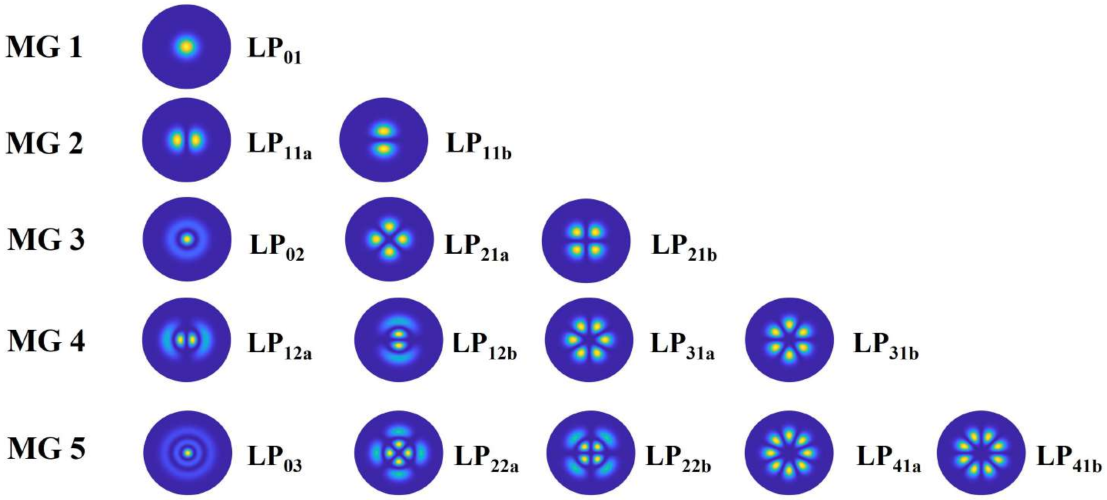

Fig. 2.7: Modes within the first five mode groups.

multiplexing technique for short-reach VCSEL-MMF interconnects. SWDM is categorized into two types: SWDM4 representing four wavelength channels and SWDM8 representing eight wavelength channels. The operating wavelengths of SWDM4 are 850 nm, 880 nm, 910 nm, and 940 nm, respectively. For SWDM8, the wavelength range covers from 850 nm to 1060 nm with a wavelength spacing of 30 nm. The optical source compatibility with the SWDM specification is a crucial issue. While the conventional VCSEL usually works at 850 nm, VCSELs working at other wavelengths are also fabricated, as shown in Table 2.2. As an application of SWDM, J. Lavrencik, *et al.* demonstrated an error-free transmission using 850 nm, 980 nm, and 1060 nm VCSELs and 100 m OM5 fiber in [66]. This shows the feasibility of the wavelength multiplexing over a range of 850 nm to 1060 nm. With the scheme of SWDM8, the channel number has a 2-fold increase compared to SWDM4, and the transmission capacity over one single fiber can eventually reach 1 Tbps with the help of

SWDM [26].

2.4 DSP and advanced modulation formats

With more stringent requirements for transmitted data rates, DSP techniques for the short-reach VCSEL-MMF links are developed, and more advanced modulation formats are also adopted.

Generally, an optical signal can be modulated based on four dimensions: amplitude, phase, frequency, and polarization. The most widely-used and straightforward modulation format is the non-return-to-zero (NRZ) code, where one symbol transmits one bit. Additionally, advanced modulation formats, such as 4-level/8-level pulse amplitude modulation (PAM4/PAM8), carriless amplitude and phase modulation (CAP), and discrete multitone modulation (DMT), have been used in the VCSEL-MMF links. These advanced modulation formats provide higher spectral efficiency and improve the transmitted bit rate. On the other hand, they also result in modulation nonlinearity and reduced signal noise ratios. The recent demonstrations about the use of advanced modulation formats in VCSEL-MMF links are detailed as follows.

The transmitted bit rate doubles the baud rate using the PAM-4 format, while the bit rate is equal to the baud rate for the NRZ modulation. PAM-8 carries 3 bits per symbol. Numerous experiments based on pulse amplitude modulation are carried out to improve the transmitted bit rate over a single fiber lane. For PAM-4, a 200 Gbps transmission was realized over 100m MMF based on an 850 nm VCSEL for the first time in [25]. This contribution provides a solution for the next-generation 800 GbE and 1.6 GbE Ethernet. As an example of using PAM8, researchers from ETH Zurich experimented with 108 Gbps PAM8 transmission over 25 m OM3 fiber [67]. With the help of pre-equalization at the transmitter side and feed-forward equalization at the receiver side, the received bit error rate of the PAM8 signal was below the 7% FEC threshold of 3.8×10^{-3}.

In addition to pulse amplitude modulation, the modulation formats of CAP and DMT are also exploited in the VCSEL-MMF link. The researchers from the University of Cambridge successfully achieved 112 Gbps and 124 Gbps CAP-16 data transmission over a single-lane OM4 MMF of 100 m [68]. Their experiments show that it is feasible to use CAP modulation over a VCSEL-MMF link to achieve a data rate of over 100 Gbps. In 2021, DMT modulation realized 224 Gbps transmission with SD-FEC and 180 Gbps transmission with HD-FEC over 1-m OM3 fiber [69]. Their transmission experiment was achieved at both 850 nm and 910 nm, and a gross data rate of over 400 Gbps should be possible using both the SWDM technique and the DMT modulation format.

In addition to advanced modulation formats, strong nonlinear equalizers such as Volterra equalizers and neural network equalizers have been used to improve the signal performance for the short-reach VCSEL-MMF link, while these equalizers are also widely used for the long-reach transmission. Recently proposed equalizers for short-reach VCSEL-MMF links are summarized in Table 2.4. An attractive concern is to increase the equalizer performance but reduce the equalizer computation complexity simultaneously. For example, Peking University did substantial research to optimize equalizers for the VCSEL-MMF link [70,71]. In [70], they proposed a Gaussian mixture model-hidden Markov model based nonlinear equalizer to help the PAM-4 signal transmission over the VCSEL-MMF interconnect link. The computational complexity of the proposed equalizer reduces by 73% compared to that of the neural network-based equalizer. Additionally, an advanced adaptive neural network-based equalizer was also investigated by the same group [71]. Their scheme required an adaptive online training, removing conventional labeled training sequences. As a result, a 56 Gbps PAM4 signal was transmitted over 100 OM4 fiber, and the BER was below 1×10^{-3} with the help of a neural network-based equalizer. Researchers from Shanghai JiaoTong University proposed a threshold-based pruned retraining Volterra equalizer to reduce the computation complexity by 70.7%, maintaining a good transmission performance [72]. They also developed a neural network-based equalizer, which assisted 112-Gbps PAM-4 and PAM-8 transmissions based on a 850-nm multimode VCSEL over 100 m OM3 MMF [73]. Furthermore in [74], a high-performance and low-complexity Volterra equalizer was successfully demonstrated, where a record of 93% complexity reduction was reported and the BER still reached a value below the KP4 FEC limit of 2×10^{-4} after 200-m OM4 MMF.

As seen from the above-mentioned literature, the research of equalizers concentrates on two directions: one is to have excellent linear and non-linear compensation abilities with affordable computation burden; the other is to reduce computation complexity but maintain

Table 2.4: Advanced equalizers for the short-reach VCSEL-MMF link.

Group	Year	Equalizer	Mod. Format	Bit Rate (Gbps)	Baud Rate (GBaud)	Reach	FEC	Ref.
PKU	2020	Gaussian Mixture Model-Hidden Markov Model Based Equalizer	PAM4	56	28	100-m OM4	HD-FEC	[70]
PKU	2020	Neural Network Equalizer	PAM4	56	28	100-m OM4	HD-FEC	[71]
SJTU	2019	Volterra Equalizer	PAM4	100	50	100-m OM3	HD-FEC	[72]
SJTU	2020	Neural Network Equalizer	PAM4 /PAM8	112	56/37	100-m OM3	HD-FEC	[73]
NSYSU	2018	Volterra Equalizer	PAM4	112	56	200-m OM4	KP4-FEC	[74]
CAM	2019	CAP Equalizer	CAP16	112	28	150-m OM4	HD-FEC	[75]
CAM	2019	Neural Network Equalizer	CAP16	112	28	100-m OM4	HD-FEC	[76]

good equalization performance. Combining multiplexing techniques, advanced modulation formats and novel equalizers, a VCSEL-MMF interconnect link supporting dozens of Tbps traffic is believed achievable.

2.5 Mode selective excitation

MMF as a type of multimode device allows multiple modes to propagate simultaneously. Owing to spatial mode distribution, the mode temporal delays are quite different. Mode selective excitation effectively manipulates the fiber mode generation and leads to a better

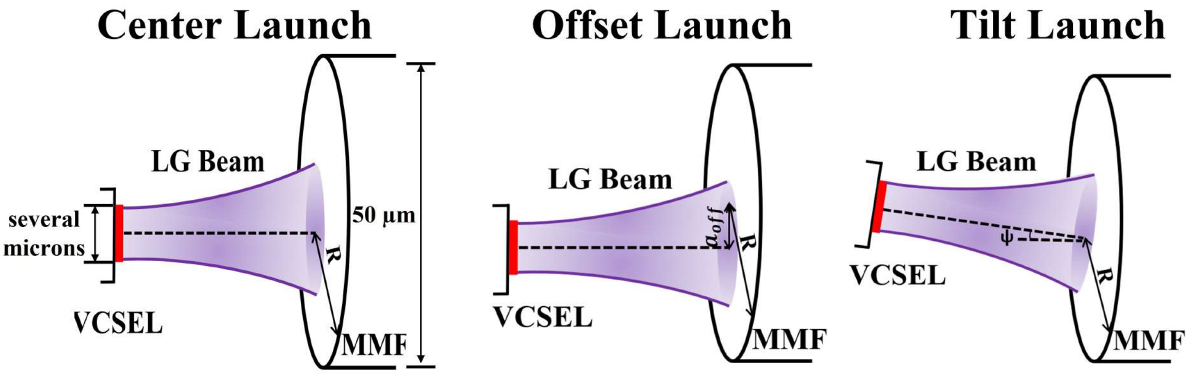

Fig. 2.8: Schematic for center launch, offset launch, and tilt launch. R is the radius of the fiber core; a_{off} is the radial offset; ψ is the tilt angle.

transmission performance. Two solutions here are proposed to optimize the MMF mode excitation. One is to tune the beam launch condition; the other is to shape the beam using optical devices such as a SLM or a phase plate.

The MMF has a core radius of 25 μm, while the beam radius is of the order of several microns. Benefiting from the radius difference between the VCSEL beam and the MMF, the beam at the fiber input facet has sufficient translation and tilt space. Based on categories of launch conditions, the central-launch, offset-launch, and tilt-launch techniques have been proposed in the past few years. These launch conditions are illustrated in Fig. 2.8. The mode-field matched central launch technique was presented by Prof. Y. C. Chung in 2007 [77], where only the fundamental mode was excited and transmitted over MMF. In 2020, they successfully transmitted 112 Gbps PAM-4 signal over 1-km OM2 MMF with only a 9-tap feed forward equalizer [78]. The offset launch scheme utilizes the radial offset between the laser and the MMF input surface to excite high-order modes selectively. For the offset

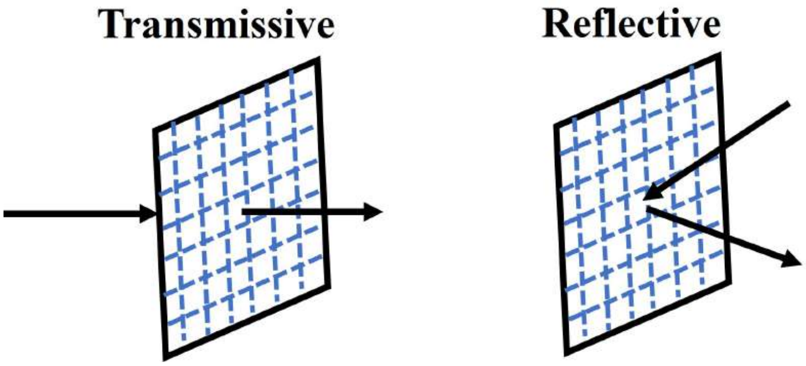

Fig. 2.9: The transmissive SLM and the refractive SLM.

launch, J. Carpenter used this technique to improve the signal integrity in [79, 80]. The tilt launch varies the incidence angle of the laser beam from the laser to the fiber input facet. With different tilt angles, excited modes or mode groups have various power coupling coefficients. Applying the tilt launch, N. Sheffi demonstrated a 5×5 multiple-input–multiple-output (MIMO) system based on the mode group theory [81]. The maximum crosstalk was lower than $-9\,\mathrm{dB}$, and the minimum coupling efficiency was larger than $-1.5\,\mathrm{dB}$. In addition to the central launch, the offset launch, and the tilt launch, other beam launch strategies, such as the line launch [82], the ring launch [83], the two-spot launch [84], were also implemented. Selective excitation by optimizing the launch condition does not require external devices; accordingly, this low-cost characteristic meets the cost and energy usage requirements for short-reach datacenter links.

Another idea for mode selective excitation is to shape the beam amplitude and phase using external optical devices. Typical devices for wavefront shaping are the spatial light modulator

(SLM) and the phase plate. The SLM consists of independent optical units forming a one-dimensional or two-dimensional array, and can be categorized into the transmissive SLM and the refractive SLM [85], as shown in Fig. 2.9. Using the SLM, the amplitude and/or the phase of the light are dynamically modulated so that the beam with the specific spatial distribution is selectively generated after the SLM. The phase plate is a low-cost optical device, which is usually made of glass. The beam phases are tuned due to various optical paths at different regions of the phase plate.

With the assistance of external optical devices, mode selective excitation can be easily implemented to improve the transmission performance [86], multiplex fiber channels [87], and produce beam patterns [82, 88]. In [86], MPN was mitigated using a SLM, where 25-Gbps OOK signal after 300-m MMF transmission was performed with about 1-dB power penalty improvement compared to the case without wavefront shaping. Also, due to the selective mode excitation assisted by the SLM, a 25-channel MDM-WDM system was realized to increase the communication capacity [87]. In addition, by applying SLMs, phase plates, or beam shaping masks, special beams such as the Hermite-Gaussian line beam [82] and the Hermite-Gaussian square beam [88] have been obtained to achieve selective mode excitation, increasing the link bandwidth.

To conclude this chapter, some background knowledge and recent advances of the VCSEL-MMF link are presented. After the summarized progress of VCSELs and MMFs in Section 2.2, several techniques to improve the transmission capacity are introduced in

Sections 2.3–2.5, including multiplexing techniques, digital signal processing, advanced modulation formats, and mode selective excitation techniques. Next, my contributions to VCSEL-MMK link transmission will be presented in Chapters 3–6.

Chapter 3

A Compact High-Efficient Equivalent Circuit Model of MQW VCSELs

In this chapter, a compact equivalent circuit model with noise effects is proposed for high-speed MQW VCSELs. The model comprehensively accounts for the carrier and photons dynamisms of a MQW structure, which includes separate confinement SCH layers, barrier layers, and quantum well layers. The proposed model is generalized to various VCSEL designs and accommodates a flexible number of quantum wells. Experimental validation of the model is performed at 25 Gbps with a self-wire-bonded 850 nm VCSEL. The work has been published as a journal paper in Applied Sciences in 2020 [14].

3.1 Introduction

Due to their low power consumption [89], high modulation speed [26], and low cost [90] vertical-cavity surface-emitting lasers (VCSELs) based links dominate modern datacenter systems. A lot of development works have been carried out in the fabrication of

VCSELs [52, 91, 92]. For these diverse design structures, the number of quantum wells differs. As the demand for greater capacity increases, the VCSEL has incorporated equalization circuitry, embedded in drivers through CMOS technology [93, 94]. To facilitate VCSEL design, fabrication and evaluation, an accurate VCSEL model, accommodating the variable quantum well (QW) number, needs to be built in an electronic-photonic co-simulation platform.

Previous models were proposed to simulate the performance of multi-quantum-well (MQW) VCSELs [10, 95, 96]. In these models, the number of rate equations are proportional to the number of QWs such that the model cannot be generalized to all VCSEL designs [97, 98], and are not suitable for the system-level simulation of VCSEL-based fiber links. The parameter extraction will also be a significant challenge in view of the extremely large number of parameters. In addition, these models do not account for noise effects, which are significant for assessing the transmission performance.

A versatile compact equivalent circuit model with noise effects is proposed for the MQW VCSEL. The proposed model accommodates a flexible number of quantum wells (QW's), which provides the freedom to simulate an arbitrary VCSEL in the system-oriented opto-electronic simulation platform. The model is developed in the commercial Cadence tool suite, a schematic-driven tool for CMOS electronic integrated circuit design. The chapter outline is as follows. Section 3.2 explains the VCSEL parasitic circuit model, which determines the small-signal response. In Section 3.3, the carrier and photon dynamisms are analyzed for the structure including separate confinement hetero-structure layers, barrier layers, and quantum well layers. In the QW layer, the carriers have two states: the confined state inside the quantum well and the unconfined state above the quantum well. In Section 3.4, based on the VCSEL structure analysis, a set of rate equations is obtained for the MQW VCSEL. After that, a versatile compact rate equation set is obtained, with a significant reduction in the number of equations. Laser intensity noise is expressed based on the Markovian assumption and added to the compact rate equations. In Section 3.5, the rate equations with noise terms are translated into the corresponding equivalent circuit equations. The equivalent circuit model for the MQW VCSEL is realized. In Section 3.6, the accuracy of the proposed VCSEL model is validated using a self-wire-bonded 850 nm VCSEL. In Section 3.7, a summary is provided.

3.2 VCSEL Structure and Dynamism Analysis

Although designs and materials used for the VCSELs vary, these VCSELs have one typical common structure, as shown in Figure 3.1. Two multi-layered Bragg reflectors are located at the top of the p-doped region and at the bottom of the n-doped region, with the high-index layer and low-index layer alternating. Constructive interference is caused by the reflections at the interface between the high-index and low-index layers for the reflective wave around the Bragg wavelength, and the multiple layers act as a mirror to improve optical gain [99]. The oxide layer, with a specific aperture size, transversely confines carriers to the active region. The p-doped and n-doped regions provide carrier injection for the active region between them.

The active region consists of separate confinement heterostructure (SCH) layers, barrier (B) layers, and quantum well (QW) layers, detailed in Figure 3.1b. The SCH1 layer is adjacent to the n-doped region, while the SCH2 layer is adjacent to the p-doped region. The barrier layers are sandwiched between two adjacent QW layers and have a larger energy bandgap than the QWs. Conventionally, the QWs of 850 nm VCSELs are fabricated using GaAs. However, InGaAs QWs increase the differential gain, which is advantageous to reach higher speeds [100]. In QW layers, carriers have two states: an unconfined state and a confined state. The confined state indicates the carriers are confined at the bottom of the wells and no longer free to move in three dimensions. The carriers in the unconfined state (also referred as the gateway (G) state) are free to move in three dimensions and occupy energy higher than the carriers in the confined state at the bottom of the well [101]. Therefore, the gateway state can be viewed as an intermediate state for carriers originating from either a SCH or barrier layer. The MQW-SCH-G-B structure is widely adopted for 850 nm VCSEL devices [97, 98]. In [97], the VCSEL performance investigation uses a 7-nm-thick GaAs MQWs separated by 8-nm-thick $Al_{0.3}Ga_{0.7}As$ barriers.

The dynamic behavior of the VCSEL is determined by the carrier and photon dynamism illustrated in Figure 3.1c. The carriers are injected into the active region due to the injection current. Then, carriers drift with applied electric field between the top and bottom contacts

(Figure 3.1a) and diffuse from carrier concentration gradient between the n-doped and p-doped regions. Carrier movements between the two energy bands are labelled capture when the carrier moves to a lower bandgap region, and escape when it jumps to a higher bandgap region. Tunneling is the quantum process, where a carrier penetrates through a barrier region, facilitating a carrier motion between adjacent QW regions. Photons are generated via stimulated emission involving an electron-hole recombination.

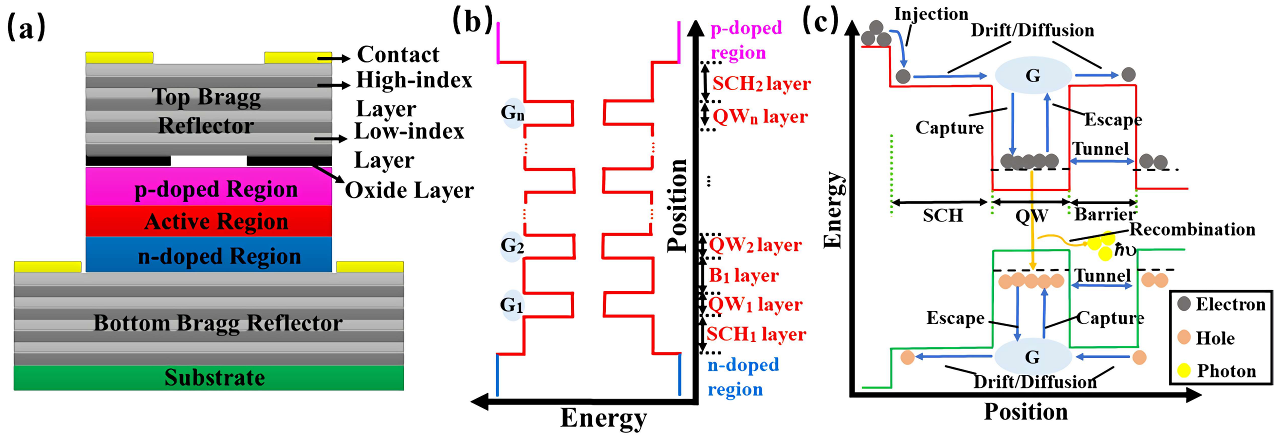

Fig. 3.1: (a) Cross-sectional schematic of a MQW VCSEL. (b) The active region of the VCSEL represented by a MQW-SCH-G-B band diagram. The subscript of SCH, QW, G, B represents the position of the corresponding layer. (c) The carrier and photon dynamics in the first QW are illustrated. The red and green solid lines represent the conduction and valence band edges, respectively. The black dash line represents the energy state in the quantum well.

3.3 Parasitic Circuit

A complete VCSEL model includes the extrinsic parasitic circuit description and the intrinsic rate-equation-based model. The parasitic circuit originates from the cavity structure explained in Section 3.2 and determines the small-signal response. The rate-equation-based model reflects the variation in the number of carriers and photons inside the active region.

The complete parasitic circuit model is shown in Figure 3.2a. The contact pads introduce resistance, capacitance and inductance to the parasitic circuit. C_p is the capacitance between the contacts, the resistance R_p represents the contact pad loss, and L_p is the inductance induced by the contacts. The resistance R_t and R_b model the top, and bottom Bragg reflectors, respectively. The oxide layer capacitance, C_{ox}, is in series with the junction capacitance, C_j. The resistance of the active region, R_a, is parallel with the series connection of C_{ox} and C_j. The time-varying current flowing through R_a serves as the input to the rate equation model. In Figure 3.2b, the parasitic circuit is simplified for further circuit analysis and modeling. The series connection of C_{ox} and C_j leads to C_a, and the combination of the top and bottom Bragg reflector resistances leads to R_m.

Based on Figure 3.2b, the input impedance of the parasitic circuit is expressed as,

$$Z_{in}\left(f\right)=\left(\left(\left(j\cdot 2\pi f\cdot C_p\right)^{-1}+R_p\right)^{-1}+\left(j\cdot 2\pi f\cdot L_p+R_m+\left(j\cdot 2\pi f\cdot C_a+{R_a}^{-1}\right)^{-1}\right)^{-1}\right)^{-1} \tag{3.1}$$

where f is the frequency of the modulation signal and j is the imaginary unit.

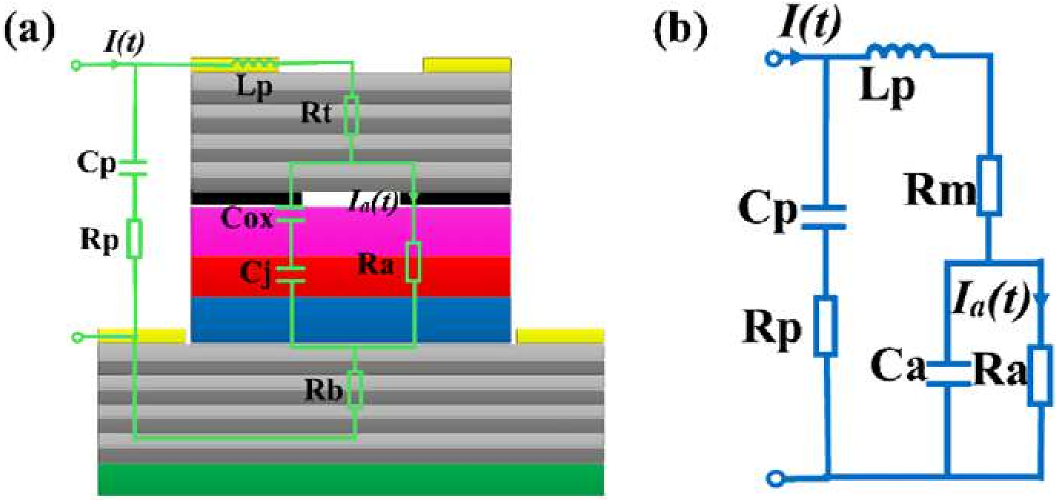

Fig. 3.2: (a) The complete parasitic circuit of the VCSEL; (b) the simplified parasitic circuit model.

The active region injection current with respect to time t, $Ia(t)$, is expressed in Equation (3.2),

$$I_a(t)=\frac{I_d\cdot e^{j\omega t}\cdot Z_{in}}{R_a+R_m-\omega^2 L_p C_a R_a+j\omega\left(C_a R_a R_m+L_p\right)} \tag{3.2}$$

where I_d is the amplitude of the time-varying high-speed driving current.

Due to Joule ohmic heating and free carrier absorption loss, the VCSEL self-heating effect leads to temperature elevation of the laser cavity [102]. The parasitic elements in the active region, R_m, R_a and C_a, are modelled as the function of the active region temperature, as shown in Equation (3.3),

$$f(T) = a_0 + a_1\left(T - T_0\right) + a_2(T - T_0)^2 + a_3(T - T_0)^3 + a_4(T - T_0)^4 \tag{3.3}$$

where a_0, a_1, a_2, a_3 and a_4 are the polynomial coefficients, T is the VCSEL cavity temperature in Kelvin, and T_0 is the relative temperature subtracted from T to reduce the requirement for coefficient extraction precision.

The active region temperature is expressed as follows due to the self-heating effect,

$$T = T_{amb} + \left(IV - P\right) R_{th} - \tau_{th}\frac{dT}{dt} \tag{3.4}$$

where T_{amb} is the ambient temperature, V is the device voltage, I is the driving current, P is the output light power, R_{th} is the thermal impedance of the VCSEL, and τ_{th} is the thermal time constant.

Considering the excellent thermal conductivity of the contact pads and relatively large gap between pads and the active region, it is accurate enough to regard R_p, C_p, and L_p as temperature-independent.

3.4 Compact Rate Equations

The SCH-QW-G-B bandgap structure in Section 3.2 is modeled using the set of rate equations expressing the carrier and photon dynamisms. In this section, the rate equation model describes the intrinsic behaviors of a MQW VCSEL with more complete carrier and photon dynamisms than previously reported [103, 104]. First, the rate equations are derived for the two SCH layers (SCH1 and SCH2) of the active regions. Carriers injected into SCH1 make their way to SCH2. The carrier movement between a SCH layer and an unconfined state in an adjacent QW layer determines the carrier quantity. In addition, electron-hole recombination in the SCH layer with high carrier density is included. The variations in carrier numbers with respect to time in the two SCH regions are expressed by the differential equations below,

$$\frac{dN_{SCH(1)}}{dt} = \frac{\eta_{inj} I_a\left(t\right)}{q} - R_{SCH(1)} - \frac{N_{SCH(1)}}{\tau_D} + \frac{N_{G(1)}}{\tau_D} \tag{3.5}$$

$$\frac{dN_{SCH(2)}}{dt} = -\frac{I_{leak}}{q} - R_{SCH(2)} - \frac{N_{SCH(2)}}{\tau_D} + \frac{N_{G(n_w)}}{\tau_D} \tag{3.6}$$

where $N_{SCH(i)}$ and $R_{SCH(i)}$ represent the carrier number and the combination rate in SCH1 (i = 1) and SCH2 (i = 2). η_{inj} is the current injection efficiency (dimensionless) and q is the electron charge. The injection current $I_a\left(t\right)$ is a time-varying high-speed signal, and I_{leak} is the leakage current. $N_{G(j)}$ is the unconfined carrier number in the gateway state of the QW layer, where the subscript j denotes the gateway state in the jth QW layer counting from the bottom of the active region (in Figure 3.1b). The number of gateway states in the active region is the same as the number of QWs (denoted as n_w), therefore $1 \leq j \leq n_w$. τ_D is the effective carrier transport time between a SCH or barrier layer and its adjacent gateway state.

Next, the gateway rate equations for the carriers are derived. In the first gateway state (at the bottom of the active region in Figure 3.1b) and the last gateway state (at the top), the following effects are considered: the carrier exchange with the adjacent SCH or barrier layer, the electron-hole recombination, and the carrier exchange with the confined states within the QW layer. Equation (3.7) represents the rate equation for the unconfined carriers in the bottom QW layer ($j = 1$),

$$\frac{dN_{G(1)}}{dt} = \frac{N_{SCH(1)}}{\tau_D} - \frac{2N_{G(1)}}{\tau_D} + \frac{N_{B(1)}}{\tau_D} + \frac{N_{W(1)}}{\tau_{esc}} - \frac{N_{G(1)}}{\tau_{cap}} - R_{G(1)} \tag{3.7}$$

where $N_{B(1)}$ is the carrier number in the bottom barrier layer, $N_{W(1)}$ and $R_{G(1)}$ are the confined carrier number and the recombination rate of the unconfined carriers in the bottom QW layer, respectively. τ_{esc} and τ_{cap} are the QW carrier escape, and capture lifetimes, respectively. The rate equation for unconfined carriers in the top QW layer is expressed in

(3.8),

$$\frac{dN_{G(n_w)}}{dt} = \frac{N_{SCH(2)} - 2N_{G(n_w)} + N_{B(n_w-1)}}{\tau_D} + \frac{N_{W(n_w)}}{\tau_{esc}} - \frac{N_{G(n_w)}}{\tau_{cap}} - R_{G(n_w)} \tag{3.8}$$

where the subscript n_w represents the top layer. For gateway states in the other QW layers (i.e., $2 \leq j \leq n_w - 1$) which are adjacent to two barrier layers, the rate equation is expressed by Equation (3.9).

$$\frac{dN_{G(j)}}{dt} = \frac{N_{B(j-1)} - 2N_{G(j)} + N_{B(j)}}{\tau_D} + \frac{N_{W(j)}}{\tau_{esc}} - \frac{N_{G(j)}}{\tau_{cap}} - R_{G(j)}, \quad 2 \leq j \leq n_w - 1 \tag{3.9}$$

Similarly, in the barrier layer, I consider the carrier exchange between the barrier layer and the two adjacent gateway states as well as the electron-hole recombination using Equation (3.10),

$$\frac{dN_{B(k)}}{dt} = \frac{N_{G(k)}}{\tau_D} - \frac{2N_{B(k)}}{\tau_D} + \frac{N_{G(k+1)}}{\tau_D} - R_{B(k)}, \quad 1 \leq k \leq n_w - 1 \tag{3.10}$$

where $R_{B(k)}$ is the recombination rate in the kth barrier layer.

For confined carriers by the quantum wells, the dynamisms, such as carrier capture/escape, quantum tunneling, spontaneous and stimulated emissions, and recombination, are accounted. The following equation represents the rate equation for confined carriers in the first QW layer,

$$\frac{dN_{W(1)}}{dt} = \frac{N_{G(1)}}{\tau_{cap}} - \frac{N_{W(1)}}{\tau_{esc}} - R_{W(1)} - \frac{N_{W(1)} - N_{W(2)}}{\tau_{tun}} - v_g \Gamma_{_{W(1)}} G_{W(1)} S_{W(1)} \tag{3.11}$$

where $S_{W(1)}$ represents the photon number in this QW layer. τ_{tun} is the tunneling time, and v_g is the group velocity of the lasing medium. $R_{W(1)}$, $\Gamma_{_{W(1)}}$ and $G_{W(1)}$ represent the recombination rate, the optical confinement factor, and the gain coefficient for the confined carriers. The rate equation for the confined carriers in the last QW layer is expressed as the following,

$$\frac{dN_{W(n_w)}}{dt} = \frac{N_{G(n_w)}}{\tau_{cap}} - \frac{N_{W(n_w)}}{\tau_{esc}} - R_{W(n_w)} - \frac{N_{W(n_w)} - N_{W(n_w-1)}}{\tau_{tun}} - v_g \Gamma_{W(n_w)} G_{W(n_w)} S_{W(n_w)} \tag{3.12}$$

where the subscript is replaced to represent the top layer (n_w). The rate equation for confined carriers in all other QW layers is expressed as follows, where the subscript is generalized to j to represent the jth QW layer.

$$\begin{gathered} \tfrac{dN_{W(j)}}{dt} = \tfrac{N_{G(j)}}{\tau_{cap}} - \tfrac{N_{W(j)}}{\tau_{esc}} + \tfrac{N_{W(j-1)} + N_{W(j+1)} - 2N_{W(j)}}{\tau_{tun}} - R_{W(j)} - v_g \Gamma_{W(j)} G_{W(j)} S_{W(j)}, \\ 2 \leq j \leq n_w - 1 \end{gathered} \tag{3.13}$$

Finally, Equation 3.14 accounts for the photon number generated in the jth QW,

$$\frac{dS_{W(j)}}{dt} = -\frac{S_{W(j)}}{\tau_p} + R_{\omega\beta_{(j)}} + v_g \Gamma_{W(j)} G_{W(j)} S_{W(j)} \tag{3.14}$$

where τ_p is the photon lifetime. $R_{\omega\beta_{(j)}}$ represents the rate of electron-hole recombination of the lasing mode.

The rate equations describing these carrier and photon dynamisms are detailed above. The number of differential rate equations reaches $4 \cdot n_w + 1$ for a VCSEL where n_w corresponds to the number of QWs, leading to a challenging computation complexity. In addition, parameter extraction from the experimental results is required to simulate and evaluate the performance of the manufactured VCSEL. The number of parameters included in the aforementioned equations is relatively large, which challenges parameter extraction. Furthermore, the proposed rate equations are strongly dependent on the number of QWs, such that the model cannot be generalized to all VCSEL designs as those in [97, 98], where the numbers of QWs in these designs are quite different. It is, therefore, necessary to manipulate the rate Equations (3.5)–(3.14) to make them independent from the number of QWs. The detailed analysis of carrier and photon behaviors builds a set of rate equations for their comprehensive dynamisms, and the inclusion of the gateway states bridges SCH layers and QW layers. Consequently, the issues mentioned above are overcome by a series of transformations of rate equations. Combining Equations (3.5) to (3.10), Equation (3.15) below describes the variation in the total number of unconfined carriers, N_S,

$$\frac{dN_S}{dt} = \frac{\eta_{inj} I_a - I_{leak}}{q} - R_{N_S} + \frac{N}{\tau_e} - \frac{N_S}{\tau_c} \tag{3.15}$$

where N is the total number of confined carriers inside each a QW. The total number of unconfined carriers, N_S, and of confined carriers, N, in all layers are expressed as the following:

$$N_S = \sum\nolimits_{i=1}^{2} N_{SCH(i)} + \sum\nolimits_{j=1}^{n_w} N_{G(j)} + \sum\nolimits_{k=1}^{n_w-1} N_{B(k)}, \qquad N = \sum\nolimits_{j=1}^{n_w} N_{W(j)}. \tag{3.16}$$

The total recombination rate for the unconfined carriers in all layers gives the equivalent recombination rate as, R_{N_S}, which shows the total number of recombined unconfined carriers per unit time:

$$R_{N_S} = \sum\nolimits_{i=1}^{2} R_{SCH(i)} + \sum\nolimits_{j=1}^{n_w} R_{G(j)} + \sum\nolimits_{k=1}^{n_w-1} R_{B(k)}. \tag{3.17}$$

The equivalent escape lifetime τ_e is equal to τ_{esc}, while the equivalent capture lifetime τ_c is expressed as the following:

$$\tau_c = \tau_{cap} \cdot \frac{N_S}{\sum_{j=1}^{n_w} N_{G(j)}}. \tag{3.18}$$

The confined carrier dynamisms are expressed below by combining Equations (3.11) to (3.13),

$$\frac{dN}{dt} = \frac{N_S}{\tau_c} - \frac{N}{\tau_e} - R_N - v_g G_N S \tag{3.19}$$

where the photon number S is the total number of photons in QW layers, R_N is the total recombination rate for the confined carriers, and G_N is the gain coefficient weighted by optical confinement factors. These can be expressed as the following:

$$S=\sum\nolimits_{j=1}^{n_w} S_{W(j)}, \quad R_N=\sum\nolimits_{j=1}^{n_w} R_{W(j)}, \quad G_N = \frac{1}{S} \cdot \sum\nolimits_{j=1}^{n_w} \Gamma_{W(j)} G_{W(j)} S_{W(j)}. \tag{3.20}$$

For the photon dynamisms, Equation (3.21) is derived from the summation of (3.14) over the QW position j:

$$\frac{dS}{dt} = -\frac{S}{\tau_p} + R_S + v_g G_N S, \quad where\ R_S=\sum\nolimits_{j=1}^{n_w} R_{\omega\beta(j)}. \tag{3.21}$$

With respect to Equations (3.15), (3.19) and (3.21), the equation set for the carrier and photon dynamisms consists of three differential equations, an important reduction in computation for the modeling of a laser source with MQWs. Each differential equation is assumed to consume the same computation time, because the terms in equations are similar. The calculation efficiency, defined as the reciprocal of the computation time for the whole equation set, improves by 3.3-fold for a laser source with three QWs and by 6-fold for five QWs.

The recombination rate terms R_{N_S}, R_N and R_S consist of three main types of recombination: Shockley-Read-Hall (SRH) non-radiative recombination, radiative recombination and Auger non-radiative recombination. A third-order polynomial based on the ABC model [105] describes recombination terms, where A_{N_S}, A_N and A_S are SRH recombination coefficients for unconfined carriers, confined carriers and photons, B_{N_S}, B_N

and B_S are corresponding radiative recombination coefficients, and C_{N_S}, C_N and C_S are corresponding Auger recombination coefficients. The expressions for R_{N_S}, R_N and R_S are expressed in Equation (3.22). Specifically, the radiative recombination dominates the photon generation, and non-radiative recombination effects are negligible. Therefore, values of A_S and C_S are set to 0.

$$\begin{aligned} R_{N_S} &= A_{N_S} N_S + B_{N_S} {N_S}^2 + C_{N_S} {N_S}^3, \\ R_N &= A_N N + B_N N^2 + C_N N^3, \\ R_S &= A_S N + B_S N^2 + C_S N^3 \end{aligned} \tag{3.22}$$

The strong thermal dependence of VCSEL I–P characteristics is mainly attributed to the temperature-dependent carrier leakage out of the active region [106]. The carrier leakage is represented by the leakage current I_{leak} in Equation (3.15), which is expressed by a fourth-order polynomial of temperature in Equation (3.23). It is worth mentioning that the fourth-order polynomial provides sufficient parameter fitting accuracy and acceptable computation complexity,

$$I_{leak} = b_0 + b_1 (T - T_0) + b_2 (T - T_0)^2 + b_3 (T - T_0)^3 + b_4 (T - T_0)^4 \tag{3.23}$$

where b_0, b_1, b_2, b_3, and b_4 are the polynomial coefficients. In the same way as Equation (3.3), T_0 is subtracted from T to reduce the requirement for coefficient fitting precision.

The weighted gain coefficient G_N is expressed as follows [106, 107]:

$$G_N = \frac{G_0\left(N - N_0\right)}{1 + \varepsilon S} \tag{3.24}$$

where G_0 is the gain coefficient, ε is gain suppression factor, and N_0 is the transparency carrier number.

Laser noise is important in the VCSEL model. As such, the noise terms F_{N_S}, F_N, F_S are added to the right-hand side of Equations (3.15), (3.19) and (3.21), accounting for fluctuation in N_S, N and S. The noise-inclusive rate-equations are expressed below as Equations (3.25) to (3.27):

$$\frac{dN_S}{dt} = \frac{\eta_{inj} I_a - I_{leak}}{q} - R_{N_S} + \frac{N}{\tau_e} - \frac{N_S}{\tau_c} + F_{N_S} \tag{3.25}$$

$$\frac{dN}{dt} = \frac{N_S}{\tau_c} - \frac{N}{\tau_e} - R_N - v_g G_N S + F_N \tag{3.26}$$

$$\frac{dS}{dt} = -\frac{S}{\tau_p} + R_S + v_g G_N S + F_S \tag{3.27}$$

Based on the Markovian assumption that the noise sources have relatively small correlation time compared to the carrier and photon lifetimes [108, 109], F_{N_S}, F_N and F_S satisfy the following correlation functions,

$$\left\langle F_K(t) F_J(t') \right\rangle = 2D_{K,J}\delta(t - t') \qquad K, J = N_S, N, S \tag{3.28}$$

where the angle bracket represents time-average operator, and $\delta(t)$ is the Kronecker delta function. $D_{K,J}$ is the diffusion coefficient, described by Equation (3.29),

$$\begin{gathered} D_{N_S,N_S} = \tfrac{N_S}{\tau_n}; \quad D_{N,N} = R_{sp}S + \tfrac{N}{\tau_n}; \quad D_{S,S} = R_{sp}S; \quad D_{S,N} = D_{N,S} = -R_{sp}S; \\ D_{N_S,N} = D_{N,N_S} = D_{N_S,S} = D_{S,N_S} = 0 \end{gathered} \tag{3.29}$$

where R_{sp} is the spontaneous emission rate, and τ_n is the carrier recombination lifetime. With Equation (3.28) and (3.29), F_{N_S}, F_N and F_S are mathematically expressed in Equation (30),

$$F_{N_S} = \sqrt{2D_{N_S,N_S}}x_1; \quad F_N = -\sqrt{2D_{S,S}}x_2 + \sqrt{2\left(D_{N,N} - D_{S,S}\right)}x_3; \quad F_S = \sqrt{2D_{S,S}}x_2 \tag{3.30}$$

where x_1, x_2 and x_3 are independent Gaussian random variables with zero mean and unitary standard deviation.

3.5 VCSEL Equivalent Circuit Model

To realize the hybrid electronic-photonic modeling, the noise-inclusive rate Equations (3.25)–(3.27) are translated into a set of equations describing circuits. The equivalent circuit model is derived based on these circuit-described equations. To eliminate non-physical solutions of the carrier and photon dynamisms, Equation (3.31) is used to ensure that N_S and N are positive values,

$$N_S = N_{SEQ} V_{act} e^{\frac{V}{2V_T}}, \qquad N = N_{EQ} V_{QW} e^{\frac{V_w}{2V_T}} \tag{3.31}$$

where N_{SEQ} and N_{EQ} are the densities of unconfined and confined carriers in thermal equilibrium at zero bias, and V_{act} and V_{QW} are the volumes of the active region and the single QW. V_T, V, and V_w are the thermal voltage, and the voltages across the SCH and QW layers, respectively. The relationship between the total number of photons S and the optical output power P_o is expressed as Equation (3.32),

$$\frac{S}{P_o} = \frac{\lambda \tau_p}{2\pi \eta_c \hbar c} \tag{3.32}$$

where λ is the free space wavelength, τ_p is the photon lifetime, η_c is the output power coupling coefficient, $\hbar$ is reduced Planck constant, and c is the light speed in free space. By substituting (3.31) into (3.25), Equation (3.33) is obtained to represent the equivalent circuit for the unconfined carriers in terms of current variables,

$$I_a = I_C + I_D - I_{Cw} - I_{Dw} + I_1 + I_{RS} + I_L - I_{FNS} \tag{3.33}$$

where

$$I_C=\frac{qN_{SEQ}V_{act}}{\eta_{inj}\tau_c},\quad I_D=\frac{qN_{SEQ}V_{act}}{\eta_{inj}\tau_c}(e^{\frac{V}{2V_T}}-1),\quad I_{Cw}=\frac{qN_{EQ}V_{QW}}{\eta_{inj}\tau_e},\quad I_{Dw}=\frac{qN_{EQ}V_{QW}}{\eta_{inj}\tau_e}(e^{\frac{V_w}{2V_T}}-1),$$

$$I_1=\frac{qN_{SEQ}V_{act}}{2V_T\eta_{inj}}e^{\frac{V}{2V_T}}\frac{dV}{dt},\quad I_{R_S}=\frac{q}{\eta_{inj}}R_{N_S},\quad I_L=\frac{I_{leak}}{\eta_{inj}},\quad I_{FNS}=\frac{q}{\eta_{inj}}F_{N_S}.$$

In addition, Equation (3.34) is derived by substituting (3.31) and (3.32) into (3.26), which represents the equivalent circuit for the confined carriers in QWs,

$$I_C+I_D=I_{Cw}+I_{Dw}+I_2+I_{R1}+I_{S1}-I_{FN} \tag{3.34}$$

where

$$I_2=\frac{qN_{EQ}V_{QW}}{2V_T\eta_{inj}}e^{\frac{V_w}{2V_T}}\frac{dV_w}{dt},\quad I_{R1}=\frac{q}{\eta_{inj}}R_N,\quad I_{S1}=\frac{q\lambda\tau_p v_g G_N P_o}{2\pi\eta_{inj}\eta_c\hbar c},\quad I_{FN}=\frac{q}{\eta_{inj}}F_N.$$

Substituting (3.32) into (3.27), Equation (3.35) is obtained, describing the equivalent circuit for the photon dynamism,

$$C_p\frac{dV_o}{dt}+\frac{V_o}{R_p}=I_{R2}+I_{S2}+I_{FS} \tag{3.35}$$

where:

$$R_p = 1\ \Omega, \quad C_p = \frac{2\tau_p}{R_p}, \quad V_o = \sqrt{P_o R_p}, \quad I_{R2} = \frac{2\pi\eta_c\hbar c}{\lambda V_o} R_S, \quad I_{S2} = v_g G_N \tau_p \frac{V_o}{R_p}, \quad I_{FS} = \frac{2\pi\eta_c\hbar c}{\lambda V_o} F_S.$$

The equivalent circuit schematic is shown in Figure 3.3, based on Equations (3.33)–(3.35). The equivalent circuit model is realized in the Cadence Virtuoso environment based on the Verilog-A language. As seen from the mathematical derivations above, I_C, I_{C_ω} and I_L are considered as constant current sources, while I_D and I_{D_ω} are regarded as currents passing through a diode with the diode ideality factors equal to 2. Other current components, I_{RS}, I_{R1}, I_{R2}, I_{S1}, I_{S2}, I_1, I_2, I_{FNS}, I_{FS} and I_{FN}, are generated by time-varying current-controlled current sources. The circuit in the bottom right corner of Figure 3.3 converts V_O to the practical optical power output, P_O. R_L is an arbitrary resistor for completeness of the closed circuit, and its value does not influence the functionality of the circuit model.

3.6 Results and Discussion

The model validation and parameter extraction are divided into two parts: One is for the parasitic circuit and the other is for the circuits of carrier and photon dynamisms. For parameter extraction of the parasitic circuit, the S11 data are utilized. For the circuits of carrier and photon dynamisms, the measurement results of output optical powers at different bias currents are utilized.

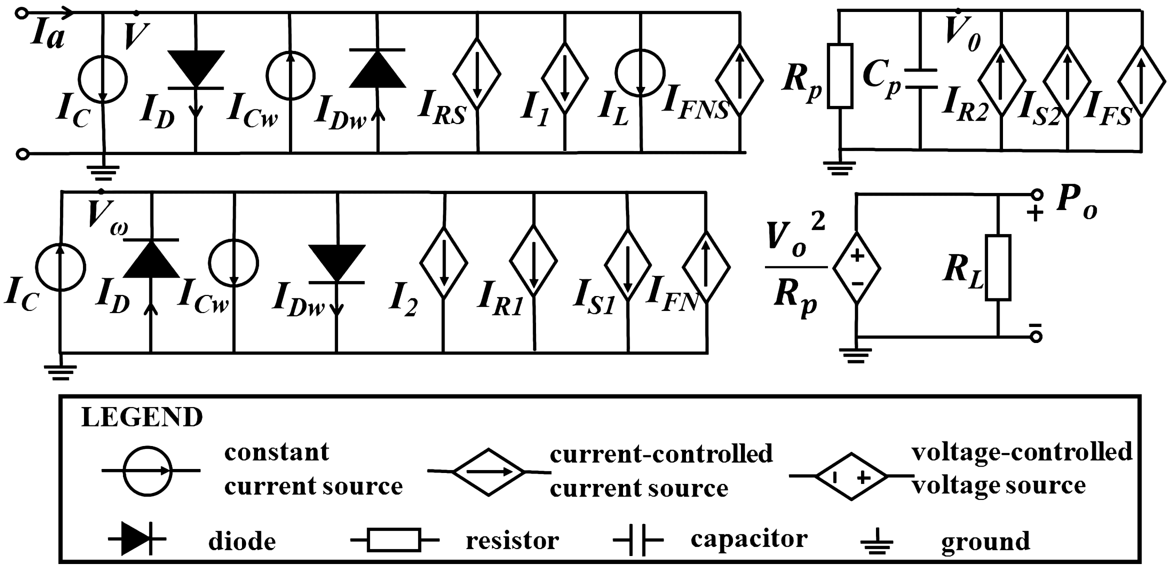

Fig. 3.3: The compact circuit model for carrier and photon dynamisms of the MQW VCSEL.

The experimental setup for S_{11} measurement is shown in Figure 3.4. A bias-tee is employed to combine the bias current and the small signal from a high-precision time-domain reflectometer (TDR). After the bias-tee, an 850 nm VCSEL chip is driven. S_{11} data are measured by the TDR module. The self-wire-bonded VCSEL chip under test is manufactured by II-VI Incorporated.

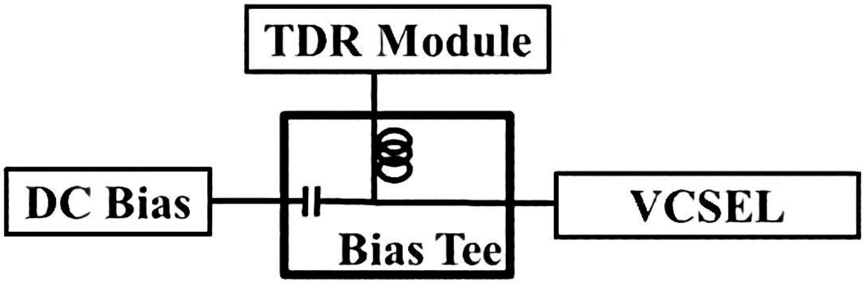

Fig. 3.4: The experimental setup for S11 measurement.

The measurement for I-V-P data (I for injection current; V for VCSEL voltage; P for optical power) is performed automatically using the computer program, and the experimental schematic diagram for I-V-P measurement is shown in Figure 3.5. The DC power supply is controlled by a personal computer (PC) to change the output voltage. A resistor of $462\,\Omega$ is used to protect the VCSEL, which voltage is recorded by a multi-meter. Therefore, the current passing through the resistor and the VCSEL can be obtained using Ohm's law. The fiber couples the light of the VCSEL and is connected to an optical power meter. The optical power meter data is recorded by a PC. Based on the I-V-P data, the VCSEL temperatures under different bias currents are obtained using Equation (3.4) with $R_{th} = 2 \times 10^3$ K/W. It needs to be pointed out that the differential term in the right-hand side of Equation (3.4) is equal to zero for the steady state.

The expression for the magnitude of S11 is shown below based on Equation (3.1),

$$H\left(f\right) = 20 \cdot \log_{10} \left| \frac{Z_{in}\left(f\right) - Z_0}{Z_{in}\left(f\right) + Z_0} \right| \tag{3.36}$$

where $Z_0 = 50\,\Omega$ is the measurement system impedance. The values of parasitic electrical elements are extracted using the least squares algorithm. The mean-square error between the calculated magnitude of S_{11} by Equation (3.36) and the measured data is minimized to determine the optimal value of each element. The extracted values of C_p, L_p and R_p are given in Table 3.1, and the polynomial coefficients of R_m, R_a and C_a are given in Table

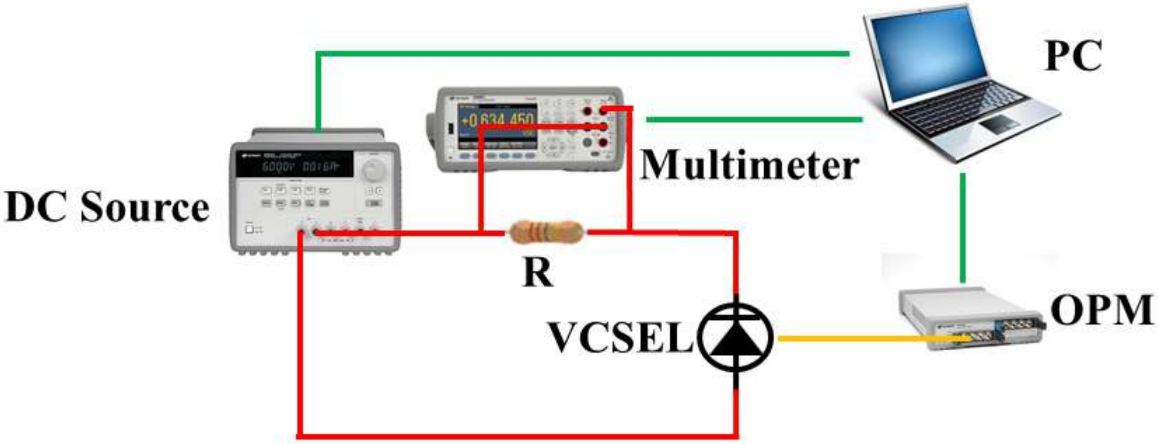

Fig. 3.5: The experimental schematic diagram for I-V-P measurement. The green lines represent the communications between a PC and measuring instruments; the red lines represent the electrical link; the yellow line represents the optical link. The DC source, multi-meter and OPM are controlled by PCs, respectively. DC: direct current; R: resistor; PC: personal computer; OPM: optical power meter.

3.2. The measured data and the simulation curves of S_{11} are depicted in Figure 3.6(a). The calculated S_{11} can fit the measured data very well.

Table 3.1: Extracted values of C_p, L_p and R_p.

Parameter	Unit	Value
C_p	pF	0
L_p	nH	0.86
R_p	Ω	4

Curve fitting of large-signal DC responses is utilized to extract the parameters for the rate equations which describe the VCSEL electro-optical dynamisms. With the obtained VCSEL temperatures, the coefficients b_0–b_4 are extracted by minimizing the sum of the squares of

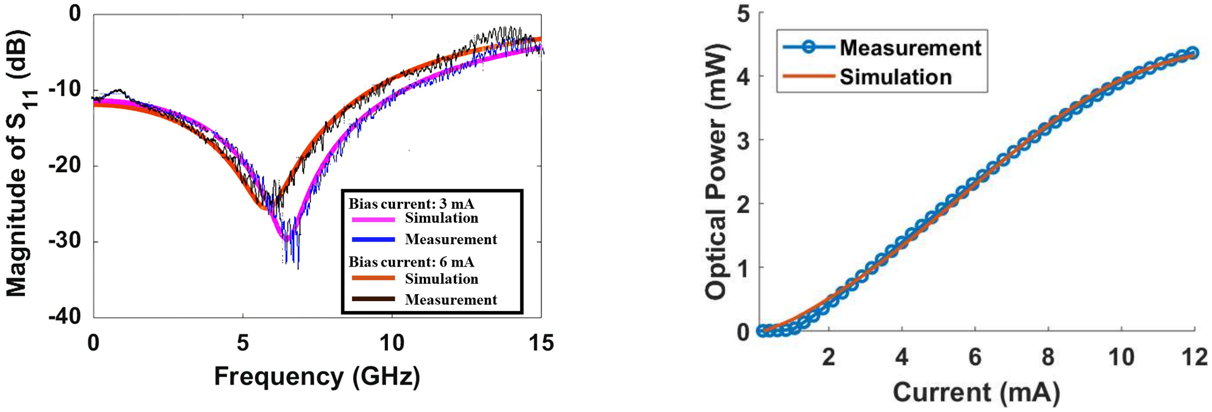

(a) (b)

Fig. 3.6: (a) The magnitude of the simulated and measured S11 under the bias current of 3 mA and 6 mA; (b) measured and simulated I-P characteristics.

Table 3.2: Polynomial coefficients of R_m, R_a and C_a.

Parameter	Unit	a0	a1	a2	a3	a4
R_m	Ω	280.70	-88.16	10.19	-0.47	0.01
R_a	Ω	-213.34	84.59	-9.06	0.40	-0.01
C_a	pF	4.05	-1.24	0.14	-0.01	1.02×10^{-4}

the residuals between the simulation and measurement results of the leakage current. T_0 in Equation (3.23) is chosen as 300 K. Under steady states, rate equations are simplified into the non-differential nonlinear equations. The temperature-independent parameters of nonlinear equations are extracted by fitting the I-P curve. Table 3.3 presents parameters of the rate equations, which are extracted by curve fitting. The simulated I-P curve and the experimental result are depicted in Figure 3.6(b), and they match with each other very well. Based on the extracted parameters in Tables 3.1–3.3, the equivalent circuit model is realized in Cadence Tool Suits (Virtuoso Environment 5.10.41). The 25 Gbps PRBS-7 transient responses under 6 mA bias current for both simulation and measurement are shown in Figure 3.7. The peak-to-peak jitter in the experiment is 11.3 ps, while the simulation result is 11.4 ps. The measured vertical and horizontal eye-opening ratios are 0.55 and 0.71, while the simulated ratios are 0.58 and 0.70, respectively. The measurement and simulation show satisfactory match, proving that the proposed model have strong ability to simulate the VCSEL performance.

Table 3.3: Parameters for the rate equations model.

Parameter	Unit	Value	Parameter	Unit	Value
η_{inj}	–	0.86	b_3	mA/K^3	2.4×10^{-4}
τ_e	ps	400	b_4	mA/K^4	-1.9×10^{-6}
τ_c	ps	1	A_{N_S}	s^{-1}	1.1×10^8
τ_p	ps	2.8	B_{N_S}	s^{-1}	5.3
V_{QW}	m^3	6×10^{-18}	C_{N_S}	s^{-1}	1.9×10^{-8}
V_{act}	m^3	2.3×10^{-16}	A_N	s^{-1}	1.3×10^8
N_{SEQ}	m^{-3}	4×10^{19}	B_N	s^{-1}	1.8×10^1
N_{EQ}	m^{-3}	6×10^{14}	C_N	s^{-1}	9.1×10^{-6}
τ_n	ns	5	A_S	s^{-1}	0
R_{sp}	s^{-1}	1.4×10^{12}	B_S	s^{-1}	1.8×10^{-3}
b_0	mA	5.1×10^{-2}	C_S	s^{-1}	0
b_1	mA/K	1.2×10^{-1}	v_g	m/s	8.6×10^7
b_2	mA/K^2	-8.7×10^{-2}	G_N	m^{-1}	4.2×10^3

3.7 Conclusions

A compact high-efficient equivalent circuit model is proposed for the multi-quantum-well VCSEL. The number of nonlinear equations significantly decreases, resulting in improvement of the computation efficiency by 3.3-fold for three QWs-VCSEL and by six-fold for five QWs-

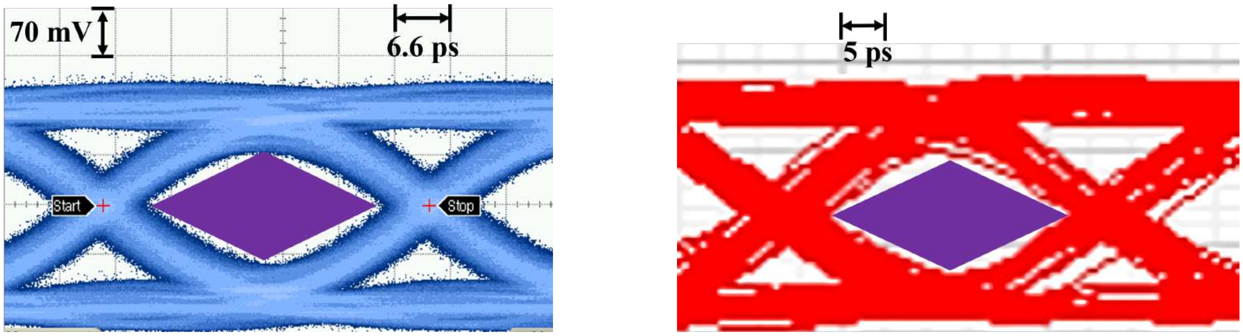

(a) **(b)**

Fig. 3.7: (a) The measured eye diagram of VCSEL at 25 Gbps; (b) the simulated eye diagram based on the proposed model.

VCSEL. In addition, parameter extraction becomes much easier compared to conventional MQW models, due to the reduction in the number of parameters. The model is system-oriented and can be used as a part of the VCSEL-based link modelling.

Chapter 4

Electronic-photonic Modeling of High-speed VCSEL-MMF Links

Spectral-dependent electronic-photonic modeling of VCSEL-MMF links is presented for next-generation high-speed interconnects. The beam coupling processes, between the VCSEL and the MMF and between the MMF and the PD, are discussed, with spectral-dependent three-dimensional launch conditions analyzed. The model accounts for fiber effects on the transmission performance, specifically modal attenuation, dispersion, mode mixing, and mode partition noise. An advanced split-step small-segment (4-S) method simulates the signal evolution over the MMF with high accuracy and high efficiency. Experimental validation at 25 Gbps confirms the high accuracy of the VCSEL-MMF link model. The model reveals that larger radial offsets can further excite lower-order mode groups reducing the power distributed to higher-order groups when a tilted beam couples to the input fiber facet. With an optimized misalignment launch, the modal bandwidth is greatly improved by 3.8-fold compared to the conventional center launch. The model helps determine the optimum launch condition to improve link performance metrics such as transmission reach. The work presented in this chapter has been published as a journal paper in Optics Express [15].

4.1 Introduction

Due to low power consumption [89], high modulation speed [26], and low cost [90], vertical-cavity surface-emitting laser (VCSEL)-multimode fiber (MMF) interconnects represent over 85% of short-reach datacenter links [110]. Further, more than 90% of MMFs are shorter than 100 m [23]. As the demand for greater capacity intensifies, high-speed devices such as VCSELs and photodetectors (PDs) are developed [111, 112]. Data rates of VCSEL-MMF transmission systems reach 100 Gbps per lane with equalization [72] and potentially reach 1 Tbps in aggregated capacity through multiplexing techniques [26]. At high-speed transmission, the mode launch condition has significant impact on the performance due to the enhanced fiber sensitivity to mode power distribution. The optimization of the beam launch condition, such as offset launch techniques [79, 84, 113–115] and tilt launch techniques [116], was studied for fiber bandwidth enhancement. As VCSEL-MMF links consist of electrical and optical components, as well as optoelectronic devices, a hybrid electronic-photonic link model plays a significant role in the design and evaluation of high-speed next-generation interconnects.

Device-level modeling previously reported [117, 118] do not account for the overall link-level system modeling in the device optimization. At the system level, a 10 GbE system model illustrates modal and chromatic dispersion interference (MCDI) [13]. However, the spectral dependence and other fiber effects are neglected affecting the simulation accuracy of the higher speed link. In addition, existing mode launch models only exploit specific mode-excitation conditions [81, 119]. In [120, 121], spatial segments of a PD are utilized to detect mode-division-multiplexed signals, where a fairly simple fiber-PD coupling model is given. Nonetheless, they do not further discuss the effects of launch conditions and free-space diffraction phenomenon between the fiber and the PD. Therefore, more accurate models of the VCSEL-MMF and MMF-PD coupling are required to simulate high-speed VCSEL-MMF links for next-generation interconnects. Additionally, signal processing CMOS circuits, such as equalizers, are generally used to extend link capabilities and mitigate the contradiction between increased data rates and limited device bandwidth [75, 122]. In such context, hybrid electronic-photonic modeling of a VCSEL-MMF link allows modular extension within an electronic design automation environment.

A comprehensive hybrid-electronic-photonic modeling platform is proposed, sensitive to the coupling conditions for high-speed VCSEL-MMF links. The chapter outline is as follows. In Section 4.2, the spectral-dependent beam coupling from the VCSEL to the free-space is analyzed. Section 4.3 explains the mode coupling over the fiber input facet. The radial offset and 3-dimensional (3-D) angular tilt are simultaneously included and coupling coefficient matrices are calculated for different coupling conditions. Section 4.4 introduces the coupling-coefficient-dependent fiber model sensitive to launch conditions.

An advanced split-step small-segment (4-S) method calculates the signal evolution over fiber. In Section 4.5, along with the coupling analysis from the MMF to the PD, a wavelength-sensitive PD model, matching the multi-wavelength characteristic of the VCSEL, realizes the opto-electric conversion. The proposed link model is developed in the commercial Cadence tool suite, a schematic-driven tool for CMOS electronic integrated circuit design. In Section 4.6, the high accuracy of the electronic-photonic modeling platform is validated by 25 Gbps non-return-to-zero (NRZ) transmission experiments over different coupling conditions and transmission distances. Section 4.7 presents impact of launching conditions on mode power distribution With spectral-dependent 3-D coupling conditions investigated, it is found that compared to high-order mode groups, further optical power can be distributed to low-order mode groups using a larger radial offset with a tilted beam. Section 4.8 is the conclusion.

4.2 VCSEL-to-Free-Space Coupling

As a part of the VCSEL-MMF link model, the advanced equivalent circuit model of the multiple-quantum-well (MQW) VCSEL in the previous chapter is used, which includes the extrinsic parasitic and equivalent circuits. The temperature-dependence and noise effects are accounted in the model as well as carrier and photon dynamisms. With the extracted parameters, the VCSEL model shows a satisfactory ability to reproduce the measurement results in small-signal and large-signal responses. The VCSEL outputs multiple transverse modes, with typical numbers from 3 to 10 [123]. When each VCSEL transverse mode is coupled into the MMF, the launch condition significantly impacts the link performance. Therefore, it is important to define the corresponding power of each VCSEL transverse mode and model the launch-condition-dependent VCSEL-MMF coupling. The VCSEL is modelled as a cylindrical weakly-guided step-index waveguide supporting linearly polarized (LP) modes [124]. Each mode exhibits its own specific resonant wavelength meeting the cavity resonance phase condition. The wavelength of the gth VCSEL LP mode, λ_g, is obtained from Eq. (4.1) using the effective index model [125]:

$$\lambda_g{=}\lambda_c - \lambda_c \frac{{\mu_g}^2 \left(n_a - n_c\right)}{n_c \left({\mu_g}^2 + {\omega_g}^2\right)} \tag{4.1}$$

where λ_c is the central wavelength, n_a and n_c are the refractive indices of the core and the cladding, μ_g and ω_g represent the core and cladding propagation parameter of the gth VCSEL mode. In the simulation, the value of n_a is obtained from the publications [86, 126]. Based on the step-index waveguide eigenvalue equation [127], μ_c, μ_g and ω_g are derived by fitting the measured VCSEL optical spectrum. It is worth mentioning that the VCSEL wavelength compositions slightly vary between devices due to fabrication process variations. For applications of mass production of VCSEL-MMF modules, statistical mean and worst-case parameters of VCSELs should be included in the model. As a proof-of-principle demonstration of the model, a typical multimode VCSEL spectrum is measured with a bias current of 6 mA using a 25 Gbps VCSEL (manufactured by II-VI Incorporated). The measured overall spectral power with an optical spectrum analyzer (Anritsu MS9710C) is shown in Fig. 4.1(a), fitting a Gaussian distribution. Based on the obtained Gaussian distribution and the wavelengths of VCSEL modes calculated in (4.1), Fig. 4.1(b) illustrates the output power of each VCSEL mode normalized to the peak value of the Gaussian distribution curve. The corresponding power of the gth mode (from right to left) is denoted as P_g. As seen from Fig. 4.1(b), the third and fourth VCSEL transverse modes (i.e., LP_{21} and LP_{02}) have close wavelengths such that both modes are superposed due to the linewidth of the transverse mode, resulting in a merged peak.

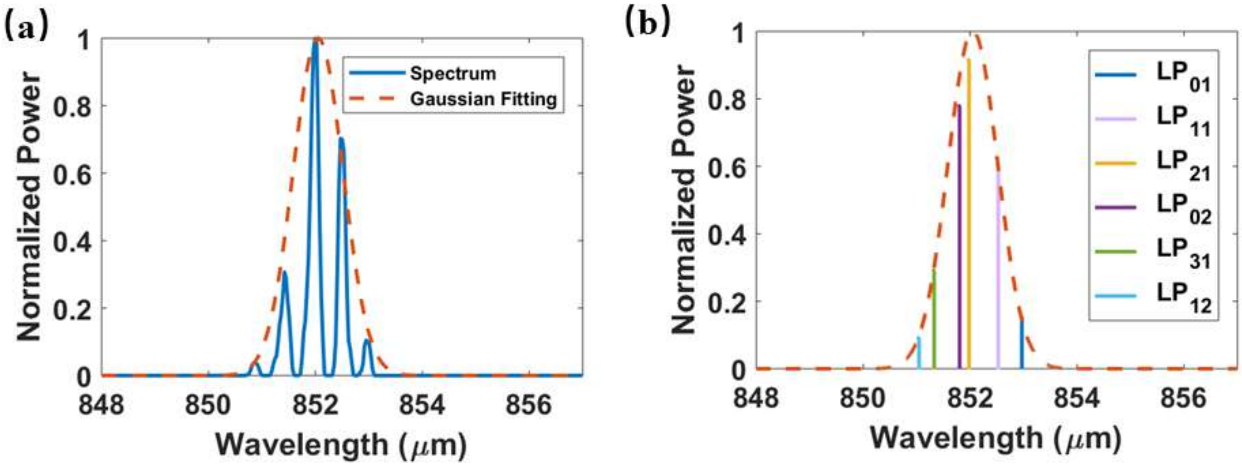

Fig. 4.1: (a) The measured VCSEL optical output spectrum. The solid blue line is the VCSEL spectrum for a typical bias current of 6 mA; the red dash line is a Gaussian fitting curve. (b) The normalized output power for each VCSEL mode to the peak value of the Gaussian distribution curve.

The cylindrical coordinate system ($\widetilde{r}$,$\widetilde{\varphi}$,$\widetilde{z}$) is used for modeling the VCSEL mode at its output, as shown in Fig. 4.2. The radial coordinate axis $\tilde{r}$ and the azimuthal coordinate axis $\tilde{\varphi}$ are at the VCSEL surface with the pole $\tilde{o}$ at the VCSEL aperture center. The coordinate axis $\tilde{z}$ is perpendicular to the VCSEL surface. The normalized transverse field of the gth VCSEL mode, $\widetilde{LP}_g$, is derived using Eq. (4.2) at $\tilde{z} = 0$ (i.e., at the VCSEL surface).

$$\widetilde{LP}_g(\tilde{r}, \tilde{\varphi}) = N_g \cdot \left\{ \frac{J_l(\mu_g \cdot \tilde{r} / a_v)}{J_l(\mu_g)} \cdot [1 - H(\tilde{r} - a_v)] + \frac{K_l(\omega_g \cdot \tilde{r} / a_v)}{K_l(\omega_g)} \cdot H(\tilde{r} - a_v) \right\} \cdot e^{-il\tilde{\varphi}} \quad (4.2)$$

where N_g is a normalization constant, a_v is the VCSEL oxide aperture radius, l is the azimuthal index of the gth LP mode, i is the imaginary unit. $H(\cdot)$ is the Heaviside Step Function, $J_l(\cdot)$ denotes the lth-order Bessel function of the first kind, and $K_l(\cdot)$ represents the lth-order modified Bessel function of the second kind.

As the VCSEL beam propagates in free space after emission, the diffraction will change its amplitude and phase. As a result of the symmetric circular structure of the VCSEL, modes are expanded over the Laguerre-Gaussian (LG) mode basis, accounting for the diffraction phenomenon. Eq. (4.3) expresses the normalized spectral-dependent mode profile of the hth LG mode, $\widetilde{\mathrm{LG}}_h$, in the cylindrical coordinate $(\tilde{r}, \tilde{\varphi}, \tilde{z})$, with f_1 and f_2 representing the amplitude and phase functions of the LG mode beam.

$$\widetilde{LG}_h(\tilde{r}, \tilde{\varphi}, \tilde{z}, \lambda) = f_1\left(\tilde{r}, \tilde{z}, \lambda\right) \cdot e^{-i \cdot f_2(\tilde{\varphi}, \tilde{z}, \lambda)} \quad (4.3)$$

The functions f_1 and f_2 are defined in Eq. (4.4) and Eq. (4.5),

$$f_1\left(\tilde{r},\tilde{z},\lambda\right)=\sqrt{\frac{2n!}{\pi(n+|\,m|)!}}\cdot\frac{1}{\omega\left(\tilde{z},\lambda\right)}\cdot\left(\frac{\sqrt{2}\tilde{r}}{\omega\left(\tilde{z},\lambda\right)}\right)^{|m|}\cdot L_n^{|m|}\left(\frac{2\tilde{r}^2}{\omega(\tilde{z},\lambda)^2}\right) \tag{4.4}$$

$$f_2\left(\tilde{\varphi},\tilde{z},\lambda\right)=\frac{\pi\tilde{r}^2}{\lambda q\left(\tilde{z},\lambda\right)}-\phi\left(\tilde{z},\lambda\right)+\frac{2\pi\tilde{z}}{\lambda}+m\tilde{\varphi} \tag{4.5}$$

where n and m are the radial and azimuthal indices of the LG mode, λ stands for the beam wavelength, $\mathrm{L}_n^m(\cdot)$ is the generalized Laguerre polynomial, $\omega(\tilde{\mathrm{z}},\lambda)$ denotes the spot size, $\phi(\tilde{\mathrm{z}},\lambda)$ expresses the Gouy phase shift, and $q(\tilde{\mathrm{z}},\lambda)$ is a complex beam parameter. The expressions for $q(\tilde{\mathrm{z}},\lambda)$, $\omega(\tilde{\mathrm{z}},\lambda)$, and $\phi(\tilde{\mathrm{z}},\lambda)$ are defined by Eqs. (4.6) to (4.8):

$$q\left(\tilde{z},\lambda\right)=\frac{\pi{\omega_0}^2\mathrm{A}\left(\tilde{z}\right)-i\lambda\mathrm{B}\left(\tilde{z}\right)}{\pi{\omega_0}^2\mathrm{C}\left(\tilde{z}\right)-i\lambda\mathrm{D}\left(\tilde{z}\right)} \tag{4.6}$$

$$\omega^2\left(\tilde{z},\lambda\right)=-\frac{\lambda}{\pi\mathrm{Im}\left(1/q\left(\tilde{z},\lambda\right)\right)} \tag{4.7}$$

$$\phi\left(\tilde{z},\lambda\right)=\left(2n+|m|+1\right)\arctan\left(\frac{\mathrm{B}\left(\tilde{z}\right)\cdot\lambda}{\mathrm{A}\left(\tilde{z}\right)\cdot\pi{\omega_0}^2}\right) \tag{4.8}$$

where ω_0 is the beam waist. $A(\tilde{z})$, $B(\tilde{z})$, $C(\tilde{z})$ and $D(\tilde{z})$ are the elements of a 2×2 ABCD matrix, describing the optical system between the VCSEL and the MMF (see in Fig. 4.2) [128, 129]. The optical system represented by the transfer matrix will depend on the type of optical module and may include a collimating lens or a 45° reflective metal, or both.

With Eqs. (4.2) and (4.3), the coupling coefficient c_{gh} between the gth VCSEL mode,

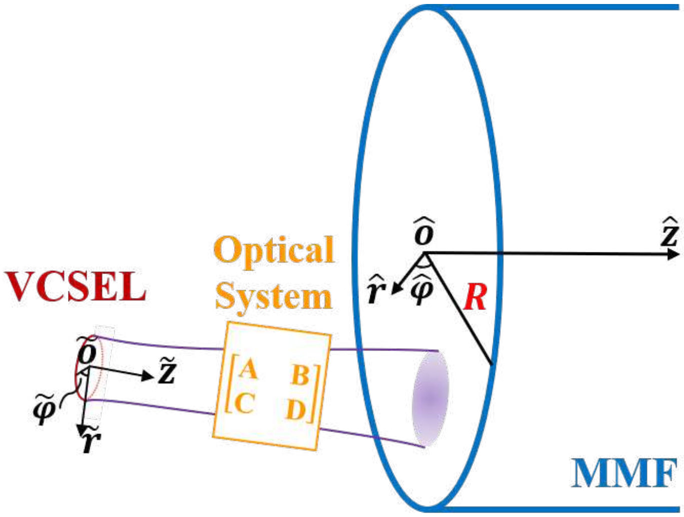

Fig. 4.2: Launching system between the VCSEL and the MMF using cylindrical coordinates$(\tilde{r}, \tilde{\varphi}, \tilde{z})$ referenced to the VCSEL and $(\hat{r}, \hat{\varphi}, \hat{z})$ referenced to the fiber. R is the fiber core radius. The optical system between the VCSEL and the MMF is defined by a 2×2 matrix.

$\widetilde{\mathrm{LP}}_g$, and the hth LG mode, $\widetilde{\mathrm{LG}}_h$, is obtained by the overlap integral as follows:

$$c_{gh}(\lambda_g) = K_f \iint_{A_V} \widetilde{LP}_g\left(\tilde{r}, \tilde{\varphi}\right) \cdot \left[\widetilde{LG}_h\left(\tilde{r}, \tilde{\varphi}, 0, \lambda_g\right)\right]^* \tilde{r} d\tilde{r} d\tilde{\varphi} \tag{4.9}$$

where K_f is the Fresnel coefficient for the fiber–air interface, A_V is the VCSEL aperture area, and the asterisk denotes the complex conjugate. K_f is approximately 0.98 because of the small refractive index difference between the air and the glass [126].

4.3 Free-Space-to-MMF Coupling

MMF is considered as a weakly-guided graded-index (GI) waveguide with the refractive index (RI) profile parameter α. Due to the cylindrical structure of the fiber, it is common to use the cylindrical coordinate system. As such, $(\hat{r}, \hat{\varphi}, \hat{z})$ describes the MMF LP mode field distribution. The radial coordinate axis $\hat{r}$ and the azimuthal coordinate axis $\hat{\varphi}$ are at the MMF input facet with the pole $\hat{o}$ at the center, and the $\hat{z}$-axis is along the fiber axis, as shown in Figs. 4.2 and 4.3. The analytical expression in Eq. (4.10) elucidates the uth MMF LP mode within the profile parameter range $(1.8 < \alpha < 2.2)$ of manufactured optical fibers [119] at $\hat{z} = 0$ (i.e., at the fiber input facet).

$$\widehat{MLP}_u(\hat{r}, \hat{\varphi}, \lambda) = \frac{1}{R} \cdot \sqrt{\frac{V^{|l'|+1}\Gamma(p')}{\pi\,\Gamma(p' + |l'|)}} \cdot \left(\frac{\hat{r}}{R}\right)^{|l'|} \cdot L_{p'-1}^{|l'|}\left(\frac{\hat{r}^2}{R^2} \cdot \mathrm{V}(\lambda)\right) \cdot e^{-\frac{\hat{r}^2}{2R^2} \cdot \mathrm{V}(\lambda) - il'\hat{\varphi}} \tag{4.10}$$

where l' and p' are the azimuthal and radial indices of the MMF LP mode, R is the fiber core radius, $\mathrm{V}(\lambda) = 2\pi R\sqrt{n_1(\lambda)^2 - n_2(\lambda)^2}/\lambda$ is the wavelength-dependent normalized frequency, and $\Gamma(m)$ is the gamma function equal to the factorial of $m - 1$. The modeling of the wavelength dependence of the core peak RI, n_1, and the cladding RI, n_2, uses the third order Sellmeier equation [130]. It is worth noticing that Eqs. (4.3) and (4.10) are both dependent on the optical wavelength λ, which implies that the field distribution of LG modes and MMF LP modes are different for diverse wavelengths.

Fig. 4.3 illustrates an arbitrary launch of LG beams with a radial offset and a 3-D angular tilt. The reference point P is at the center of the VCSEL, zd is the distance between the VCSEL center and the light spot center at the fiber input facet. Three right-handed Cartesian coordinate systems are used for modeling. The plane $\hat{x}-\hat{y}$ of the coordinate system $\hat{o}-\hat{x}-\hat{y}-\hat{z}$ is located at the input facet of fiber, where the origin $\hat{o}$ is the center of the fiber input facet, $\hat{x}$-axis coincides with the direction of the beam radial offset and $\hat{z}$-axis coincides with the fiber axis. $\overline{o}-\overline{x}-\overline{y}-\overline{z}$ has a lateral translation of a_{off} from $\hat{o}-\hat{x}-\hat{y}-\hat{z}$ along the $\hat{x}$-axis. Different from the first two coordinate systems, $\check{o}-\check{x}-\check{y}-\check{z}$ is at the beam wave front plane, where $\check{y}$-axis corresponds to the intersection line between the MMF input facet and the beam contour across $\check{o}$, and $\check{z}$-axis is along the beam optical axis. At the input facet of MMF, the free-space LG beam excites MMF LP modes, with the radial offset a_{off}, the incidence tilt ψ between the $\hat{z}$-axis and the $\check{z}$-axis, and an azimuthal tilt θ between the $\hat{y}$-axis and the $\check{y}$-axis. The combination of a_{off}, ψ and θ ensures an arbitrary launch condition in three-dimensional space, overcoming the restriction of launch conditions in reported literatures [81,119]. ψ has a value ranging from 0 to 90°. θ is between $-180°$ and 180°, relying on the coordinates of the point P, $(\overline{\mathrm{P}_X}, \overline{\mathrm{P}_Y}, \overline{\mathrm{P}_Z})$, with respect to the coordinate system $\overline{o}-\overline{x}-\overline{y}-\overline{z}$. When $\overline{\mathrm{P}_Y} > 0$, θ is less than 0; otherwise, $\theta \geq 0$.

Eq. (4.3) in the coordinate system $(\widetilde{r}, \widetilde{\varphi}, \widetilde{z})$ is rewritten as Eq. (4.11) in the cylindrical

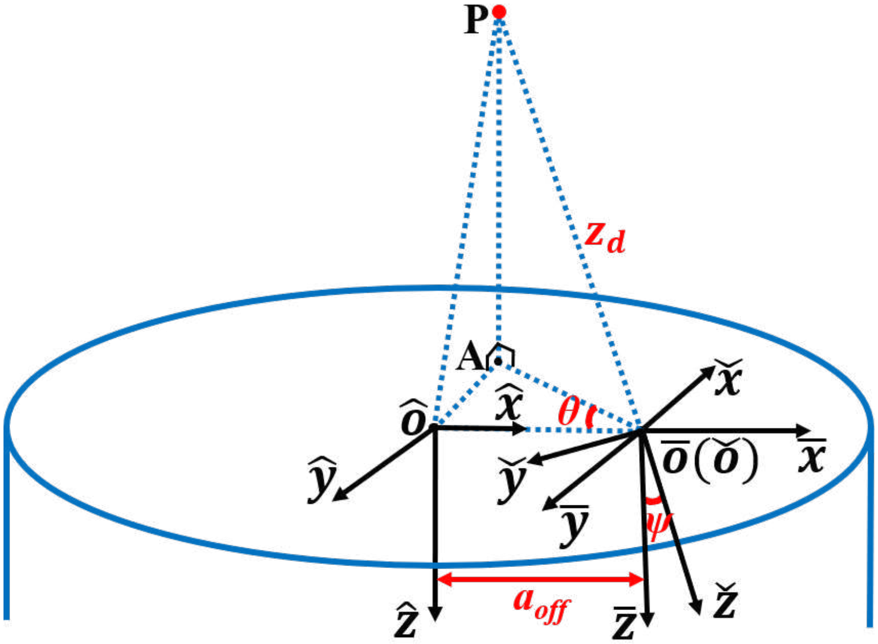

Fig. 4.3: The geometrical schematic diagram of beam launch. Point P is the center of the VCSEL, and Point A is the projection of P onto the fiber input facet. ψ is the incidence tilt angle between the $\hat{z}$-axis and the $\check{z}$-axis, and θ is the azimuthal tilt angle between the $\hat{y}$-axis and the $\check{y}$-axis.

coordinate system $(\hat{r}, \hat{\varphi}, \hat{z})$,

$$\widehat{LG}_h\left(\hat{r}, \hat{\varphi}, \hat{z}, \lambda\right) = \widetilde{LG}_h\left(\tilde{r}, \tilde{\varphi}, \tilde{z}, \lambda\right) \tag{4.11}$$

where

$$\tilde{r} = \sqrt{\tilde{x}^2 + \tilde{y}^2},$$

$$\tilde{x} = \hat{r}\sin\hat{\varphi}\cos\psi\sin\theta - \left(a_{off} - \hat{r}\cos\hat{\varphi}\right)\cos\psi\cos\theta - \hat{z}\sin\psi,$$

$$\tilde{y} = \left(a_{off} - \hat{r}\cos\hat{\varphi}\right)\sin\theta + \hat{r}\sin\hat{\varphi}\cos\theta,$$

$$\tilde{z} = \hat{z}\cos\psi - \left(a_{off} - \hat{r}\cos\hat{\varphi}\right)\sin\psi\cos\theta + \hat{r}\sin\hat{\varphi}\sin\psi\sin\theta + z_d,$$

$$\tilde{\varphi}=\begin{cases} \pi+\arctan\left(\dfrac{\tilde{y}}{\tilde{x}}\right), & \mathit{when}\ \tilde{x}<0 \\ \dfrac{\pi}{2}, & \mathit{when}\ \tilde{x}=0 \\ \arctan\left(\dfrac{\tilde{y}}{\tilde{x}}\right), & \mathit{when}\ \tilde{x}>0 \end{cases}.$$

Based on Eqs. (4.10) and (4.11), the coupling coefficient for the wavelength λ between the hth decentered and tilted LG mode and the uth MMF LP mode, $d_{hu}(\lambda)$, is expressed as Eq. (4.12).

$$d_{hu}\left(\lambda\right) = \int_0^{+\infty}\int_0^{2\pi}\widehat{LG}_h(\hat{r},\hat{\varphi},0,\lambda)\cdot\left[\widehat{MLP}_u(\hat{r},\hat{\varphi},\lambda)\right]^*\hat{r}d\hat{r}d\hat{\varphi} \tag{4.12}$$

The expansion of LG modes over the orthogonal MMF LP modes is obtained in Eq. (4.13),

$$\widehat{LG}_h(\hat{r},\hat{\varphi},0,\lambda) = \sum\nolimits_{u=1}^{N_{MLP}} d_{hu}(\lambda)\widehat{MLP}_u(\hat{r},\hat{\varphi},\lambda) + \sum\nolimits_{u=1+N_{MLP}}^{\infty} d_{hu}(\lambda)\widehat{MLP}_u(\hat{r},\hat{\varphi},\lambda) \tag{4.13}$$

where N_{MLP} denotes the number of guided LP modes propagating along MMF. The first term on the right-hand side of Eq. (4.13) indicates the guided LP modes, while the second term represents the lossy LP modes which powers radiate. It is worth mentioning that mode power distribution is independent of the coordinate system. Therefore, coupling coefficients c_{gh} are the same in the coordinate systems $(\tilde{r},\tilde{\varphi},\tilde{z})$ and $(\hat{r},\hat{\varphi},\hat{z})$. At the fiber facet $(\hat{r},\hat{\varphi},0)$, the expansion of the gth VCSEL LP mode over the MMF LP modes is expressed in Eq. (4.14).

$$\begin{aligned}\widehat{LP}_g(\hat{r},\hat{\varphi},\lambda_g) &= \textstyle\sum_{u=1}\sum_{h=1}\left(c_{gh}(\lambda_g)\cdot d_{hu}(\lambda_g)\cdot\widehat{MLP}_u(\hat{r},\hat{\varphi},\lambda_g)\right)\\ &= \textstyle\sum_{u=1} e_{gu}(\lambda_g)\cdot\widehat{MLP}_u(\hat{r},\hat{\varphi},\lambda_g)\end{aligned} \tag{4.14}$$

where $\sum_{h=1} c_{gh}d_{hu}$ can be defined as e_{gu}. As illustrated in Fig. 4.4, a power coupling coefficient (PCC) matrix, $\mathbf{H}'$, whose element is η_{gu}, is obtained, where η_{gu} is equal to $|e_{gu}|^2$. In addition, a corresponding wavelength matrix $\mathbf{\Omega}'$ is generated, where the element, Λ_{gu}, is equal to λ_g. In view of the large value of N_{MLP} (over 200 for 850 nm wavelength), the number of elements in $\mathbf{H}'$ and $\mathbf{\Omega}'$ is on the order of 10^3. As a result, tremendous computation cycles are needed to iterate each mode propagation. MMF modes are degenerated into mode groups, which are indexed by the principal mode number (PMN) $v = 2p' + |l'| - 1$. Fig. 4.5 depicts the MMF modes included in the first ten mode groups. Within the same mode group, modes share approximately the same propagation constant [131, 132].

A PCC matrix $\mathbf{H}$ with the element ξ_{gv} and a wavelength matrix $\mathbf{\Omega}$ with the element ζ_{gv} are built for each mode group. $\mathbf{H}'$ and $\mathbf{\Omega}'$ are converted into $\mathbf{H}$ and $\mathbf{\Omega}$ to express the coupling relation between VCSEL LP modes and MMF mode groups, as shown in Fig. 4.4. The number of guided mode groups N_{MG} is typically around 20 to 30. Therefore, the size of $\mathbf{H}$ and $\mathbf{\Omega}$ is only about 10% of that of $\mathbf{H}'$ and $\mathbf{\Omega}'$. The use of mode groups improves calculation efficiency of the proposed coupling model by approximately 90%. Due to nearly the same propagation characteristics of the degenerated modes, the use of mode groups

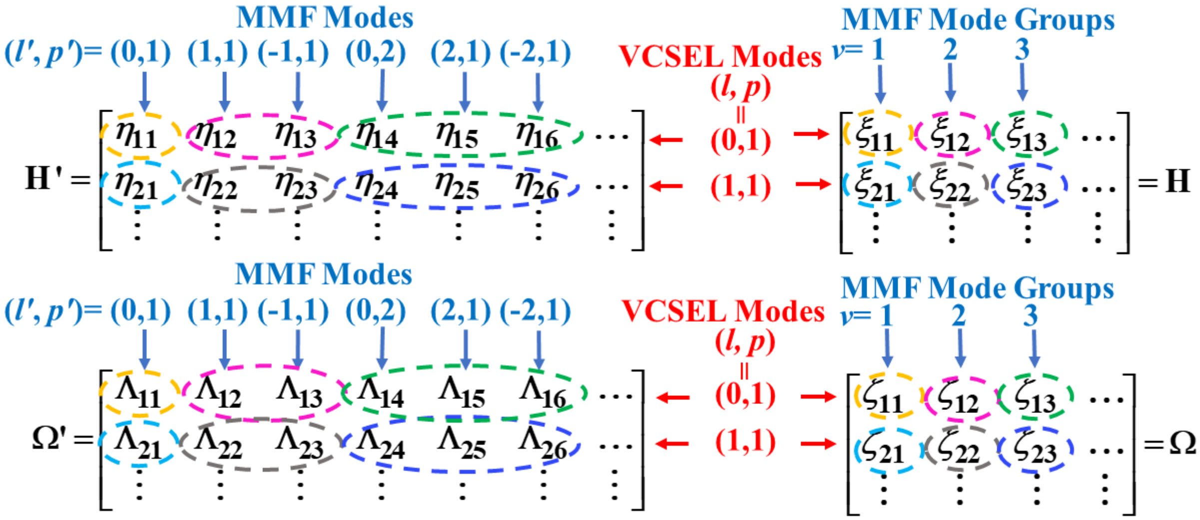

Fig. 4.4: The conversions of matrices $\mathbf{H}'$ to $\mathbf{H}$ and $\mathbf{\Omega}'$ to $\mathbf{\Omega}$. l and p are the azimuthal and radial indices of the VCSEL mode, while l' and p' are the azimuthal and radial indices of the MMF LP mode. v is the principal mode number of the MMF mode group. The element ξ of $\mathbf{H}$ is the summation of elements, η, circled by the same color in $\mathbf{H}'$; The elements in the gth row of $\mathbf{\Omega}'$ and $\mathbf{\Omega}$ are equal to λ_g.

maintains the computation accuracy very well, which is verified by works [133, 134].

4.4 MMF Model

Attenuation, dispersion, fiber mode mixing and mode partition noise (MPN) play significant roles in the signal distortion, especially in the VCSEL-based MMF link. Due to the MMF multimode excitation and the VCSEL multi-transverse-mode output, the model should include mode-dependence and wavelength-dependence of these effects. With a coherent source and mode-selective loss devices, it is worth pointing out that modal noise

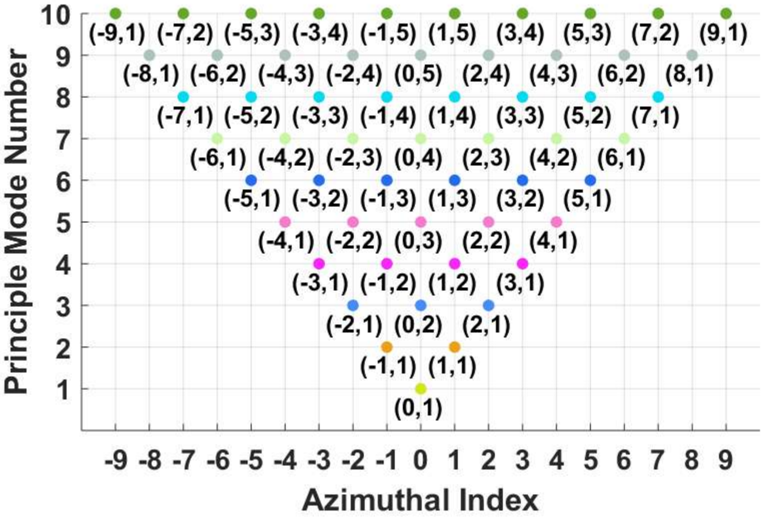

Fig. 4.5: The azimuthal and radial index distribution in the first ten MMF LP mode groups. The first and second element in the parentheses are the azimuthal and the radial indices, respectively.

may occurs when the link suffers from source frequency changes or environmental vibrations such as mechanical stress. Modal noise results in speckle pattern variations at the fiber output translating into signal-to-noise ratio fluctuations [135]. The model assumes no source frequency fluctuations nor environment vibrations; thus, modal noise is not studied.

Attenuation and fiber mode mixing lead to mode power fluctuation. As a result of intrinsic waveguide properties and material defects [136], LP modes experience differential mode attenuation, where higher-order modes suffer more loss. Eq. (4.15) defines the spectral-dependent modal attenuation for the vth MMF LP mode group excited by the gth VCSEL mode, γ_{gv}:

$$\gamma_{gv} = \gamma_0 + \gamma_0 \cdot \mathrm{I}_\rho \left(\eta \cdot \left(\frac{\zeta_{gv} v}{\pi R} \right)^{2\alpha/(\alpha+2)} \cdot \left[\frac{\alpha+2}{2\alpha} \cdot \frac{1}{n_1(\zeta_{gv})^2 - n_2(\zeta_{gv})^2} \right]^{\alpha/(\alpha+2)} \right) \tag{4.15}$$

where γ_0 is the attenuation per unit length of the fundamental mode, η is a weighting constant, ζ_{gv} is the wavelength element in the matrix Ω, $n_1(\zeta_{gv})$ and $n_2(\zeta_{gv})$ is the core peak RI and the cladding RI of the MMF, and $I_\rho(\cdot)$ is the ρth-order modified Bessel function of the first kind. Thus, the attenuated output power $P_{out(gv)}$, as a function of the transmission length z, is obtained as follows:

$$P_{out(gv)}(z) = P_g \cdot \xi_{gv} \cdot e^{-\gamma_{gv} z} \tag{4.16}$$

In addition to differential mode attenuation, fiber mode mixing phenomenon contributes to power transfers between modes, inducing mode power fluctuation as well as inter-symbol interference (ISI). Based on coupled power equations, fiber mode mixing is expressed by Eq. (4.17),

$$\frac{\partial P_{gu}^M}{\partial z} + \tau \frac{\partial P_{gu}^M}{\partial t} = \sum\nolimits_{\hat{u} \neq u} d_{u\hat{u}}^M \left(P_{g\hat{u}}^M - P_{gu}^M \right) \tag{4.17}$$

where P_{gu}^M is the power of the uth MMF LP mode induced by the gth VCSEL LP mode, $d_{u\hat{u}}^M$ is the coupling coefficient between the uth and $\hat{u}$th MMF LP modes [137, 138], and τ is the time delay of the uth MMF LP modes per unit fiber length. The superscript of P_{gu}^M and

$d^{M}_{u\hat{u}}$, M, denotes the MMF mode.

Eq. (4.17) aims at fiber modes, such that the simulation process calls this equation tens of thousands of times (in the order of 10^4). With today's computing capabilities, the computation load is important resulting in simulation time up to several hours. As modes within the same mode group exhibit the same transmission characteristics, after some mathematical operations, a modified steady-state coupled-power equation (4.18) is derived for the mode groups instead of Eq. (4.17),

$$\frac{\partial P^{G}_{gv}}{\partial z} = \sum_{\hat{v}\neq v} d^{G}_{v\hat{v}} \left(\frac{P^{G}_{g\hat{v}}}{N_{g,\hat{v}} - N_{g,\hat{v}-1}} - \frac{P^{G}_{gv}}{N_{g,v} - N_{g,v-1}} \right) \tag{4.18}$$

where P^{G}_{gv} represents the power of the vth mode group excited by the gth VCSEL LP mode, and $N_{g,v}$ denotes the number of modes within the first v mode groups. The superscript, G, represents the MMF mode group. $d^{G}_{v\hat{v}}$ expresses the coupling coefficient between the vth mode group and the $\hat{v}$th mode group, which is derived from $d^{M}_{u\hat{u}}$ following Eq. (4.19):

$$d^{G}_{v\hat{v}} = \sum_{u=(N_{g,v-1}+1)}^{N_{g,v}} \sum_{\hat{u}=(N_{g,\hat{v}-1}+1)}^{N_{g,\hat{v}}} d^{M}_{u\hat{u}} \tag{4.19}$$

While differential modal attenuation and fiber mode mixing influence the amplitude, modal dispersion and chromatic dispersion result in time delay difference, leading to ISI and MPN penalties. Using the well-known WKB (Wentzel-Kramers-Brillouin) analysis of the Helmholtz equation [139], the modal propagation constant, β_{gv}, is obtained using Eq.

(4.20).

$$\beta_{gv}\left(\zeta_{gv}\right) = \frac{2\pi n_1}{\zeta_{gv}} \sqrt{1 - \frac{{n_1}^2 - {n_2}^2}{{n_1}^2} \left[\frac{(\alpha+2)\cdot {\zeta_{gv}}^2 \cdot v^2}{\alpha \cdot 2\pi^2 R^2 \cdot ({n_1}^2 - {n_2}^2)} \right]^{\frac{\alpha}{\alpha+2}}} \tag{4.20}$$

It is worth noting that n_1 and n_2 are wavelength-dependent as well based on the Sellmeier equation. The modal delay per unit length, t_{gv}^m is proportional to the first-order derivative of β_v,

$$t_{gv}^m = -\frac{\lambda^2}{2\pi c} \frac{d\beta_{gv}(\lambda)}{d\lambda} \bigg|_{\lambda=\zeta_{11}} \tag{4.21}$$

where c is the speed of light in vacuum.

Due to the multi-transverse-mode nature of the VCSEL, its output shows a relatively wide spectrum as seen in Fig. 4.1. The chromatic dispersion is usually neglected for the low-speed data rate transmission because the chromatic delay is far less than the bit period; however, it is of vital significance for the performance evaluation of the next-generation high-speed ($\geq$ 10 Gbps) VCSEL-MMF interconnects [133, 140]. The chromatic delay per length,t_{gv}^c, is expressed in (22),

$$t_{gv}^c = \frac{S_0}{4} \left[\frac{{\zeta_{gv}}^4 - {\lambda_0}^4}{{\zeta_{gv}}^3} \right] \left(\zeta_{gv} - \zeta_{11}\right) \tag{4.22}$$

where λ_0 is the zero-dispersion wavelength, and S0 is the zero-dispersion slope. With the interaction of the modal and chromatic dispersion, the total delay, t_{gv}, is equal to $t_{gv}^m + t_{gv}^c$.

Mode competition among the lasing transverse modes of a multimode VCSEL contributes to random correlated fluctuations in the mode powers. In the dispersive fiber link, the time delay induced by dispersion effects de-correlates VCSEL modes, resulting in MPN. The standard deviation of MPN, σ_{MPN}, is expressed below [86],

$$\sigma_{MPN}{}^{2} = \kappa_{MPN}{}^{2} \cdot \left\{ \sum\nolimits_{g} a_{g} \left[F_{g}\left(t\right) \right]^{2} - \left[\sum\nolimits_{g} a_{g} F_{g}\left(t\right) \right]^{2} \right\} \tag{4.23}$$

where κ_{MPN} is the mode partition parameter. F_g is the signal waveform carried by the gth VCSEL mode after propagation over the fiber, and it is given as

$$F_{g}\left(t\right) = \sum\nolimits_{v=1}^{N_{MG}} \xi_{gv} f_{g}\left(t - \tau_{gv}\right) \tag{4.24}$$

where ξ_{gv} is the power coupling coefficient from matrix $\mathbf{H}$, τ_{gv} is the temporal delay of the modulated signal induced by the MMF dispersion after fiber transmission, and f_g is the waveform before coupling to the MMF fiber for a given sequence.

A highly-efficient and highly-accurate fiber effect simulation approach, named split-step small-segment (4-S) method, is proposed to emulate the signal evolution along the MMF, as illustrated in Fig. 4.6(a). Using the 4-S method, the MMF fiber is equally divided into Ns segments with an identical length of Δz. The algorithm steps, outlined in the flowchart of Fig. 4.6(b), are implemented as follows:

Step 1: At the fiber input facet, the transmission distance, z, is 0, where the power of the vth MMF mode group excited by the gth VCSEL mode is $a_g \xi_{gv}$;

Step 2: the first MMF mode group excited by the first VCSEL mode is selected;

Step 3: the selected mode group propagates over the first half of the small segment with the length of $\Delta z/2$, while only the mode mixing effect is numerically calculated;

Step 4: at the mid-point of the segment, attenuation and dispersion effects over the whole segment are imposed;

Step 5: the mode group propagates over the second half of the segment, while only the mode mixing is considered;

Step 6: the steps 3 to 5 are repeated until all MMF mode groups for all wavelengths are iterated over;

Step 7: the steps 2 to 6 are repeated over the next segments until the light reaches the fiber output facet;

Step 8: MPN is determined by Eqs. (4.23) and (4.24).

The error of the 4-S method is positively correlated with Δ_z; however, the computational cost is inversely proportional to Δ_z. Therefore, a shorter segment results in a more accurate result, while the simulation time increases. In our model, the small segment Δ_z is chosen as one-twentieth of the fiber length for the tradeoff between high accuracy and low computation burden. With this small segment, the simulation can reproduce the measurement satisfactorily as seen in Section 4.6.

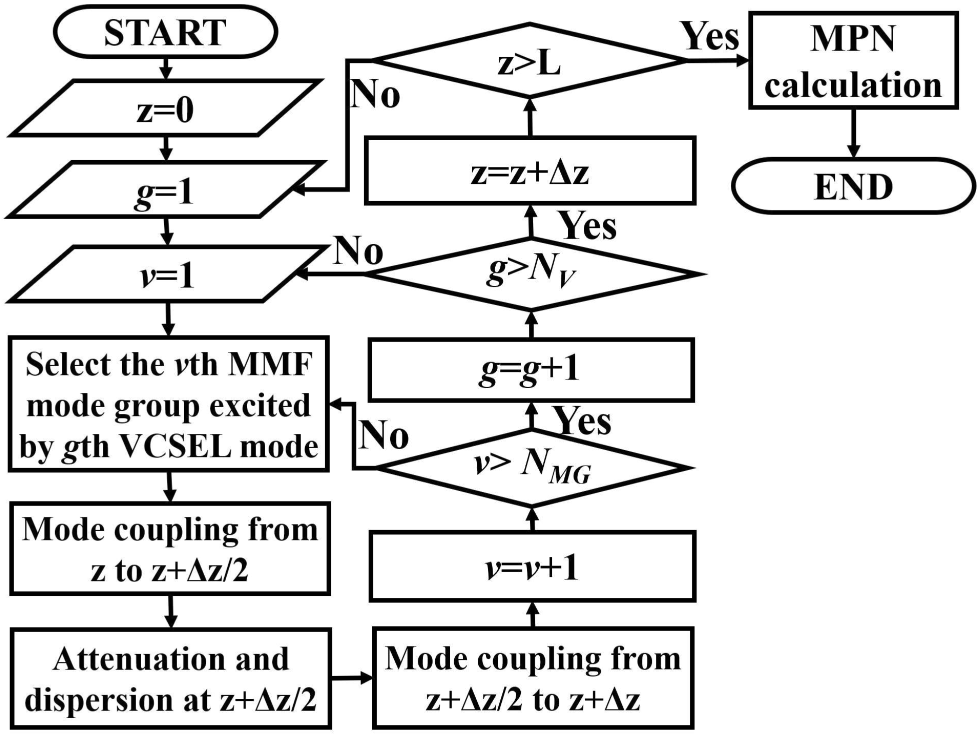

Fig. 4.6: (a) Illustration of the split-step small-segment (4-S) method. The fiber length L is divided into several small segments with the length of Δ_z. (b) The flowchart describes the 4-S method, where N_V is the number of VCSEL modes, and N_{MG} is the number of guided MMF mode groups.

4.5 MMF-PD Coupling Model and PD Model

A photodiode (PD) detects and demodulates the optical signal after fiber transmission. The beam coupling into the PD after the MMF influences the photocurrent magnitude, inducing the signal-to-noise ratio variation. In addition, the coupling between the MMF and the PD significantly affects the channel crosstalk in mode-group-division-multiplexing (MGDM) systems [121]. Due to the multimode VCSEL output and its wide spectrum, the PD model used in the VCSEL-MMF link should be wavelength-sensitive for high simulation accuracy. Fig. 4.7(a) shows the beam propagation from the MMF output facet to the active area of PD. The cylindrical coordinate system $(\widehat{\hat{r}}, \widehat{\hat{\varphi}}, \widehat{\hat{z}})$ is built at the fiber output facet. Its origin $\widehat{\hat{o}}$ is at the facet center, and $\widehat{\hat{z}}$-axis directs towards the outside of the fiber along the fiber axis. The coordinate systems $(\widehat{\hat{r}}, \widehat{\hat{\varphi}}, \widehat{\hat{z}})$ and $(\hat{r}, \hat{\varphi}, \hat{z})$ meet the following relations: $\hat{r} = \widehat{\hat{r}}$, $\hat{\varphi} = \widehat{\hat{\varphi}}$, and $\hat{z} = \widehat{\hat{z}} + L$. The MMF LP mode profile is described by Eq. (4.10), and Eq. (4.3) expresses the free-space LG mode after fiber to characterize beam diffraction. Using Eqs. (4.3) and (4.10), at the fiber output facet, the coupling coefficient between the uth guided MMF LP mode excited by the gth VCSEL mode and the wth free-space LG mode, denoted as f_{guw}, is given by the overlap integral as follows:

$$f_{guw} = \int_0^{+\infty} \int_0^{2\pi} \widehat{MLP}_u \left(\hat{\hat{r}}, \hat{\hat{\varphi}}, \Lambda_{gu}\right) \cdot \left[\widetilde{LG}_w \left(\hat{\hat{r}}, \hat{\hat{\varphi}}, 0, \Lambda_{gu}\right)\right]^* \hat{\hat{r}} d\hat{\hat{r}} d\hat{\hat{\varphi}} \tag{4.25}$$

where Λ_{gu} is the element from the mode wavelength matrix Ω', due to the wavelength stability during fiber propagation. Based on the orthogonality of the generalized Laguerre polynomials [[141], Eq. 7.414], the LG modes after the MMF, $\widetilde{\mathrm{LG}}_{\mathrm{w}}$, have a waist of $\omega_0 = \mathrm{R}\sqrt{2/\mathrm{V}\left(\lambda\mathrm{g}\right)}$, where R is the fiber core radius. This simplifies the expansion of MMF LP mode profiles over LG modes. Consequently, the MMF LP mode with the azimuthal index l' and the radial index p' is fully coupled onto the free-space LG mode with the radial and azimuthal indices n and m if the relations $m = l'$ and $n = p' - 1$ are satisfied.

A new cylindrical coordinate system ($\tilde{\tilde{r}}$, $\tilde{\tilde{\varphi}}$, $\tilde{\tilde{z}}$) is built at the PD, where the axes $\tilde{\tilde{r}}$ and $\tilde{\tilde{\varphi}}$ are located at the surface of the PD active area, and the pole $\tilde{o}$ is at the center. Under this system, Eq. (4.26) expresses the electrical field for the wavelength λ_g at the PD surface,

$$E_{PD(g)}\left(\tilde{\tilde{r}},\tilde{\tilde{\varphi}}\right)=\sum\nolimits_{u}\sum\nolimits_{w}\left[E_{gu}\left(t-\tau_{gu}\right)\cdot e^{-i\cdot\beta_{gu}\cdot L}\cdot f_{guw}\cdot\widehat{LG}_{w}\left(\tilde{\tilde{r}},\tilde{\tilde{\varphi}},d_{pd},\Lambda_{gu}\right)\right] \tag{4.26}$$

where E_{gu} is the waveform carried by the uth guided MMF LP mode, τ_{gu} is the relative time delay of the uth mode induced by modal and chromatic dispersion after fiber propagation, d_{pd} is the beam transmission distance between the MMF and the PD surface, and β_{gu} is the propagation coefficient.

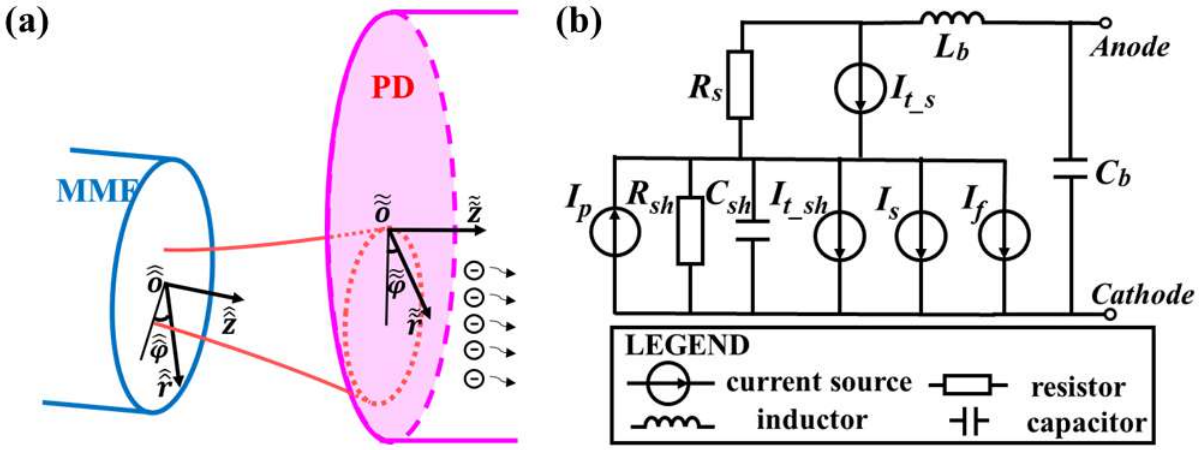

Fig. 4.7: (a) Beam launch with misalignment between the MMF and the PD. ($\hat{r}, \hat{\varphi}, \hat{z}$) and ($\tilde{\tilde{r}}$, $\tilde{\tilde{\varphi}}$, $\tilde{\tilde{z}}$) are cylindrical coordinate systems. The purple region represents the PD active area where photons are converted into electrons. (b) The equivalent circuit model of a PIN photodiode.

The wavelength-dependent responsivity of a PIN photodiode, R_{pd}, is modeled as follows,

$$R_{pd}(\lambda) = \frac{\eta_{pd} q \lambda}{2\pi \hbar c} \tag{4.27}$$

where η_{pd} is the quantum efficiency, q is the electron charge, $\hbar$ is reduced Planck constant. Therefore, the photocurrent is

$$I_p = \sum_{g=1}^{N_V} \left[R_{pd}\left(\lambda_g\right) \cdot \int_0^{r_{pd}} \int_0^{2\pi} \left| E_{PD(g)}\left(\tilde{\tilde{r}}, \tilde{\tilde{\varphi}}\right) \right|^2 \tilde{\tilde{r}} d\tilde{\tilde{r}} d\tilde{\tilde{\varphi}} \right] \tag{4.28}$$

where N_V is the number of VCSEL modes, and r_{pd} is the radius of the PD active area. A spectral-dependent equivalent circuit model of the photodiode with noise effects describes the behavior of a PIN photodiode, as shown in Fig. 4.7(b). R_{sh} and C_{sh} denote the shunt junction resistance and capacitance, R_S models the contact resistance, L_b and C_b are the parasitic inductance and capacitance due to the bond wires. The noise currents consist of four sources: the shunt-resistance thermal noise I_{t_sh}, the series-resistance thermal noise I_{t_s}, the shot noise I_s and the flicker noise I_f, which variances are expressed as (4.29)–(4.32), respectively:

$$\left\langle {I_{t\_sh}}^2 \right\rangle = \frac{4kT\Delta f}{R_{sh}} \tag{4.29}$$

$$\left\langle {I_{t\_s}}^2 \right\rangle = \frac{4kT\Delta f}{R_s} \tag{4.30}$$

$$\left\langle {I_s}^2 \right\rangle = 2q(I_d + I_p)\Delta f \tag{4.31}$$

$$\left\langle {I_f}^2 \right\rangle = \frac{K_f {I_d}^{\varepsilon_f} \Delta f}{{f_e}^{\gamma_f}} \tag{4.32}$$

where k is the Boltzmann constant, T is the device temperature, K_f is the flicker noise coefficient, I_d is the dark current, f_e is the frequency at which the noise is measured, ε_f is the flicker noise exponent, γ_f is the flicker noise frequency coefficient and Δf is the bandwidth of the photodiode.

4.6 Experimental Validation

A comprehensive spectral-dependent link model is presented, where the offset condition and 3-dimension tilt conditions are simultaneously considered. The model is developed within a commercial Cadence tool suite, so that the modular extension can be realized easily by designers to verify the performance of the targeted device. The simulation results and experimental validation will be given in this section.

An experimental setup is built on a vibration-isolated optical table to validate the model, as depicted in Fig. 4.8. First, a bias-tee is employed to combine the bias current and the high-speed signal generated by the pulse pattern generator (PPG). After the bias-tee, a wire-bonded 850 nm VCSEL chip (manufactured by II-VI Incorporated) is driven by the biased signal. The VCSEL beam is butt-coupled into the OM4 MMF, using a 6-axis micro-positioning stage to tune the relative position between the VCSEL and the MMF. After transmission over the MMF, the beam profiles and eye diagrams are

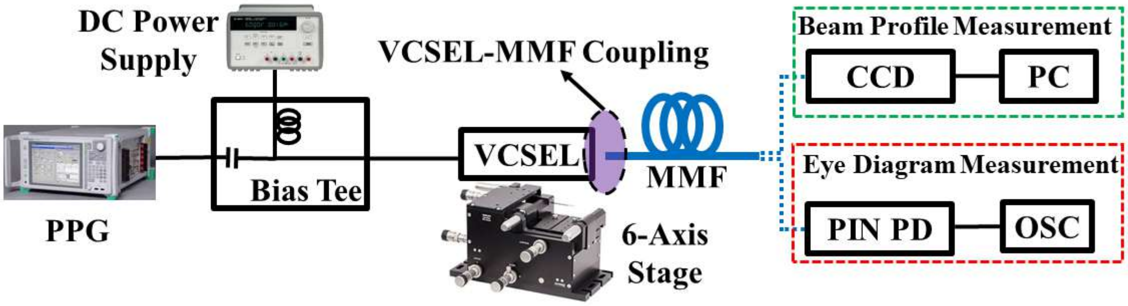

Fig. 4.8: Experiment schematic. DC: direct current; PPG: pulse pattern generator; CCD: charge-coupled device; PC: personal computer; OSC: oscilloscope.

measured, respectively. For beam intensity profile measurement, a charge-coupled device (CCD) camera beam profiler (Thorlabs BC106-VIS), located after the MMF, is used to detect the beam intensity profiles. To minimize mode-dependent fiber effects and maximize the influence of the launch condition, a back-to-back (B2B) configuration is employed with a short MMF of 1 meter. For eye diagram measurements, the light is fully coupled to the PD active region without misalignment. The oscilloscope (OSC) is synchronized in time with the PPG. The data signal is then analyzed on an oscilloscope.

The beam profiles in the top row of Fig. 4.9 are obtained from experiments, while those in the bottom row of Fig. 4.9 are the simulation results. The measurement and simulation show visually similar spatial beam intensity distribution to prove that the model is able to evaluate the guided fiber modes for different beam launch conditions. Their discrepancies are attributed to VCSEL polarization instability [142], imperfect parallelism between the VCSEL aperture and the CCD sensing surface, the CCD camera resolution, and the stray light. The donut profile in Fig. 4.9(a) has a dispersed intensity distribution over the CCD camera, thus it is more sensitive to these adverse impacts.

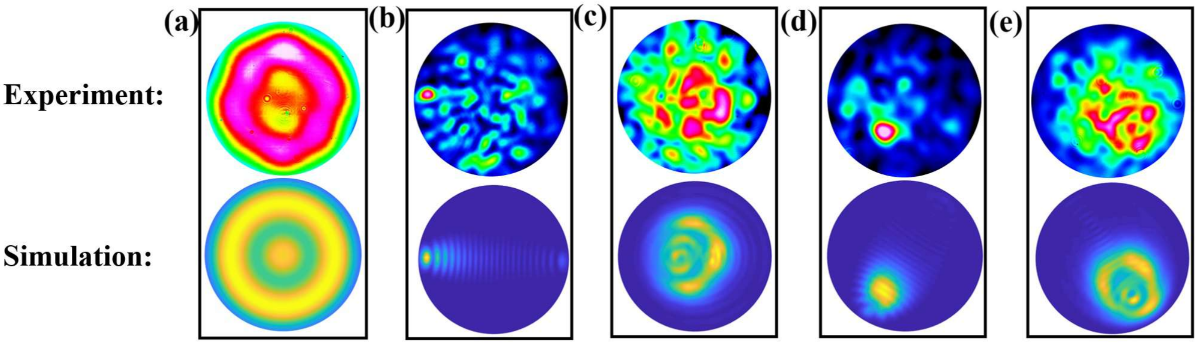

Fig. 4.9: (a): The beam intensity profile at the fiber input facet. (b)-(e): The intensity profiles of guided modes excited by different launch conditions at the fiber output facet. The launch conditions are: (b) a_{off} is $0\,\mu$m, ψ is 20° and θ is 0°; (c) a_{off} is $10\,\mu$m, ψ is 10° and θ is 0°; (d) a_{off} is $10\,\mu$m, ψ is 20° and θ is 45°; (e) a_{off} is $10\,\mu$m, ψ is 10° and θ is 90°. The top figures in (a)-(e) are the experimental results; the bottom ones present the simulation results.

Utilizing the Cadence Tool Suite (Virtuoso Environment 5.10.41), the VCSEL-MMF link is simulated based on the proposed model. The parameters used in the simulation are summarized in Table 4.1, which values are extracted from the devices' datasheets, publications [86, 111, 126, 132, 143, 144], experimental measurement, and parameter fitting.

In the experimental setup, multimode fibers manufactured by Corning Inc., with the length 100 m and 200 m, are used for the transmission. A 25 Gbps PRBS7 NRZ signal is generated by the pulse pattern generator (Anritsu MU181020A) combined with a multiplexer (Anritsu MU1813A). Eye diagrams for center launch (no tilt nor offset) in experiments and

Table 4.1: Parameters Used in the Simulation.

Symbol	Description	Value	Symbol	Description	Value
a_v	VCSEL oxide aperture radius	3μm	λ_c	Central wavelength	852 nm
n_a	VCSEL core RI	3.6	r_{pd}	PD active area radius	40μm
n_c	VCSEL cladding RI	3.59	η_{pd}	Quantum efficiency	0.87
R	GI-MMF core radius	25μm	R_S	PD contact resistance	$0.72m\Omega$
n_1	GI-MMF core peak RI	1.47 (at 850 nm)	R_{sh}	PD shunt junction resistance	$430k\Omega$
n_2	GI-MMF cladding RI	1.45 (at 850 nm)	C_{sh}	PD shunt junction capacitance	0.18 pF
α	RI profile parameter	2	C_b	PD parasitic capacitance	98 fF
γ_0	Attenuation coefficient	$0.53\times10^{-3}/m$ (at 850 nm)	L_b	PD parasitic inductance	0.44 nH
ρ	Order of Bessel function	9	I_d	Dark current	0.1 nA
η	Attenuation weighting constant	7.35	K_f	Flicker noise coefficient	1×10^{-12}
S_0	Zero-dispersion slope	0.101 ps/(nm^2·km)	ε_f	Flicker noise exponent	1
λ_0	Zero-dispersion wavelength	1310 nm	γ_f	Flicker noise frequency coefficient	1
κ_{PMN}	Mode partition parameter	0.03			

simulations are shown in Fig. 4.10. Fig. 4.11 plots peak-to-peak jitters, bit error rates (BERs) and eye-opening ratios versus fiber lengths. In the experiment, the peak-to-peak jitters are 13.9 ps, 16.5 ps and 20.0 ps for the back-to-back, 100 m and 200 m transmission, respectively, while the corresponding jitters are 14.1 ps, 16.6 ps and 19.8 ps in the simulation.

The experimental BERs are 3.3×10^{-7}, 5.3×10^{-6}, and 1.3×10^{-4} for the B2B, 100 m and 200 m transmission, while BERs in the simulation are 3.5×10^{-7}, 5.4×10^{-6}, and 1.3×10^{-4}. The BER values are limited by the parasitic bandwidth of the wired-bonded VCSEL [14] and expect to have lower values using the large-bandwidth VCSELs [4, 145]. The eye-opening ratio is an important metric to show the eye diagram quality [146, 147]. The vertical eye-opening ratio (a ratio of the eye height to the amplitude difference between one and zero logical levels) measured in the experiment are 0.379, 0.287 and 0.170 for the B2B, 100 m and 200 m transmission, while the simulation results are 0.382, 0.289 and 0.167. The horizontal eye-opening ratios normalized to the unit interval are 0.653, 0.588 and 0.500 for the B2B, 100 m and 200 m transmission, while the simulation results are 0.648, 0.585 and 0.505. The experiment and simulation have satisfactory match, which validates that the proposed model have strong ability to predict the transmission performance.

To validate the launch condition sensitivity of the proposed model, a coupling condition is realized with $a_{off} = 10\,\mu$m, $\psi = 20°$ and $\theta = 45°$. Fig. 4.12 shows the eye diagrams for the center launch and the given launch. Due to misalignment, the amplitude of the PD output signal is approximately 25 mV, less than 110 mV relative to the center launch. However, fewer modes are excited so that mode-dependent signal distortion is effectively suppressed. With the fiber length 200 m, the experimental BER is 2.3×10^{-6}, while the simulation result is 2.5×10^{-6}. The experimental vertical eye-opening ratio is 0.337 and the horizontal eye-opening ratio normalized by the unit interval is 0.631. The values of 0.331 for the vertical eye-

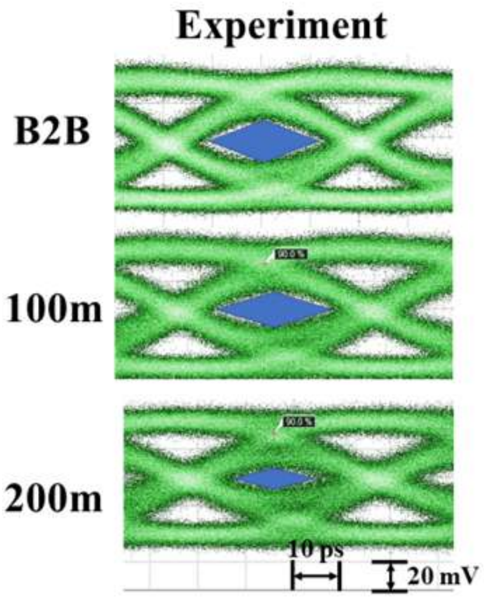

Fig. 4.10: Eye diagrams for B2B, 100 m, and 200 m transmission. a_{off} is 0μm, ψ is 0° and θ is 0°.

opening ratio and 0.636 for the horizontal eye-opening ratio are obtained in the simulation. The peak-to-peak timing jitter values in the measurement and simulation are 14.8 ps and 14.5 ps, respectively. The simulation results match the experiment and validate the ability of the model to simulate the transmission performance with arbitrary launch conditions. The mode power distributions under the center launch and the given misalignment launch are shown in Fig. 4.13. Compared to the center launch, the misalignment launch improves the transmission performance, but the additional attenuation resulting from coupling loss needs to be compensated.

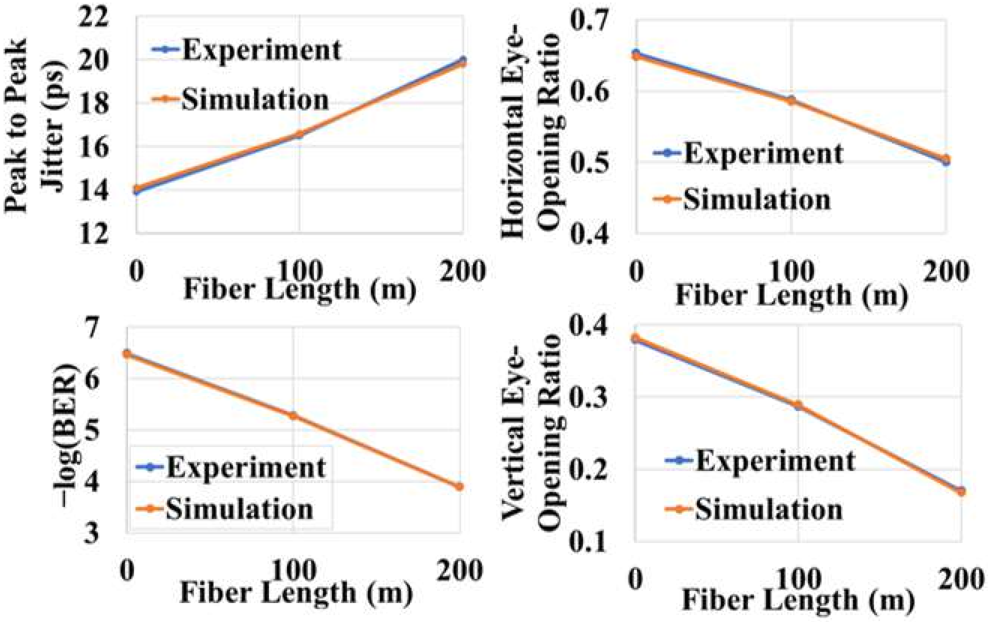

Fig. 4.11: The fiber length versus jitters, BERs, and eye-opening ratios in the experiment (in orange) and simulation (in blue).

4.7 Impact of Launching Conditions on Mode Power Distribution

Mode power distribution (MPD) is of vital significance due to mode-dependent propagation characteristics over the MMF. When different launch conditions are applied, the model can evaluate the corresponding MPD and determine the optimum coupling scheme of VCSEL-MMF links. In Fig. 4.14, mode power distributions induced by a multimode VCSEL are shown, with only the radial offset a_{off} included. With an increase in radial offset, higher-order mode groups obtain more power, which matches our expectation for the

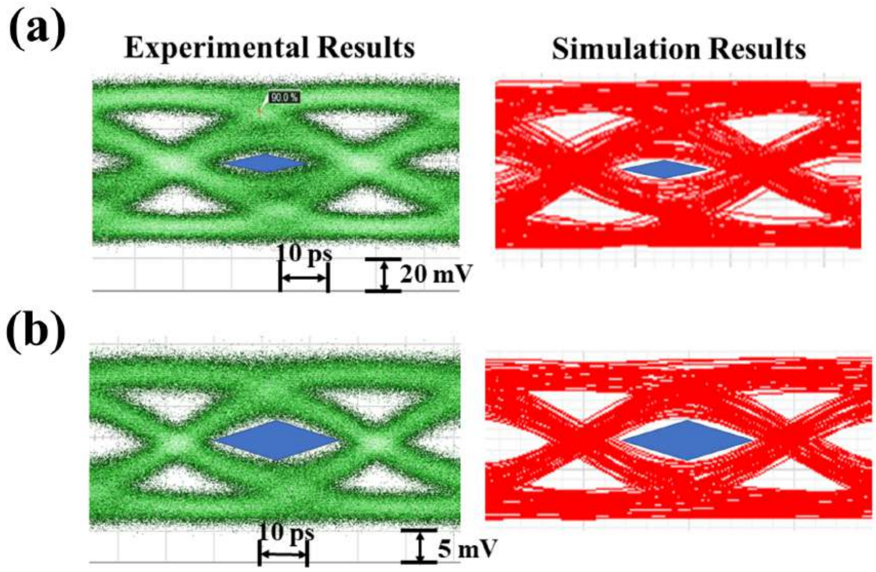

Fig. 4.12: (a) Eye diagrams for 200 m transmission where a_{off} is 0 μm, ψ is 0° and θ is 0°. (b) Eye diagrams for 200 m transmission where a_{off} is 10 μm, ψ is 20° and θ is 45°.

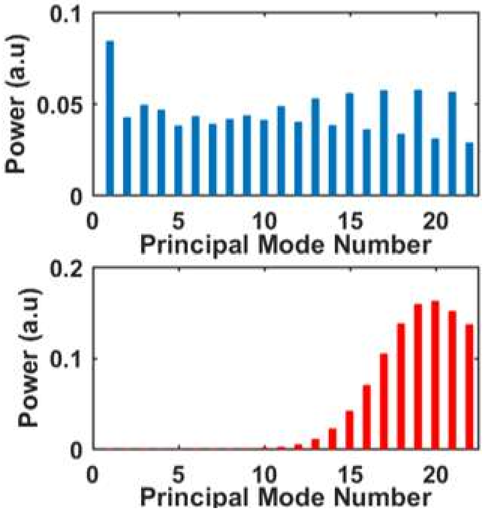

Fig. 4.13: Mode power distribution at the fiber input facet. The top plot refers to the center launch, while the bottom one corresponds to the misalignment launch with $a_{off} = 10\,\mu$m, $\psi = 20°$ and $\theta = 45°$.

offset excitation. Fig. 4.15 shows the effective modal bandwidths for different radial offsets without including fiber mode mixing and MPN. The horizontal axis is normalized to the bandwidth-distance product of the center launch. Compared to the center launch, the bandwidth-distance product of the MMF link has a 1.1-fold, 1.4-fold and 1.8-fold improvement for radial offsets of 10 μm, 15 μm and 20 μm, respectively. MPD patterns of

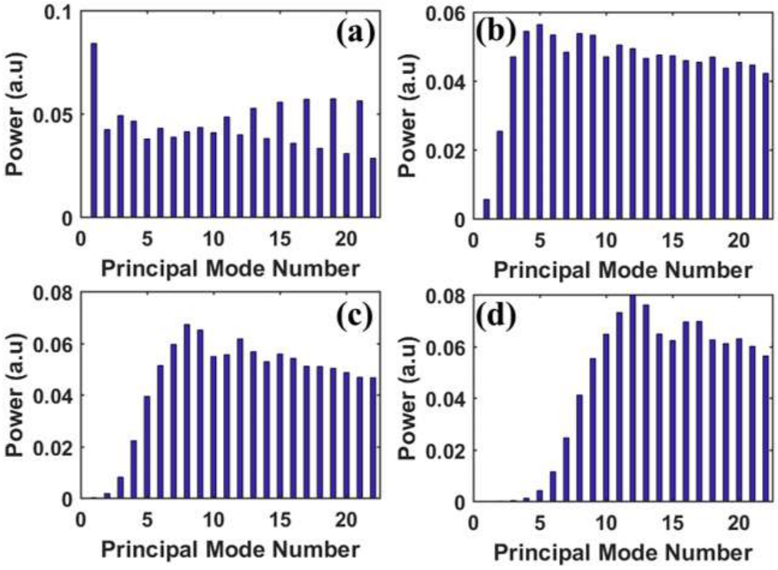

Fig. 4.14: (a)-(d) The mode power distribution only with the radial offset: (a) The offset is 0 μm (center launch); (b) the offset is 10 μm; (c) the offset is 15 μm; (d) the offset is 20 μm.

purely angular launch are shown in Fig. 4.16 for angular tilts of 0°, 5°, 10° and 15°. When ψ is 15°, low-order mode groups vanish, and the power concentrates on high-order guided mode groups. As a result, the bandwidth-distance product improves by 3.5-fold as seen in Fig. 4.17. Based on Fig. 4.15 and Fig. 4.17, the tilt tuning plays a better role for the control of selective mode excitation, due to the limited impact of radial offsets.

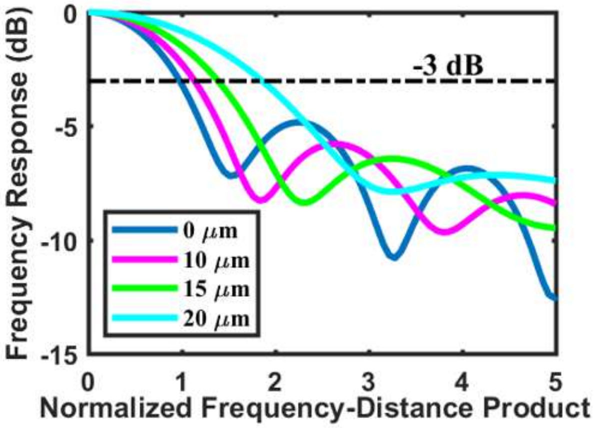

Fig. 4.15: The frequency response for different radial offsets.

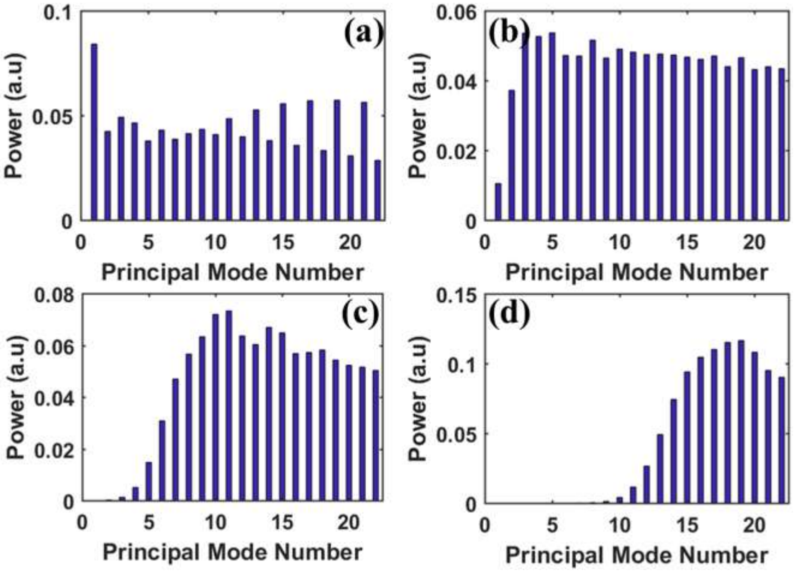

Fig. 4.16: (a)-(d) The mode power distribution only with tilt ψ: (a) ψ is 0° (center launch); (b) ψ is 5°; (c) ψ is 10°; (d) ψ is 15°.

When the radial offset a_{off} and the tilt ψ are simultaneously changed, the MPD can be optimally controlled. MPD figures are plotted in Fig. 4.18 (a)-(c) and (d)-(f). In (a)-(c), a_{off} is fixed at $10\,\mu$m, and the values of ψ are 5°, 10° and 15°, respectively. With the

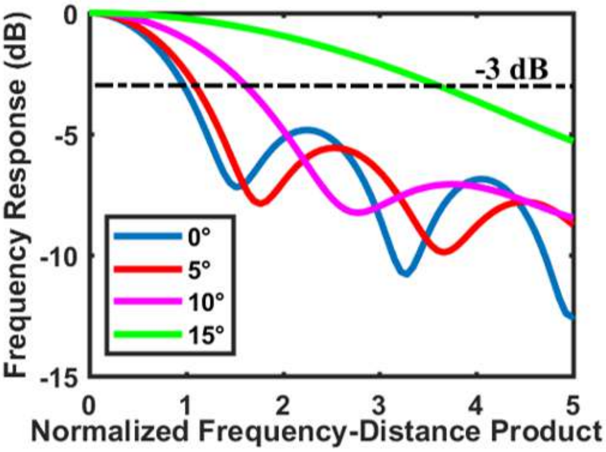

Fig. 4.17: The frequency response for different angular tilts.

same radial offset, higher-order mode groups are excited with a larger ψ, which matches the conclusion of purely angular launch. This result is explained by the fact that the input beam has a better overlap with the high-order MMF modes for large angular tilts. However, the improvement of the bandwidth-distance product for 15° is only 1.5-fold over the center launch. In (d)-(f), the tilt ψ is fixed to 10°, and a_{off} is varied to $5\,\mu$m, $10\,\mu$m, and $15\,\mu$m, respectively. The lower-order mode groups obtain even more portion of power for a larger radial offset. Therefore, the bandwidth-distance product decreases with the radial offset increasing, as shown in Fig. 4.19(b). The reason is that the radial offset is counteracted by the angular tilt misalignment, which implies the combination of a radial offset and an angular tilt does not necessarily result in expected high-order-mode excitation.

Finally, Fig. 4.20 shows MPD patterns, with a radial offset a_{off}, tilt ψ, and tilt θ concurrently analyzed. a_{off} is fixed at $10\,\mu$m; ψ is fixed at 10°; the values of θ are 45°, 90°,

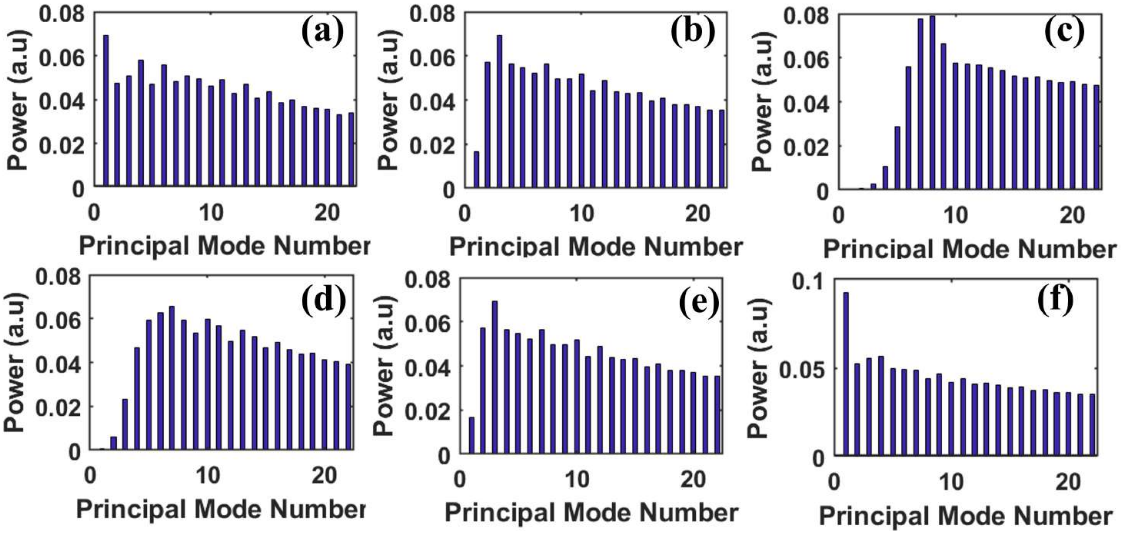

Fig. 4.18: (a)-(c) The mode power distribution with a fixed radial offset of 10 μm and varied tilts ψ: (a) ψ is 5°; (b) ψ is 10°; (c) ψ is 15°. (d)-(f) The mode power distribution with a fixed angular tilt (10°) and changed radial offsets: (d) a_{off} is 5 μm; (e) a_{off} is 10 μm; (f) a_{off} is 15 μm.

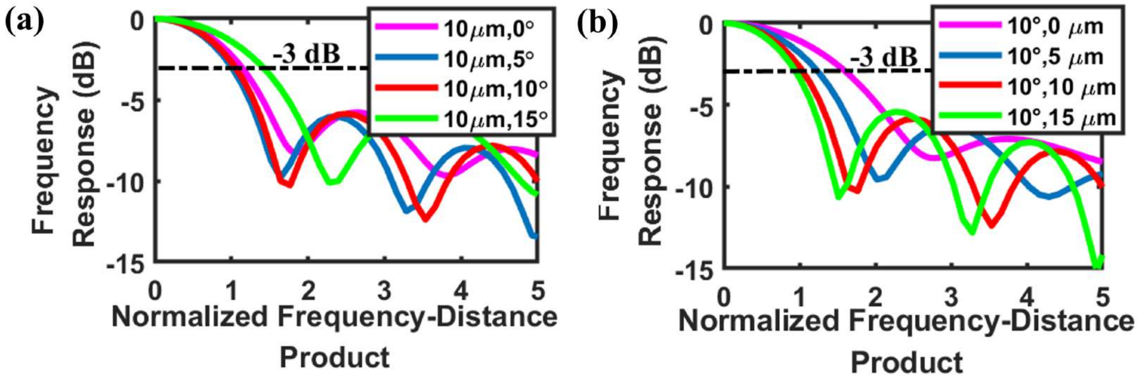

Fig. 4.19: (a) The corresponding frequency response for different angular tilts. (b) The corresponding frequency response for different radial offsets.

135° or 180°. Higher-order mode groups are excited by a larger tilt θ. The modal bandwidths under these launch conditions are shown in Fig. 4.21(a). The bandwidth-distance product

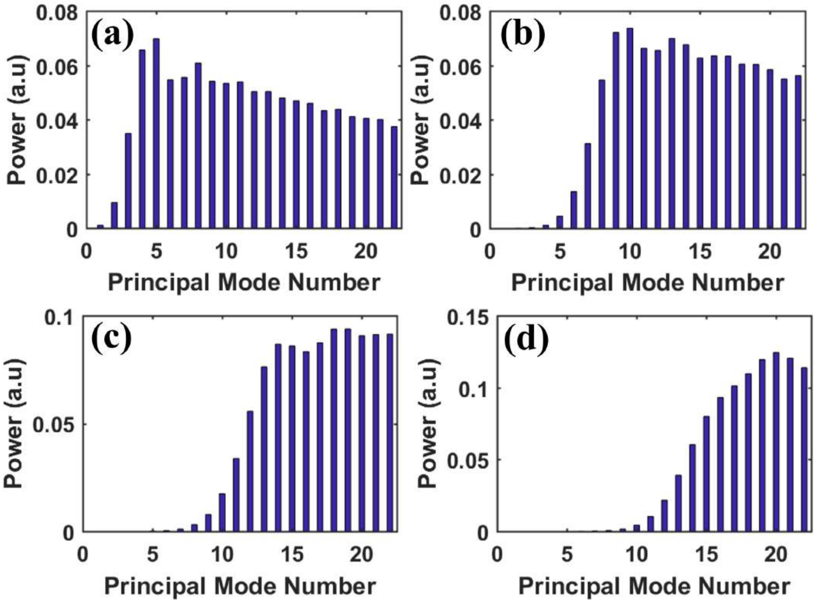

Fig. 4.20: (a)-(d) The mode power distribution with a_{off} , ψ and θ concurrently analyzed: (a) a_{off} is 10 μm, ψ is 10° and θ is 45°; (b) a_{off} is 10 μm, ψ is 10°, and θ is 90°; (c) a_{off} is 10 μm, ψ is 10° and θ is 135°; (d) a_{off} is 10 μm, ψ is 10° and θ is 180°.

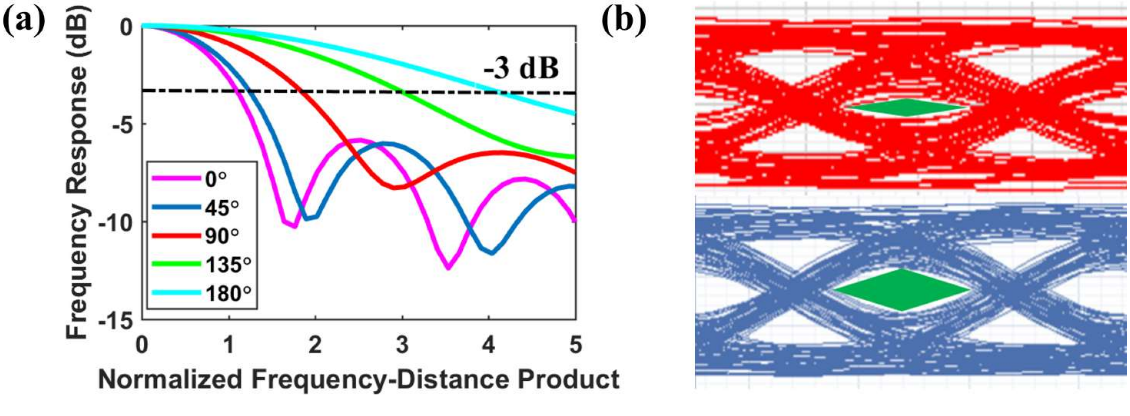

Fig. 4.21: (a) The frequency response for different θ values. (b) Eye diagrams of 25 Gbps NRZ after 200 m transmission. The launch conditions are: (top) a_{off} =10 μm, ψ=10°, θ =0°; (bottom) a_{off} =10 μm, ψ=10°, θ =180°.

increases with the increasing value of θ. When a_{off} is $10\,\mu$m, ψ is 10° and ψ is 180°, the bandwidth-distance product has a 3.8-fold improvement over the center launch. The additional coupling loss is 4.5 dB of due to lower coupling efficiency from the laser to the fiber. Fig. 4.21(b) displays simulated eye diagrams for 25 Gbps NRZ transmission over 200 m fiber length, with ψ of 0° (corresponding to the magenta curve in Fig. 4.21(a)) and 180° (corresponding to the aqua curve). The vertical and horizontal eye-opening ratios of the top eye diagram are 0.17 and 0.56, respectively. The bottom one is more widely open by virtue of better selective mode excitation, with the vertical eye-opening ratio of 0.32 and the horizontal eye-opening ratio of 0.62. The results are based on simulation only and provide a sense of the possible improvement in the frequency-distance curves with respect to launch conditions.

4.8 Conclusion

A spectral-dependent VCSEL-MMF link model is proposed for the next-generation high-speed interconnects. Spectral-dependent coupling analysis is realized with the offset and tilt angles included. The coupling model is sensitive to mechanical misalignments (radial offset, axial offset, and 3-dimensional tilt) and optical spectra. With mode-dependent fiber effects explained, the signal evolution over the MMF is simulated by an advanced split-step small-segment method. In addition, the equivalent circuit model of a wavelength-sensitive PD, matching the multi-wavelength characteristic of the VCSEL, realizes opto-electric conversion. The link model is validated using a 25 Gbps NRZ transmission experiment. Measured eye diagrams and bit error rates show good agreement with the simulation. While small-signal measurements have not been done, it is considered in future work. A CMOS-compatible electronic-photonic simulation platform is built in Cadence tool suits to help users design their devices. The model verifies that the misalignment launch can improve the effective modal bandwidth greatly compared to the conventional center launch (e.g. 3.8-fold improvement with a_{off} of $10\,\mu$m, ψ is 10° and θ is 180°), although the concomitant additional attenuation needs compensation. As one of the applications, it can be used to explore the optimum 3-D coupling solution of VCSEL-MMF links. With the transfer matrix representing the optical system between the VCSEL and the MMF, our model also provides a strong tool for optimizing components in the practically produced multimode optical module, such as the focal length of a lens inserted between the VCSEL and the MMF. While a typical VCSEL was used in this work, with the Monte Carlo simulation, the statistical variations in the VCSEL parameters can be included in the model to investigate the variances in the performance obtained with various launch conditions.

Chapter 5

Analytical Expressions for Coupling Coefficients into GI Fibers

The closed-form analytical expressions of the power coupling coefficients are derived for a Laguerre-Gaussian beam coupled into a graded-index (GI) fiber with either central, offset, or tilted launch. The expressions are further generalized to an arbitrary launching condition with the radial offset and the three-dimension angular tilt simultaneously occurring. The analytical results are in good agreement with the numerical ones and can be applied to manufactured graded-index multimode fibers with an index exponent parameter from 1.8 to 2.2. Using the derived analytical expressions, the computation time shortens by at least a four-order of magnitude compared to conventional numerical methods. The work presented in this chapter has been published as a journal paper in IEEE Journal of Lightwave Technology [16].

5.1 Introduction

The Laguerre-Gaussian (LG)-beam modal decomposition attracts increased research interest due to its wide applications in optical communication, such as mode selective excitation [148, 149] and mode division multiplexing [87, 150]. Compared to step-index fiber, graded-index (GI) fiber has lower modal dispersion and lower mode mixing [151]. Therefore, the latter is an optimum choice for communications applications, while the former is more used in optical sensors [152] and fiber lasers [153]. Mode power distribution, which is strongly dependent on the launch conditions between the modes of the LG beam and fiber modes, play a determinative role for these applications [15]. A lot of works explored the optimum mode power distributions [15, 79, 81, 121, 154, 155]. Diverse launch techniques, such as an offset launch [79], mode-field matched center launch [155] and tilted launch [81] are proposed and developed.

The power coupling coefficients, a significant metric to quantify the mode power distribution, can be derived numerically by solving the overlap integral of two coupling modes [79]. Analytical solutions provide qualitative understanding of the coupling mechanisms and parametric dependencies. Additionally, the closed-form analytical expressions using a determined number of standard mathematical expressions avoid heavy numerical computations leading to significantly reduced computation time. Also, compared with numerical methods, it is more convenient to program analytical solutions in mathematical calculation software. In 2010, Amphawan, *et al.* in [119] proposed an analytical derivation of the power coupling coefficient for an offset launch of the fundamental Gaussian beam in a graded index MMF. In addition, an analytical expression is derived in [81] when a tilted Gaussian beam is coupled into the fiber. However, the analytical expressions in [81] and [119] only applies to the Gaussian beam, which can be regarded as a special case of the LG beam.

The LG beam shows more application potentials. For example, LG beams with different azimuthal indices provide access to optical orbital angular momentum multiplexing [156], and high-order LG beams also increase the transmission capacity through fiber spatial division multiplexing (SDM) techniques [157]. An analytical expression of the power coupling coefficient for the LG beam launch meets these applications. In addition, to better make use of the fiber channel, launch conditions are required to simultaneously include beam offset and tilts. The launch conditions in references [81, 119] consider only one alignment dimension at a time (the radial offset or the angular tilt) of the beam at the fiber input facet. Moreover, their launch positions are restricted to the beam waist plane not accounting for the beam propagation. Analytical expressions of coupling coefficients are proposed for an arbitrary launch condition when a LG beam is launched into the graded-index fiber.

Closed-form analytical expressions of power coupling coefficients are derived, when an LG beam is launched into a weakly-guided graded-index fiber employing a central launch, an offset launch, and a tilted launch. Then the expressions are generalized to an arbitrary launch condition. The rest of the chapter is organized as follows. Section 5.2 shows the theoretical basis for the analytical expressions of power coupling coefficients. The preliminary concepts of Laguerre-Gaussian modes, linearly polarized (LP) modes, launch conditions, and power coupling coefficients are introduced. In Section 5.3, for different launch conditions, their analytical expressions are derived. More specifically, in Section 5.3.1, the obtained analytical expression corresponds to the center launch; in Section 5.3.2 and 5.3.3, the analytical results are derived for the offset and tilted launch, respectively. In Section 5.3.4, a more generalized expression is presented under an arbitrary launch condition including both radial offset and angular tilt of the beam at the fiber facet. Section 5.4 compares the power coupling coefficients from the derived analytical expressions with those from the numerical finite difference method, validating analytical expressions. It is shown that the analytical expressions are applicable to manufactured MMF with profile parameters between 1.8 and 2.2. The computation times of both analytical and numerical methods are presented and compared. In Section 5.5, a summary is presented.

5.2 Theory Principles

5.2.1 Laguerre-Gaussian Beam Model

Surface emitting optical sources such as VCSELs generate optical beams that may be modeled as Laguerre-Gaussian (LG) modes [158], solutions to the complex paraxial Helmholtz partial differential equation in the cylindrical coordinate system (r,φ,z) [128]. The LG modes with the radial and azimuthal indices p and l, as expressed in (5.1), form a complete and orthogonal basis set, where i is the imaginary unit:

$$\begin{aligned}\mathrm{LG}_{p,l}\left(r,\varphi,z\right) &= \frac{C}{\omega_1}\cdot\left(\frac{\sqrt{2}r}{\omega_1}\right)^{|l|}\cdot\mathrm{L}_p^{|l|}\left(\frac{2r^2}{{\omega_1}^2}\right)\\ &\cdot\exp\left(-\frac{r^2}{{\omega_1}^2}-i(k\frac{r^2}{2R_1}+kz-\Phi)-il\varphi\right)\end{aligned} \tag{5.1}$$

where

$$C=\sqrt{\frac{2\cdot\Gamma\left(p+1\right)}{\pi\cdot\Gamma\left(p+\left|l\right|+1\right)}},$$

$$\Gamma\left(p+1\right)=p!\quad\left(p\in\mathbb{Z}\right).$$

The wavenumber k is the spatial frequency of the mode equals to $2\pi/\lambda$ where λ is the wavelength in the medium. $\mathrm{L}_p^{|l|}(\cdot)$ is the generalized Laguerre polynomial. For a given LG mode, ω_1 denotes the beam spot size at z, R_1 is the radius of curvature of the beam wavefront that intersects the beam axis at z, and Φ is the Gouy phase shift of the Laguere-Gaussian beam. The normalization constant C is derived by normalizing the intensity of the LG mode $\left|\mathrm{LG}_{p,l}\right|^2$ as in (5.2):

$$\int_0^{+\infty}\int_0^{2\pi}\left|\mathrm{LG}_{p,l}\right|^2 r dr d\varphi = 1. \tag{5.2}$$

For different azimuthal and radial indices, the mode spatial field distributions in the r-ϕ plane are shown in Fig. 5.1. The azimuthal index l represents the number of 2π phase changes along one closed circle around the optical axis. The radial index p describes the radial distribution of a given LG optical mode and represents the number of nulls radially. A Gaussian optical mode is a special case of the Laguerre-Gaussian optical modes where the values of the azimuthal and radial indices are equal to zero ($l{=}p{=}0$).

5.2.2 Electrical Field Distribution in Weakly-guided Fiber

The graded-index optical fiber, first invented by Jun-ichi Nishizawa [159], has a refractive index profile described by (5.3),

$$n(r)=\begin{cases} n_1\cdot\sqrt{1-2\cdot\Delta\cdot\left(\dfrac{r}{R}\right)^{\alpha}}\ , & 0\le r<R \\ \qquad n_2 \qquad\qquad\qquad , & R\le r\le R_C \end{cases} \tag{5.3}$$

where n_1 is the refractive index along the fiber axis, n_2 is the cladding refractive index, $\Delta{=}(n_1-n_2)/n_1$ is the profile height parameter, R is the MMF core radius, R_C is the cladding radius, and α is the index parameter. For commercially manufactured fiber, α

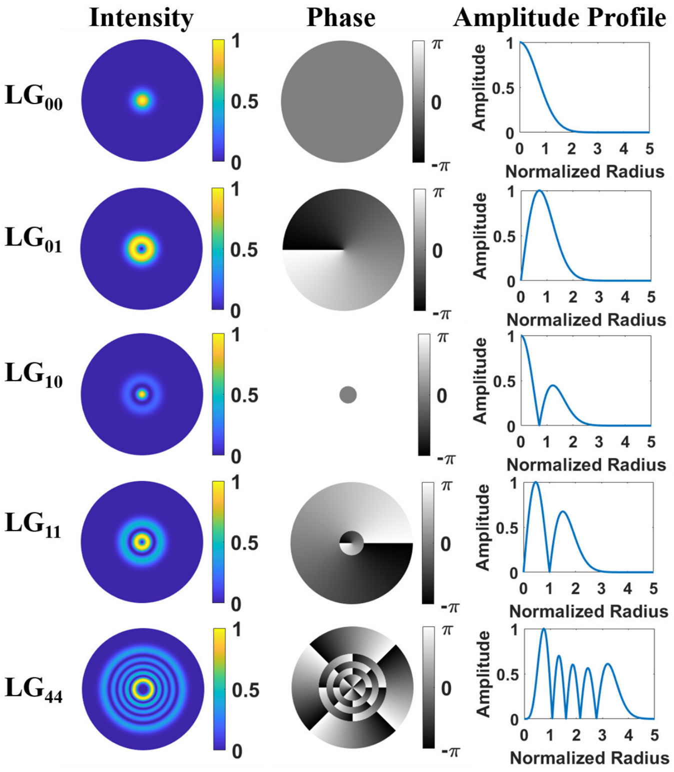

Fig. 5.1: Spatial distribution in the $r - \varphi$ plane of the Laguerre-Gaussian (LG) beams for different azimuthal and radial indices with their corresponding intensity, phase, and electrical field amplitude profile. For the amplitude profile, the x-axis is normalized to the beam spot size, and y-axis is normalized to the maximum field amplitude.

ranges approximately from 1.8 to 2.2 [119].

Under the weakly-guidance approximation, the transverse electrical field satisfies the following scalar wave equation,

$$\left(\nabla^2 + k^2 n(r)^2 - \beta^2\right) \cdot \Psi_{s,t} = 0 \tag{5.4}$$

where ∇^2 is the transverse Laplacian operator, β is the scalar propagation constant, and

$\Psi_{s,t}$ is the transverse electric field with the fiber mode azimuthal index s and radial index t. Equation (5.4) has no closed-form solutions for $\Psi_{s,t}$ with the exception of the infinite parabolic profile [127]. With the assumption of an infinite parabolic refractive index profile, a closed-form analytical solution for the fiber mode electrical field is obtained in (5.5). The analytical solution in (5.5) is a good approximation for the mode electric field in a commercially manufactured graded-index fiber with α ranging from 1.8 to 2.2 [160]. As examples, the electric field amplitude profiles of the LP_{01} even mode and the LP_{45} even mode for finite α-exponent and infinite parabolic refractive indices are shown in Fig. 5.2a and Fig. 5.2b, respectively. The electric fields for finite α-exponent refractive indices are in good agreement with those for the infinite parabolic profile both in Fig. 5.2a and Fig. 5.2b. To quantify the degree of agreement, the correlation coefficients of electric fields between finite α-exponent profiles and the infinite parabolic profile are calculated and illustrated in Fig. 5.2c. All values are larger than 0.995, validating our results.

$$\begin{aligned}\Psi_{s,t}^{\chi}\left(r,\varphi\right) = & B\cdot\left(\frac{r}{R}\right)^{s}\cdot \mathrm{L}_{t-1}^{s}\left(\frac{Vr^2}{R^2}\right)\cdot\exp\left(-\frac{Vr^2}{2R^2}\right)\\ & \cdot\begin{cases}\cos\left(s\varphi\right), & \text{when } \chi \text{ is } 'e'(\text{even})\\ \sin\left(s\varphi\right), & \text{when } \chi \text{ is } 'o'(\text{odd})\end{cases}\end{aligned} \tag{5.5}$$

$$B = \frac{1}{R}\sqrt{\frac{2V^{s+1}\cdot\Gamma(t)}{\left(1+\delta_{0,s}\right)\pi\cdot\Gamma(s+t)}} \tag{5.6}$$

V is the normalization frequency given by $V = 2\pi \mathrm{n}_1\sqrt{2\Delta}\mathrm{R}/\lambda$. The superscript χ is either $'e'$

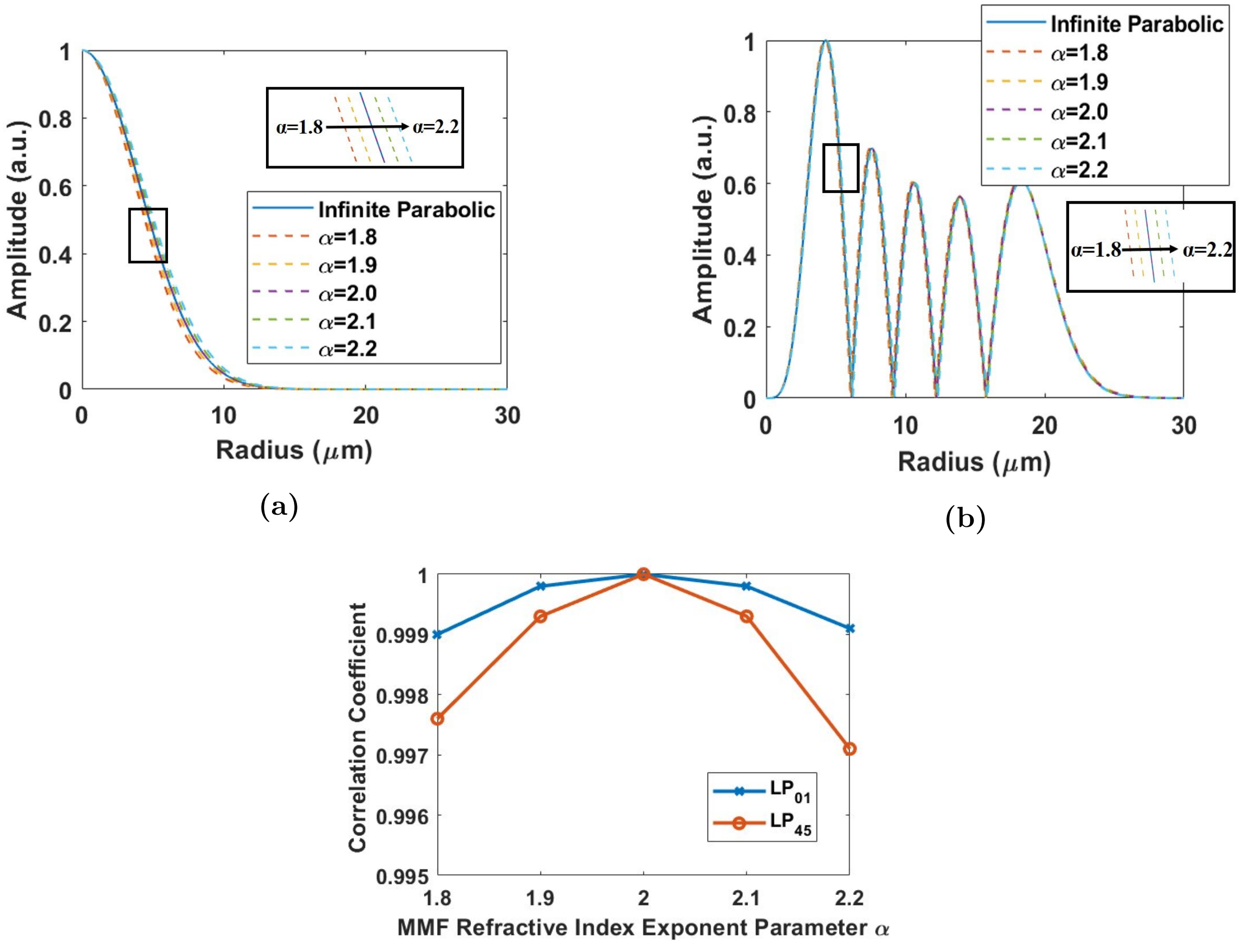

(a)

(b)

(c)

Fig. 5.2: (a) The electrical field amplitude of the LP_{01} even mode for the finite α-exponent refractive index profiles (dash curves) and the infinite parabolic refractive index profiles (solid curves). (b) The electrical field amplitude of the LP_{45} even mode for the finite α-exponent refractive index profiles (dash curves) and the infinite parabolic refractive index profiles (solid curves). (c) The correlation coefficients between the finite α-exponent refractive index profiles and the infinite parabolic refractive index profiles with α ranging from 1.8 to 2.2.

or $'o'$ denoting the even (cosine) or odd (sine) mode solution. B is a normalization constant described in (5.6), where δ is the Kronecker delta function. With this normalization constant, $\int_0^{+\infty}\int_0^{2\pi}\left|\Psi_{s,t}\right|^2 rdrd\varphi{=}1$ for all combinations of s and t, and the gamma function $\Gamma(\cdot)$ has the same definition as in (5.1). It is worth mentioning that the circular symmetric mode with $e^{is\varphi}$ is also a solution of the scalar wave equation, which is equivalent to $\Psi_{s,t}^{'e'}{+}i{\cdot}\Psi_{s,t}^{'o'}$. In the application of SDM, even and odd modes are widely used for transmission channels; therefore I prefer the even and odd modes rather than the circular modes.

5.2.3 Power Coupling Coefficient

The description of the beam launch condition into the fiber in three-dimension free space is shown in Fig. 5.3. The point **O** is the center of the fiber input facet, the point **P** is the center of the LG beam source, and the point **A** is the projection of **P** at the fiber input facet. The point **B** is the intersection point between the fiber input facet and the beam axis of the LG beam emitted from point **P**. The launch condition considers four parameters: the longitudinal distance $z_0{=}\overline{\mathbf{PA}}$, the radial offset $a_{off}{=}\overline{\mathbf{OB}}$, the incidence tilt angle $\psi{=}\angle\mathbf{APB}$, and the azimuthal tilt angle $\theta{=}\angle\mathbf{ABO}$. The positive x-axis of the fiber Cartesian coordinate system is defined to be along the direction of a_{off}, i.e., from the point **O** to the point **B**; thus, $a_{off}{\geq}0$. By combination of these parameters, the launch conditions cover the entire free space over the fiber input facet.

The calculation of the power coupling coefficient requires that the LG beam and fiber

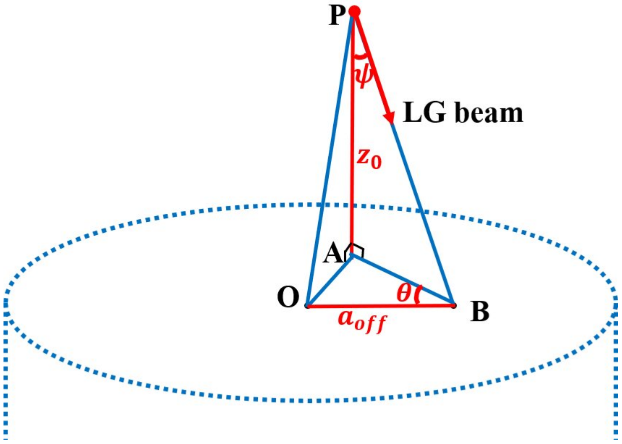

Fig. 5.3: Illustration of launch condition at the fiber surface (blue dash line). **P** is the center of the LG beam source; **A** is the projection of **P** on the fiber surface; **B** is the beam incident point; **O** is the center of the fiber input facet.

transverse electrical field be in the same coordinate system. The incidence tilt angle ψ is small in practical laser-fiber coupling structures to realize large coupling efficiencies. Based on this fact, the LG beam at the fiber input facet, $E_{p,l}$, is expressed in the fiber coordinate system as (5.7),

$$\mathrm{E}_{p,l}\left(r,\varphi\right)=\mathrm{LG}_{p,l}\left(\widetilde{r},\widetilde{\varphi},\tilde{z}\right) \tag{5.7}$$

where

$$\widetilde{r}^2=r^2+{a_{off}}^2-2a_{off}r\cos\varphi,$$

$$\widetilde{r}\cdot e^{i\widetilde{\varphi}}=e^{-i\theta}\cdot\left(r\cdot e^{i\varphi}-a_{off}\right),$$

$$\tilde{z}=r\sin\psi\cos\left(\varphi-\theta\right)-a_{off}\sin\psi\cos\theta+\frac{z_0}{\cos\psi}.$$

The field coupling coefficient, $c_{s,t,\chi}^{p,l}$, between the normalized Laguerre-Gaussian mode in

(5.7) and the normalized MMF mode in (5.5) is obtained using the overlap integral as follows:

$$c_{s,t,\chi}^{p,l} = \int_0^{+\infty} \int_0^{2\pi} \mathrm{E}_{p,l}(r,\varphi) \cdot \Psi_{s,t}^{\chi}(r,\varphi)^* r dr d\varphi. \tag{5.8}$$

The relation between the power coupling coefficient, $\eta_{s,t,\chi}^{p,l}$, and the field coupling coefficient, $c_{s,t,\chi}^{p,l}$, is expressed in (5.9):

$$\eta_{s,t,\chi}^{p,l} = \left| c_{s,t,\chi}^{p,l} \right|^2. \tag{5.9}$$

5.3 Analytical Coupling-coefficient Expressions

In this section, the closed-form analytical expressions of $c_{s,t,\chi}^{p,l}$ are obtained for the center launch (Section 5.3.1), the offset launch (Section 5.3.2), the tilted launch (Section 5.3.3), and the generalized launch (Section 5.3.4), respectively. The derivation steps follow the flow chart outlined in Fig. 5.4, where the overlap integral (5.8) is split into the φ-component integral part and the r-component integral part to reach the final solution.

5.3.1 Center Launch

For a central launch, the beam excites the fiber modes exactly at the center of the fiber input facet without any misalignment between the optical source and the fiber. In this case, a_{off}=0, ψ=0, and θ=0. The expression of the LG beam over the fiber input facet accounts

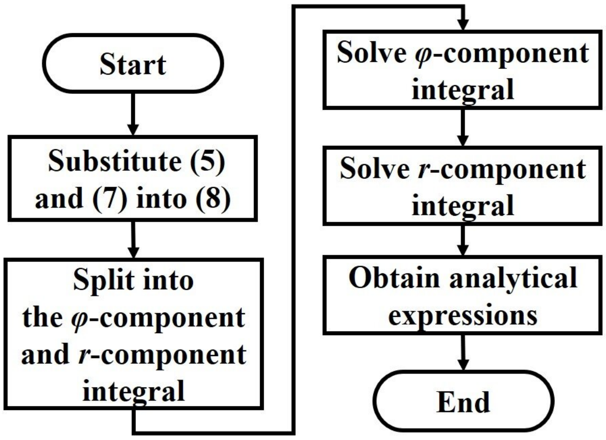

Fig. 5.4: The flow chart describing the derivation steps of the analytical expressions.

only for the longitudinal distance $z{=}z_0$. The coupling coefficient between the LG beam and the LP even (cosine) mode can be found using (5.8) with the φ-component integral part rewritten as:

$$\int_0^{2\pi} \exp\left(-il\varphi\right)\cos\left(s\varphi\right)d\varphi{=}\pi\cdot\left(1+\delta_{0,l}\right)\cdot\delta_{|l|,s}. \tag{5.10}$$

The delta function δ in (5.10) characterizes the orthogonality of the trigonometrical functions; thus, $|l|$ and s must have identical values to make the coupling coefficient non-zero for the central launch. Substituting the φ-component integral (5.10) into (5.8), the r-component integral is written by reordering the terms as follows:

$$\begin{aligned} c^{p,l}_{s,t,'e'}{=}&\pi\left(1+\delta_{0,l}\right)\delta_{|l|,s}e^{(i\Phi-ikz_0)}\frac{B\cdot C}{\omega_1}\left(\frac{\sqrt{2}}{\omega_1 R}\right)^{|l|}\\ &\cdot\int_0^{+\infty}\left\{r^{2|l|+1}\cdot\mathrm{L}_p^{|l|}\left(\frac{2r^2}{{\omega_1}^2}\right)\cdot\mathrm{L}_{t-1}^{|l|}\left(\frac{Vr^2}{R^2}\right)\right.\\ &\left.\cdot\exp\left(-\frac{r^2}{{\omega_1}^2}-\frac{Vr^2}{2R^2}-ik\frac{r^2}{2R_1}\right)\right\}dr. \end{aligned} \tag{5.11}$$

Letting $\nu = \dfrac{2}{{\omega_1}^2}$, $\mu = \dfrac{V}{R^2}$, $b = \dfrac{\nu+\mu}{2} + i\dfrac{k}{2R_1}$, $x = r^2$, and using the integral formula in [[141], Equation 7.414-4], the integral term may be rewritten as

$$\frac{1}{2}\int_0^{+\infty} x^{|l|}\cdot \mathrm{L}_p^{|l|}(\nu x)\cdot \mathrm{L}_{t-1}^{|l|}(\mu x)\cdot \exp(-bx)\,dx,$$

for which the solution is

$$\begin{aligned}&\frac{1}{2}\cdot\frac{\Gamma(p+t+|l|)}{\Gamma(p{+}1)\,\Gamma(t)}\cdot\frac{(b-\nu)^p(b-u)^{t-1}}{b^{p+t+|l|}}\\ &\quad\cdot\ {}_2\mathrm{F}_1\left(-t{+}1,{-}p;{-}p{-}t{-}\,|l|\,{+}1;\frac{b(b{-}\nu{-}\mu)}{(b{-}\nu)\,(b{-}\mu)}\right)\end{aligned} \tag{5.12}$$

where ${}_2\mathrm{F}_1(\cdot)$ is the Gaussian hypergeometric function. Since $t{-}1{\geq}0$, this Gaussian hypergeometric function term has a closed-form expression (5.13) called Jacobi polynomials of degree $t{-}1$ [161].

$$\begin{aligned}\sum_{k=0}^{t-1}\Bigg\{&(-1)^k\binom{t-1}{k}\frac{\Gamma(p+1)}{\Gamma(p-k+1)}\\ &\cdot\frac{\Gamma(p+t+|l|-k)}{\Gamma(p+t+|l|)}\left[\frac{b(b-\nu-\mu)}{(b-\nu)\,(b-\mu)}\right]^k\Bigg\}\end{aligned} \tag{5.13}$$

The field coupling coefficient between the LG beam and the fiber LP even mode can thus be rewritten from (5.11) as the following:

$$\begin{aligned}
c_{s,t,'e'}^{p,l} &= e^{i\Phi-ikz_0}\cdot\left(\sqrt{2}\right)^{|l|-2}\pi\left(1+\delta_{0,l}\right)\delta_{|l|,s}\\
&\cdot\frac{B\cdot C}{{\omega_1}^{|l|+1}R^{|l|}}\cdot\frac{(b-\nu)^p(b-\mu)^{t-1}}{b^{p+t+|l|}}\cdot\sum\nolimits_{k=0}^{t-1}\left\{(-1)^k\right.\\
&\left.\cdot\frac{\Gamma\left(p+t+|l|-k\right)}{\Gamma\left(k+1\right)\Gamma\left(t-k\right)\Gamma\left(p-k+1\right)}\left[\frac{b\left(b-\nu-\mu\right)}{\left(b-\nu\right)\left(b-\mu\right)}\right]^k\right\}.
\end{aligned}\tag{5.14}$$

For the field coupling coefficient between the LG beam and the fiber LP odd (sine) mode, its φ-component integral part is slightly different from (5.10), which is expressed as follows:

$$\int_0^{2\pi}\exp\left(-il\varphi\right)\sin\left(s\varphi\right)d\varphi=\mathrm{sgn}(l)\cdot -i\pi\left(1-\delta_{0,\mathrm{l}}\right)\delta_{|l|,s}\tag{5.15}$$

where sgn(·) is the sign function. Following the same mathematical derivation, the closed-form analytical expression for the fiber LP odd mode is written as (5.16):

$$\begin{aligned}
c_{s,t,'o'}^{p,l} &= e^{i\Phi-ikz_0-i\frac{\pi}{2}}\cdot\left(\sqrt{2}\right)^{|l|-2}\pi\left(1-\delta_{0,l}\right)\delta_{|l|,s}\\
&\cdot\mathrm{sgn}\left(l\right)\cdot\frac{B\cdot C}{{\omega_1}^{|l|+1}R^{|l|}}\cdot\frac{(b-\nu)^p(b-\mu)^{t-1}}{b^{p+t+|l|}}\cdot\sum\nolimits_{k=0}^{t-1}\left\{(-1)^k\right.\\
&\left.\cdot\frac{\Gamma\left(p+t+|l|-k\right)}{\Gamma\left(k+1\right)\Gamma\left(t-k\right)\Gamma\left(p-k+1\right)}\left[\frac{b\left(b-\nu-\mu\right)}{\left(b-\nu\right)\left(b-\mu\right)}\right]^k\right\}.
\end{aligned}\tag{5.16}$$

The expressions (5.14) and (5.16) for the LP even and odd modes have a difference in phase revealing that even and odd LP modes can act as separate sub-channels in MMF SDM transmission.

5.3.2 Offset Launch

In the case of an offset launch, the beam reaches the fiber facet with a radial offset a_{off} at the fiber input surface while the tilt angles, ψ and θ, are zero. Based on the relation (5.7), the expression of the LG beam at the fiber input facet for the offset launch is

$$\begin{aligned}\mathrm{E}_{p,l}\left(r,\varphi\right)=&\frac{C}{\omega_1}\left(\frac{\sqrt{2}}{\omega_1}\right)^{|l|}\left[r\cdot e^{-i\varphi\cdot\mathrm{sgn}(l)}-a_{off}\right]^{|l|}\\ &\cdot\exp\left[\left(-\frac{1}{{\omega_1}^2}-i\frac{k}{2R_1}\right)\left(r^2+{a_{off}}^2-2ra_{off}\cos\varphi\right)\right]\\ &\cdot\mathrm{L}_p^{|l|}\left[\frac{2\left(r^2+{a_{off}}^2-2ra_{off}\cos\varphi\right)}{{\omega_1}^2}\right]\cdot\exp\left(i\Phi-ikz_0\right).\end{aligned} \tag{5.17}$$

The following binomial formula (5.18) and the generalized Laguerre polynomial expansion (5.19) are used for deriving the analytical expressions:

$$(a+b)^n=\sum_{k=0}^{n}\binom{n}{k}a^k b^{n-k},\quad n=0,1,2\cdots, \tag{5.18}$$

$$\mathrm{L}_p^{|l|}\left(x\right)=\sum_{k=0}^{p}\left(-1\right)^k\binom{p+|l|}{p-k}\frac{x^k}{k!}. \tag{5.19}$$

As a result, (5.17) is transformed into (5.20). By using (5.18) and (5.19), (5.17) is simplified into a form of polynomial expression, which paves the way towards the analytical solution of the coupling coefficients.

$$
\begin{aligned}
\mathrm{E}_{p,l}\left(r,\varphi\right) ={}& \frac{C}{\omega_1}\cdot\left(\frac{\sqrt{2}}{\omega_1}\right)^{|l|}\cdot\exp\left(i\Phi-ikz_0\right)\\
&\cdot\sum\nolimits_{j_1=0}^{|l|}\left\{\binom{|l|}{j_1}\left[r\cdot e^{-i\varphi\cdot\mathrm{sgn}(l)}\right]^{j_1}\left(-a_{off}\right)^{|l|-j_1}\right\}\\
&\cdot\exp\left[\left(-\frac{1}{{\omega_1}^2}-i\frac{k}{2R_1}\right)\left(r^2+{a_{off}}^2-2ra_{off}\cos\varphi\right)\right]\\
&\cdot\sum\nolimits_{j_2=0}^{p}\sum\nolimits_{j_3=0}^{j_2}\left[\binom{j_2}{j_3}\binom{p+|l|}{p-j_2}\frac{(-2)^{j_2}}{j_2!{\omega_1}^{2j_2}}\right.\\
&\qquad\left.\cdot\left(r^2+{a_{off}}^2\right)^{j_2-j_3}\left(-2ra_{off}\cos\varphi\right)^{j_3}\right]
\end{aligned}
\tag{5.20}
$$

Substituting the expressions (5.5) and (5.20) into (5.8), the coupling coefficient for the fiber LP even mode is expressed below as (5.21) after some mathematical manipulations, which includes a φ-component integral part and a r-component integral part:

$$
\begin{aligned}
c_{s,t,'e'}^{p,l} ={}& \frac{\left(\sqrt{2}\right)^{|l|}B\cdot C}{{\omega_1}^{|l|+1}\cdot R^s}\cdot\exp\left(i\Phi-ikz_0\right)\\
&\cdot\exp\left[\left(-\frac{1}{{\omega_1}^2}-i\frac{k}{2R_1}\right){a_{off}}^2\right]\\
&\cdot\sum\nolimits_{j_1=0}^{|l|}\sum\nolimits_{j_2=0}^{p}\sum\nolimits_{j_3=0}^{j_2}\\
&\left\{\binom{|l|}{j_1}\binom{p+|l|}{p-j_2}\binom{j_2}{j_3}\frac{(-2)^{j_2}2^{j_3}}{j_2!{\omega_1}^{2j_2}}\left(-a_{off}\right)^{|l|-j_1+j_3}\right.\\
&\cdot\int_0^{+\infty}r^{j_1+j_3+s+1}\cdot\left(r^2+{a_{off}}^2\right)^{j_2-j_3}\cdot\mathrm{L}_{t-1}^{s}\left(\frac{Vr^2}{R^2}\right)\\
&\qquad\cdot\exp\left(-\alpha r^2\right)dr\\
&\cdot\int_0^{2\pi}\exp\left[-i\cdot j_1\cdot\mathrm{sgn}\left(l\right)\cdot\varphi\right]\cdot\left(\cos\varphi\right)^{j_3}\cdot\cos\left(s\varphi\right)\\
&\qquad\left.\cdot\exp\left[i\cdot b\cdot r\cdot\cos\left(\varphi\right)\right]d\varphi\right\}
\end{aligned}
\tag{5.21}
$$

where

$$\alpha = \frac{1}{{\omega_1}^2} + \frac{V}{2R^2} + i\frac{k}{2R_1},$$

$$b = \left(-\frac{2}{{\omega_1}^2}i + \frac{k}{R_1}\right) a_{off}.$$

Noticeably, the φ-component and r-component integral need to be transformed into the analytical expressions. Before calculating the φ-component integral part of (5.21), a useful equation (5.22) is obtained, based on the trigonometric product-to-sum formula and power-reduction formula:

$$(\cos\varphi)^m \cos(q\varphi) = \frac{1}{2^m} \sum\nolimits_{k=0}^{m} \binom{m}{k} \cos\left[(q+2k-m)\varphi\right]. \tag{5.22}$$

Using trigonometric transformation formulas, the φ-component integral part in (5.21), denoted as f_1, is simplified as (5.23):

$$\begin{aligned} f_1 = \frac{1}{2^{j_3+1}} \sum\nolimits_{j_4=0}^{j_3} \binom{j_3}{j_4} \cdot \int_0^{2\pi} & \exp\left[i \cdot b \cdot r \cdot \cos(\varphi)\right] \\ & \cdot \Big\{ \cos\Big[(j_1 \cdot \mathrm{sgn}(l) - s + 2j_4 - j_3)\,\varphi \Big] \\ & + \cos\Big[(j_1 \cdot \mathrm{sgn}(l) + s + 2j_4 - j_3)\,\varphi \Big] \Big\}\, d\varphi. \end{aligned} \tag{5.23}$$

Equation (5.23) is observed as an integral representation of the Bessel function. The

Bessel function of the first kind, $J_l(z)$, is given by (5.24) [141]:

$$\frac{1}{2\pi}\int_0^{2\pi} \exp\left[i\cdot x\cdot \cos\left(\varphi\right)\right]\cos(l\varphi)d\varphi = i^{|l|}J_{|l|}\left(x\right). \tag{5.24}$$

With (5.24), the φ-component integral is solved, and f_1 is transformed into the Bessel-function expression:

$$f_1 = \frac{\pi}{2^{j_3}}\cdot \sum\nolimits_{j_4=0}^{j_3}\binom{j_3}{j_4}\cdot\left[i^{\gamma_1}J_{\gamma_1}\left(br\right) + i^{\gamma_2}J_{\gamma_2}\left(br\right)\right] \tag{5.25}$$

where

$$\gamma_1 = \left|j_1\cdot\mathrm{sgn}\left(l\right) - s + 2j_4 - j_3\right|,$$

$$\gamma_2 = \left|j_1\cdot\mathrm{sgn}\left(l\right) + s + 2j_4 - j_3\right|.$$

The two terms with γ_1 and γ_2 in (5.25) correspond to the circular symmetric LP modes with the phase terms $e^{-is\varphi}$ and $e^{is\varphi}$, another complete set of solutions of the fiber scalar wave equation (5.4). The r-component integral part, represented by f_2, can be transformed into (5.26) using the binomial formula (5.18) and the polynomial expansion (5.19):

$$\begin{aligned} f_2 = & \sum\nolimits_{j_5=0}^{j_2-j_3}\binom{j_2-j_3}{j_5}\left(a_{off}\right)^{2j_2-2j_3-2j_5} \\ & \cdot\sum\nolimits_{j_6=0}^{t-1}\left\{\binom{t-1+s}{t-1-j_6}\cdot\frac{1}{j_6!}\cdot\frac{\left(-V\right)^{j_6}}{R^{2j_6}}\right. \\ & \left.\cdot\int_0^{+\infty}\exp\left(-\alpha r^2\right)\cdot r^{\mu}\cdot\left[i^{\gamma_1}J_{\gamma_1}\left(br\right) + i^{\gamma_2}J_{\gamma_2}\left(br\right)\right]dr\right\} \end{aligned} \tag{5.26}$$

where

$$\mu = j_1 + j_3 + s + 1 + 2j_5 + 2j_6.$$

According to the following integral formula (5.27) [22, Equation 6.631],

$$\begin{aligned}
&\textstyle\int_0^{+\infty} x^{\mu} \exp\left(-\alpha x^2\right) J_\nu\left(bx\right) dx \\
&= \frac{b^\nu \alpha^{-\frac{\nu+\mu+1}{2}}}{2^{\nu+1}\Gamma\left(\nu+1\right)} \cdot \Gamma\left(\frac{\nu+\mu+1}{2}\right) \\
&\quad \cdot {}_1\mathrm{F}_1\left(\frac{\nu+\mu+1}{2}; \nu+1; -\frac{b^2}{4\alpha}\right)
\end{aligned} \tag{5.27}$$

the integral f_2 is rewritten below with the last term modified where ${}_1\mathrm{F}_1$ is the confluent hypergeometric function. q could be 1 or 2, corresponding to the two added terms in (5.23) after the trigonometric product-to-sum operation, respectively.

$$\begin{aligned}
f_2 = &\textstyle\sum_{j_5=0}^{j_2-j_3} \binom{j_2-j_3}{j_5} \left(a_{off}\right)^{2j_2-2j_3-2j_5} \\
&\cdot \textstyle\sum_{j_6=0}^{t-1} \Bigg\{ \binom{t-1+s}{t-1-j_6} \frac{1}{j_6!} \frac{(-V)^{j_6}}{R^{2j_6}} \\
&\cdot \textstyle\sum_{q=1}^{2} \Bigg[\frac{\alpha^{-\frac{\gamma_q+\mu+1}{2}} i^{\gamma_q} b^{\gamma_q}}{2^{\gamma_q+1}\Gamma\left(\gamma_q+1\right)} \cdot \Gamma\left(\frac{\gamma_\mathrm{q}+\mu+1}{2}\right) \\
&\qquad \cdot {}_1\mathrm{F}_1\left(\frac{\gamma_q+\mu+1}{2}; \gamma_q+1; -\frac{b^2}{4\alpha}\right) \Bigg] \Bigg\}
\end{aligned} \tag{5.28}$$

The field coupling coefficient between the LG beam and the fiber LP even mode for the offset launch defined in (5.21) is expressed with the integral parts of the φ-component and the r-component rewritten, as summarized below in (5.29):

$$
\begin{aligned}
c_{s,t,'e'}^{p,l} &= \exp\left(i\Phi - ikz_0\right) \\
&\cdot \frac{\left(\sqrt{2}\right)^{|l|} \pi \cdot B \cdot C}{{\omega_1}^{|l|+1} \cdot R^s} \exp\left[\left(-\frac{1}{{\omega_1}^2} - i\frac{k}{2R_1}\right) {a_{off}}^2\right] \\
&\cdot \sum_{j_1=0}^{|l|} \sum_{j_2=0}^{p} \sum_{j_3=0}^{j_2} \sum_{j_4=0}^{j_3} \sum_{j_5=0}^{j_2-j_3} \sum_{j_6=0}^{t-1} \\
&\Bigg\{ \binom{|l|}{j_1} \binom{p+|l|}{p-j_2} \binom{j_2}{j_3} \binom{j_3}{j_4} \binom{j_2-j_3}{j_5} \binom{t-1+s}{t-1-j_6} \\
&\cdot \frac{(-2)^{j_2}}{j_2! {\omega_1}^{2j_2}} \frac{1}{j_6!} \left(-\frac{V}{R^2}\right)^{j_6} \left(-a_{off}\right)^{|l|-j_1+2j_2-j_3-2j_5} \\
&\cdot \sum_{q=1}^{2} \left[\frac{\alpha^{-\frac{\gamma_q+\mu+1}{2}} i^{\gamma_q} b^{\gamma_q}}{2^{\gamma_q+1} \Gamma\left(\gamma_q+1\right)} \cdot \Gamma\left(\frac{\gamma_q+\mu+1}{2}\right) \right. \\
&\qquad \left. \cdot {}_1\mathrm{F}_1\left(\frac{\gamma_q+\mu+1}{2}; \gamma_q+1; -\frac{b^2}{4\alpha}\right) \right] \Bigg\}.
\end{aligned}
\tag{5.29}
$$

It is worth noting that ${}_1\mathrm{F}_1$ is a non-elementary function in principle, but the term ${}_1\mathrm{F}_1$ in (5.29) can be given by a closed-form analytical expression (see Appendix A).

Concerning the coupling coefficient for the LP odd mode, the whole derivation is almost identical to that for the even mode, so its expression is directly given in (5.30):

$$\begin{aligned}
c^{p,l}_{s,t,'o'} &= \exp\left(i\Phi - ikz_0 + i\tfrac{\pi}{2}\right) \\
&\cdot\frac{\left(\sqrt{2}\right)^{|l|}\pi\cdot B\cdot C}{{\omega_1}^{|l|+1}\cdot R^s}\exp\left[\left(-\frac{1}{{\omega_1}^2} - i\frac{k}{2R_1}\right){a_{off}}^2\right] \\
&\cdot\sum\nolimits_{j_1=0}^{|l|}\sum\nolimits_{j_2=0}^{p}\sum\nolimits_{j_3=0}^{j_2}\sum\nolimits_{j_4=0}^{j_3}\sum\nolimits_{j_5=0}^{j_2-j_3}\sum\nolimits_{j_6=0}^{t-1} \\
&\left\{\binom{|l|}{j_1}\binom{p+|l|}{p-j_2}\binom{j_2}{j_3}\binom{j_3}{j_4}\binom{j_2-j_3}{j_5}\binom{t-1+s}{t-1-j_6}\right. \\
&\cdot\frac{(-2)^{j_2}}{j_2!{\omega_1}^{2j_2}}\frac{1}{j_6!}\left(-\frac{V}{R^2}\right)^{j_6}\left(-a_{off}\right)^{|l|-j_1+2j_2-j_3-2j_5} \\
&\cdot\sum\nolimits_{q=1}^{2}\left[\frac{\alpha^{-\frac{\gamma_q+\mu+1}{2}}(-1)^q i^{\gamma_q} b^{\gamma_q}}{2^{\gamma_q+1}\Gamma\left(\gamma_q+1\right)}\cdot\Gamma\left(\frac{\gamma_q+\mu+1}{2}\right)\right. \\
&\qquad\left.\left.\cdot{}_1\mathrm{F}_1\left(\frac{\gamma_q+\mu+1}{2};\gamma_q+1;-\frac{b^2}{4\alpha}\right)\right]\right\}.
\end{aligned} \tag{5.30}$$

5.3.3 Tilted Launch

For the tilted launch, the beam reaches the fiber input facet with a small tilt angle ψ. The x-axis direction in the fiber coordinate system is defined to coincide with the line AB in Fig. 5.3 when a_{off} is zero. In such case, the expression of the LG beam over the fiber input facet is described as

$$\begin{aligned}
\mathrm{E}_{p,l}\left(r,\varphi\right) &= \frac{C}{\omega_1}\cdot\left(\frac{\sqrt{2}r}{\omega_1}\right)^{|l|}\cdot\mathrm{L}_p^{|l|}\left(\frac{2r^2}{{\omega_1}^2}\right) \\
&\cdot\exp\left(-\frac{r^2}{{\omega_1}^2}-i(k\frac{r^2}{2R_1}+k\frac{z_0}{\cos\psi}-\Phi)-il\varphi\right) \\
&\cdot\exp\left(-ikr\sin\psi\cos\varphi\right).
\end{aligned} \tag{5.31}$$

Substituting (5.5) and (5.31) into (5.8), the coupling coefficient for the fiber LP even mode is expressed in (5.32):

$$\begin{aligned} c^{p,l}_{s,t,'e'} = & \int_0^{+\infty} \frac{C}{\omega_1} \cdot \left(\frac{\sqrt{2} r}{\omega_1} \right)^{|l|} \cdot \mathrm{L}_p^{|l|} \left(\frac{2r^2}{{\omega_1}^2} \right) \\ & \cdot \exp \left(-\frac{r^2}{{\omega_1}^2} - i (k \frac{r^2}{2R_1} + k \frac{z_0}{\cos\psi} - \Phi) \right) \\ & \cdot B \cdot \left(\frac{r}{R} \right)^s \cdot \mathrm{L}_{t-1}^s \left(\frac{V r^2}{R^2} \right) \cdot \exp \left(-\frac{V r^2}{2R^2} \right) \cdot r dr \\ & \cdot \int_0^{2\pi} \exp \left(-il\varphi - ikr \sin\psi \cos\varphi \right) \cdot \cos \left(s\varphi \right) d\varphi \ . \end{aligned} \tag{5.32}$$

Using the relation (5.24) for the Bessel function, the φ-component integral part, denoted as f_1, is simplified in its expression (5.33).

$$f_1 = (-i)^{|s-l|} \pi J_{|s-l|} \left(k \cdot \sin\psi \cdot r \right) + (-i)^{|s+l|} \pi J_{|s+l|} \left(k \cdot \sin\psi \cdot r \right) \tag{5.33}$$

With the φ-component integral rewritten, (5.32) is reorganized into the following expression (5.34) with (5.33):

$$\begin{aligned} c^{p,l}_{s,t,'e'} = & \exp \left(i\Phi - ik \frac{z_0}{\cos\psi} \right) \frac{\pi \cdot B \cdot C}{\omega_1} \left(\frac{\sqrt{2}}{\omega_1} \right)^{|l|} \left(\frac{1}{R} \right)^s \\ & \cdot \int_0^{+\infty} r^{|l|+s+1} \cdot \mathrm{L}_p^{|l|} \left(\frac{2r^2}{{\omega_1}^2} \right) \cdot \mathrm{L}_{t-1}^s \left(\frac{V \cdot r^2}{R^2} \right) \\ & \cdot \exp \left(-\frac{r^2}{{\omega_1}^2} - \frac{V}{2R^2} r^2 - i \frac{k}{2R_1} r^2 \right) \\ & \cdot \Big[(-i)^{|s-l|} J_{|s-l|} \left(k \cdot \sin\psi \cdot r \right) \\ & \quad + (-i)^{|s+l|} J_{|s+l|} \left(k \cdot \sin\psi \cdot r \right) \Big] \ dr. \end{aligned} \tag{5.34}$$

Expanding the Laguerre polynomials using the series (5.35),

$$\begin{aligned}&\mathrm{L}_p^{|l|}\left(\frac{2r^2}{{\omega_1}^2}\right)\cdot\mathrm{L}_{t-1}^{s}\left(\frac{Vr^2}{R^2}\right)\\&=\sum\nolimits_{j_1=0}^{p}\sum\nolimits_{j_2=0}^{t-1}\left[\binom{p+|l|}{p-j_1}\binom{t-1+s}{t-1-j_2}\right.\\&\qquad\left.\cdot\frac{1}{j_1!j_2!}\left(-\frac{2r^2}{{\omega_1}^2}\right)^{j_1}\left(-\frac{Vr^2}{R^2}\right)^{j_2}\right]\end{aligned}\tag{5.35}$$

and using the relation (5.27), the r-component integral is solved. The coupling coefficient into the fiber LP even mode for the tilted launch is presented in (5.36):

$$\begin{aligned}c_{s,t,'e'}^{p,l}=&\exp\left(i\Phi-ik\frac{z_0}{\cos\psi}\right)\frac{\pi\cdot B\cdot C}{\omega_1}\left(\frac{\sqrt{2}}{\omega_1}\right)^{|l|}\left(\frac{1}{R}\right)^{s}\\&\cdot\sum\nolimits_{j_1=0}^{p}\sum\nolimits_{j_2=0}^{t-1}\left\{\binom{p+|l|}{p-j_1}\binom{t-1+s}{t-1-j_2}\right.\\&\cdot\frac{1}{j_1!j_2!}\left(-\frac{2}{{\omega_1}^2}\right)^{j_1}\left(-\frac{V}{R^2}\right)^{j_2}\\&\cdot\sum\nolimits_{q=1}^{2}\left[\frac{\alpha^{-\frac{\gamma_q+\mu+1}{2}}\left(-i\right)^{\gamma_q}b^{\gamma_q}}{2^{\gamma_q+1}\Gamma\left(\gamma_q+1\right)}\cdot\Gamma\left(\frac{\gamma_q+\mu+1}{2}\right)\right.\\&\qquad\left.\left.\cdot{}_1\mathrm{F}_1\left(\frac{\gamma_q+\mu+1}{2};\gamma_q+1;-\frac{b^2}{4\alpha}\right)\right]\right\}\end{aligned}\tag{5.36}$$

where

$$\alpha=\frac{1}{{\omega_1}^2}+\frac{V}{2R^2}+i\frac{k}{2R_1},$$

$$b=k\sin\psi,$$

$$\mu=|l|+s+1+2j_1+2j_2,$$

$$\gamma_1 = \left|s - l\right|,$$

$$\gamma_2 = \left|s + l\right|.$$

Likewise, the coupling coefficient into the fiber LP odd mode for the tilted launch is expressed in (5.37):

$$\begin{aligned} c_{s,t,'o'}^{p,l} = & \exp\left(i\Phi - ik\frac{z_0}{\cos\psi} + i\frac{\pi}{2}\right)\frac{\pi\cdot B\cdot C}{\omega_1}\left(\frac{\sqrt{2}}{\omega_1}\right)^{|l|}\left(\frac{1}{R}\right)^{s} \\ & \cdot\sum\nolimits_{j_1=0}^{p}\sum\nolimits_{j_2=0}^{t-1}\left\{\binom{p+|l|}{p-j_1}\binom{t-1+s}{t-1-j_2}\right. \\ & \cdot\frac{1}{j_1!j_2!}\left(-\frac{2}{{\omega_1}^2}\right)^{j_1}\left(-\frac{V}{R^2}\right)^{j_2} \\ & \cdot\sum\nolimits_{q=1}^{2}\left[\frac{\alpha^{-\frac{\gamma_q+\mu+1}{2}}(-1)^q(-i)^{\gamma_q}b^{\gamma_q}}{2^{\gamma_q+1}\Gamma\left(\gamma_q+1\right)}\cdot\Gamma\left(\frac{\gamma_q+\mu+1}{2}\right)\right. \\ & \left.\left.\cdot{}_1\mathrm{F}_1\left(\frac{\gamma_q+\mu+1}{2};\gamma_q+1;-\frac{b^2}{4\alpha}\right)\right]\right\}. \end{aligned} \tag{5.37}$$

Additionally, the analytical expression of the coupling coefficient for the circular symmetric mode can also be obtained from (5.36) and (5.37) using $\frac{1+\delta_{0,s}}{2}\cdot(c_{s,t,'e'}^{p,l} - i\cdot c_{s,t,'o'}^{p,l})$.

5.3.4 Generalized Launch

For a more generalized launch condition, as illustrated in Fig. 5.3, the beam arrives at the fiber input surface with misalignment values a_{off}, ψ, and θ. In fact, the offset launch derived in Section 5.3.2 and the tilted launch derived in Section 5.3.3 can be seen as two special cases. Under the generalized launch, the expression of the LG beam over the fiber input facet is expressed in (5.38) using the fiber cylindrical coordinate system:

$$\begin{aligned}
\mathrm{E}_{p,l}=&\frac{C}{\omega_1}\left(\frac{\sqrt{2}}{\omega_1}\right)^{|l|}\left[e^{i\theta\mathrm{sgn}(l)}\left(r\cdot e^{-i\varphi\cdot\mathrm{sgn}(l)}-a_{off}\right)\right]^{|l|}\\
&\cdot\exp\left[\left(-\frac{1}{{\omega_1}^2}-i\frac{k}{2R_1}\right)\left(r^2+{a_{off}}^2-2ra_{off}\cos\varphi\right)\right]\\
&\cdot\mathrm{L}_p^{|l|}\left[\frac{2\left(r^2+{a_{off}}^2-2ra_{off}\cos\varphi\right)}{{\omega_1}^2}\right]\\
&\cdot\exp\left[-ik\sin\psi r\cos\left(\varphi-\theta\right)+ika_{off}\sin\psi\cos\theta\right]\\
&\cdot\exp\left(i\cdot\Phi-ik\frac{z_0}{\cos\psi}\right).
\end{aligned}\tag{5.38}$$

Applying the binomial formula (5.18) and the Laguerre polynomial expansion (5.19), the expression (5.38) is rewritten as follows:

$$\begin{aligned}
\mathrm{E}_{p,l}=&\frac{C}{\omega_1}\cdot\left(\frac{\sqrt{2}}{\omega_1}\right)^{|l|}\cdot\exp\left(i\cdot\Phi-ik\frac{z_0}{\cos\psi}\right)\cdot e^{i\cdot\theta\cdot l}\\
&\cdot\exp\left[-ik\sin\psi r\cos\left(\varphi-\theta\right)+ika_{off}\sin\psi\cos\theta\right]\\
&\cdot\exp\left[\left(-\frac{1}{{\omega_1}^2}-i\frac{k}{2R_1}\right)\left(r^2+{a_{off}}^2-2ra_{off}\cos\varphi\right)\right]\\
&\cdot\sum\nolimits_{j_1=0}^{|l|}\left\{\binom{|l|}{j_1}\left[r\cdot e^{-i\varphi\cdot\mathrm{sgn}(l)}\right]^{j_1}\left(-a_{off}\right)^{|l|-j_1}\right\}\\
&\cdot\sum\nolimits_{j_2=0}^{p}\left\{\binom{p+|l|}{p-j_2}\frac{(-2)^{j_2}}{j_2!{\omega_1}^{2j_2}}\cdot\sum\nolimits_{j_3=0}^{j_2}\left[\binom{j_2}{j_3}\right.\right.\\
&\qquad\left.\left.\cdot\left(r^2+{a_{off}}^2\right)^{j_2-j_3}\left(-2ra_{off}\cos\varphi\right)^{j_3}\right]\right\}.
\end{aligned}\tag{5.39}$$

Therefore, the coupling coefficient (5.8) for the fiber LP even mode is expressed in (5.40) after mathematical operations, divided into two parts: the φ-component and r-component integral.

$$
\begin{aligned}
c^{p,l}_{s,t,'e'} = & \frac{\left(\sqrt{2}\right)^{|l|} B \cdot C}{{\omega_1}^{|l|+1} \cdot R^s} \cdot e^{i \cdot \theta \cdot l} \cdot \exp\left(i\Phi - ik\frac{z_0}{\cos\psi}\right) \\
& \cdot \exp\left[\left(-\frac{1}{{\omega_1}^2} - i\frac{k}{2R_1}\right){a_{off}}^2 + ika_{off}\sin\psi\cos\theta\right] \\
& \cdot \sum\nolimits_{j_1=0}^{|l|} \sum\nolimits_{j_2=0}^{p} \sum\nolimits_{j_3=0}^{j_2} \\
& \left\{ \binom{|l|}{j_1} \binom{p+|l|}{p-j_2} \binom{j_2}{j_3} \frac{(-2)^{j_2} 2^{j_3}}{j_2! {\omega_1}^{2j_2}} \left(-a_{off}\right)^{|l|-j_1+j_3} \right. \\
& \cdot \int_0^{+\infty} r^{j_1+j_3+s+1} \left(r^2 + {a_{off}}^2\right)^{j_2-j_3} \mathrm{L}^s_{t-1}\left(\frac{V}{R^2} r^2\right) \\
& \qquad \cdot \exp\left[\left(-\frac{1}{{\omega_1}^2} - i\frac{k}{2R_1} - \frac{V}{2R^2}\right) r^2\right] dr \\
& \cdot \int_0^{2\pi} \exp\left[-i \cdot j_1 \mathrm{sgn}\left(l\right) \varphi\right] \left(\cos\varphi\right)^{j_3} \cos\left(s\varphi\right) \\
& \qquad \cdot \exp\left[-ik\sin\psi r\cos\left(\varphi - \theta\right)\right] \\
& \qquad \left. \cdot \exp\left[\left(\frac{2}{{\omega_1}^2} + i\frac{k}{R_1}\right) a_{off} r\cos\varphi\right] d\varphi \right\}
\end{aligned}
\tag{5.40}
$$

Both φ-component and r-component integrals need to be calculated. Letting

$$
\varepsilon = \frac{2a_{off}}{{\omega_1}^2} + i\left(\frac{k}{R_1} a_{off} - k\sin\psi\cos\theta\right)
$$

and $\zeta = k\sin\psi\sin\theta$, the φ-component integral in (5.40), denoted as f_1, is reorganized as

(5.41). The parameters ε and ζ characterize the beam misalignment at the fiber input facet.

$$\begin{aligned} f_1 =& \frac{1}{2^{j_3+1}} \sum\nolimits_{j_4=0}^{j_3} \binom{j_3}{j_4} \cdot \int_0^{2\pi} \exp\left(\varepsilon \cdot r \cdot \cos\varphi\right) \\ &\cdot \Big\{ \cos\Big[\left(j_1 \cdot \operatorname{sgn}(l) - s + 2j_4 - j_3\right)\varphi + \zeta \cdot r \cdot \sin\varphi\Big] \\ &+ \cos\Big[\left(j_1 \cdot \operatorname{sgn}(l) + s + 2j_4 - j_3\right)\varphi + \zeta \cdot r \cdot \sin\varphi\Big] \Big\}\, d\varphi \end{aligned} \tag{5.41}$$

A generalized Schläfli integral given by (5.42) [162] helps to solve the integral in (5.41), where the order of the Bessel function, ν, is an integer.

$$\begin{aligned} &\frac{1}{2\pi} \int_0^{2\pi} \exp\left[x \cdot \cos(\varphi)\right] \cos\left(y \cdot \sin\varphi - \nu\varphi\right) d\varphi \\ &= \frac{(y+x)^{\nu/2}}{(y-x)^{\nu/2}} J_\nu\left(\sqrt{y^2 - x^2}\right) \quad \left(\nu \in \mathbb{Z}, \operatorname{Re}(x+y) > 0\right) \end{aligned} \tag{5.42}$$

To facilitate the calculation, $a_{off}>0$ is assumed here. When $a_{off}=0$, the generalized launch degenerates to the tilted launch in Section 5.3.3, and power coupling coefficient can be obtained by (5.36) and (5.37). the most common convention is used that the principal value of the complex argument is located at $(-\pi, \pi]$. Noting that $\operatorname{Re}(\varepsilon)>0$ and $\cos(x)$ is an even function, for $\zeta \in \mathbb{R}$,

$$\begin{aligned} &\int_0^{2\pi} \exp\left[\varepsilon \cdot r \cdot \cos(\varphi)\right] \cos\left(\zeta \cdot r \cdot \sin\varphi - \nu \cdot \varphi\right) d\varphi \\ =& \int_0^{2\pi} \exp\left[\varepsilon \cdot r \cdot \cos(\varphi)\right] \cos\left(|\zeta| \cdot r \cdot \sin\varphi - u(\zeta) \cdot \nu \cdot \varphi\right) d\varphi \\ =& 2\pi \cdot \frac{\left(|\zeta| + \varepsilon\right)^{u(\zeta)\cdot\nu/2}}{\left(|\zeta| - \varepsilon\right)^{u(\zeta)\cdot\nu/2}} \cdot J_{u(\zeta)\cdot\nu}\left(\sqrt{\zeta^2 r^2 - \varepsilon^2 r^2}\right) \quad (\nu \in \mathbb{Z}) \end{aligned} \tag{5.43}$$

where

$$u(\zeta)=\begin{cases} 1, & \zeta \geq 0 \\ -1, & \zeta < 0 \end{cases}.$$

$u(\zeta)$, depending on ψ and θ, indicates how an incident LG beam tilts at the fiber input facet.

Therefore, (5.41) is evolved into (5.44) with the φ-component integral rewritten,

$$\begin{gathered} f_1 = \frac{\pi}{2^{j_3}} \sum\nolimits_{j_4=0}^{j_3} \binom{j_3}{j_4} \left[\sum\nolimits_{q=1}^{2} \frac{(|\zeta| - \varepsilon)^{\gamma_q/2}}{(|\zeta| + \varepsilon)^{\gamma_q/2}} \right. \\ \left. \cdot \left[-\operatorname{sgn}\left(\gamma_q\right) \right]^{\gamma_q} J_{|\gamma_q|} \left(\sqrt{\zeta^2 - \varepsilon^2} \cdot r \right) \right] \end{gathered} \tag{5.44}$$

where

$$\gamma_1 = [j_1 \cdot \operatorname{sgn}(l) - s + 2j_4 - j_3] \cdot u(\zeta),$$

and

$$\gamma_2 = [j_1 \cdot \operatorname{sgn}(l) + s + 2j_4 - j_3] \cdot u(\zeta).$$

The signs of s in γ_1 and γ_2 are opposite, implying the even mode can be formed by two circular modes with the opposite azimuthal indices. After substituting (5.44) back into

(5.40), the r-component of the integral is extracted from (5.40) as follows:

$$\begin{aligned} f_2 = & \int_0^{+\infty} r^{j_1+j_3+s+1} \left(r^2 + {a_{off}}^2\right)^{j_2-j_3} L_{t-1}^{s}\left(\frac{V}{R^2} r^2\right) \\ & \cdot e^{-\alpha r^2} J_{\left|\gamma_q\right|}\left(b \cdot r\right) dr \\ = & \sum\nolimits_{j_5=0}^{j_2-j_3} \binom{j_2-j_3}{j_5} \left(a_{off}\right)^{2j_2-2j_3-2j_5} \sum\nolimits_{j_6=0}^{t-1} \Bigg\{ \frac{1}{j_6!} \\ & \cdot \binom{t-1+s}{t-1-j_6} \frac{(-V)^{j_6}}{R^{2j_6}} \int_0^{+\infty} e^{-\alpha r^2} \cdot r^{\mu} \cdot J_{\left|\gamma_q\right|}\left(b \cdot r\right) dr \Bigg\} \end{aligned} \tag{5.45}$$

where

$$\alpha = \frac{1}{{\omega_1}^2} + \frac{V}{2R^2} + i \frac{k}{2R_1},$$

$$b = \sqrt{\zeta^2 - \varepsilon^2},$$

$$\mu = s + 1 + j_1 + j_3 + 2j_5 + 2j_6.$$

Using the integral formula (5.27), (5.45) is transformed into the analytical expression (5.46) with the r-component integral solved:

$$\begin{aligned} f_2 = & \sum\nolimits_{j_5=0}^{j_2-j_3} \binom{j_2-j_3}{j_5} \left(a_{off}\right)^{2j_2-2j_3-2j_5} \\ & \cdot \sum\nolimits_{j_6=0}^{t-1} \Bigg\{ \binom{t-1+s}{t-1-j_6} \frac{1}{j_6!} \frac{(-V)^{j_6}}{R^{2j_6}} \\ & \cdot \alpha^{-\frac{\left|\gamma_q\right|+\mu+1}{2}} \frac{b^{\left|\gamma_q\right|} \Gamma\left(\frac{\left|\gamma_q\right|+\mu+1}{2}\right)}{2^{\left|\gamma_q\right|+1} \Gamma\left(\left|\gamma_q\right|+1\right)} \\ & \cdot {}_1\mathrm{F}_1\left(\frac{\left|\gamma_q\right|+\mu+1}{2}; \left|\gamma_q\right|+1; -\frac{b^2}{4\alpha}\right) \Bigg\}. \end{aligned} \tag{5.46}$$

The index j_6 in (5.46) are summed from 0 to $t-1$, suggesting the LG beam is coupling into all t mode lobes of the fiber LP mode $\Psi_{s,t}$ along a radial direction.

The coupling coefficient $c^{p,l}_{s,t,'e'}$ between the LG beam and the fiber LP even mode is expressed and summarized by (5.47). Likewise, the expression (5.48) is derived for the odd mode following the identical derivation. It is worth noting that by the simplification of (5.47) and (5.48), the analytical expressions under the offset and tilted launch conditions can also be directly derived as shown in Appendix B.

$$
\begin{aligned}
c^{p,l}_{s,t,'e'} = {} & \frac{\left(\sqrt{2}\right)^{|l|}\pi \cdot B \cdot C}{{\omega_1}^{|l|+1} \cdot R^s} \cdot e^{i \cdot \theta \cdot l} \cdot \exp\left(i\Phi - ik\frac{z_0}{\cos\psi}\right) \cdot \exp\left[\left(-\frac{1}{{\omega_1}^2} - i\frac{k}{2R_1}\right){a_{off}}^2\right] \\
& \cdot \exp\left(ika_{off}\sin\psi\cos\theta\right) \\
& \cdot \sum_{j_1=0}^{|l|}\binom{|l|}{j_1} \cdot \sum_{j_2=0}^{p}\binom{p+|l|}{p-j_2}\frac{(-2)^{j_2}}{j_2!{\omega_1}^{2j_2}} \cdot \sum_{j_3=0}^{j_2}\binom{j_2}{j_3} \cdot \sum_{j_4=0}^{j_3}\binom{j_3}{j_4} \\
& \cdot \sum_{j_5=0}^{j_2-j_3}\binom{j_2-j_3}{j_5}\left(-a_{off}\right)^{|l|-j_1+2j_2-j_3-2j_5} \cdot \sum_{j_6=0}^{t-1}\binom{t-1+s}{t-1-j_6}\frac{1}{j_6!}\left(-\frac{V}{R^2}\right)^{j_6} \\
& \cdot \sum_{q=1}^{2}\left\{\frac{(|\zeta|-\varepsilon)^{\gamma_q/2}}{(|\zeta|+\varepsilon)^{\gamma_q/2}} \cdot \frac{\Gamma\left(\left(\left|\gamma_q\right|+\mu+1\right)\big/2\right)}{\Gamma\left(\left|\gamma_q\right|+1\right)} \cdot \frac{\left[-\mathrm{sgn}\left(\gamma_q\right)\right]^{\gamma_q} b^{\left|\gamma_q\right|}}{2^{\left|\gamma_q\right|+1}\alpha^{\left(\left|\gamma_q\right|+\mu+1\right)/2}}\right. \\
& \qquad \left. \cdot {}_1\mathrm{F}_1\left(\tfrac{\left|\gamma_q\right|+\mu+1}{2}; \left|\gamma_q\right|+1; -\tfrac{b^2}{4\alpha}\right)\right\}
\end{aligned}
\tag{5.47}
$$

$$
\begin{aligned}
c^{p,l}_{s,t,'o'} = {} & \frac{\left(\sqrt{2}\right)^{|l|}\pi\cdot B\cdot C}{{\omega_1}^{|l|+1}\cdot R^s}\cdot e^{i\cdot\theta\cdot l}\cdot\exp\left(i\Phi - ik\frac{z_0}{\cos\psi}+i\frac{\pi}{2}\right)\cdot\exp\left[\left(-\frac{1}{{\omega_1}^2}-i\frac{k}{2R_1}\right){a_{off}}^2\right] \\
& \cdot\exp\left(ika_{off}\sin\psi\cos\theta\right) \\
& \cdot\sum\nolimits_{j_1=0}^{|l|}\binom{|l|}{j_1}\cdot\sum\nolimits_{j_2=0}^{p}\binom{p+|l|}{p-j_2}\frac{(-2)^{j_2}}{j_2!{\omega_1}^{2j_2}}\cdot\sum\nolimits_{j_3=0}^{j_2}\binom{j_2}{j_3}\cdot\sum\nolimits_{j_4=0}^{j_3}\binom{j_3}{j_4} \\
& \cdot\sum\nolimits_{j_5=0}^{j_2-j_3}\binom{j_2-j_3}{j_5}\left(-a_{off}\right)^{|l|-j_1+2j_2-j_3-2j_5}\cdot\sum\nolimits_{j_6=0}^{t-1}\binom{t-1+s}{t-1-j_6}\frac{1}{j_6!}\left(-\frac{V}{R^2}\right)^{j_6} \qquad (5.48) \\
& \cdot\sum\nolimits_{q=1}^{2}\left\{\frac{(|\zeta|-\varepsilon)^{\gamma_q/2}}{(|\zeta|+\varepsilon)^{\gamma_q/2}}\cdot\frac{\Gamma\left(\left(\left|\gamma_q\right|+\mu+1\right)\Big/2\right)}{\Gamma\left(\left|\gamma_q\right|+1\right)}\cdot\frac{(-1)^q\left[-\operatorname{sgn}\left(\gamma_q\right)\right]^{\gamma_q}b^{|\gamma_q|}}{2^{|\gamma_q|+1}\alpha^{\left(|\gamma_q|+\mu+1\right)/2}}\right. \\
& \qquad \left.\cdot{}_1\mathrm{F}_1\left(\tfrac{\left|\gamma_q\right|+\mu+1}{2};\left|\gamma_q\right|+1;-\tfrac{b^2}{4\alpha}\right)\right\}
\end{aligned}
$$

5.4 Validation and Analysis

A well-known finite difference method (FDM) solves the scalar wave equation numerically [163, 164], and the numerical results are used to validate the analytical expressions. In both numerical and analytical methods, the fiber parameters are n_1=1.47, Δ=0.01, R=25 μm, and R_C=62.5 μm. The beam has a waist of 3 μm, and the longitudinal spacing z_0 is set 100 μm. In the FDM simulation, the maximum grid step size is 10 nm.

To validate the accuracy of the derived expressions, our analytical results are compared with corresponding numerical ones for an MMF with an infinite parabolic refractive index profile. When the LG beam is coupled into the fiber LP even modes, Fig. 5.5 presents the power coupling coefficients for the first four modes under the conditions of a central launch

(Fig. 5.5(a)), an offset launch (Fig. 5.5(b)), a tilted launch (Fig. 5.5(c)) and a generalized launch (Fig. 5.5(d)), respectively. Likewise, Fig. 5.6 shows power coupling coefficients when the LG beam is coupled into the LP odd modes. In one grid, the number in black is the analytical result, while the number in red is the relative difference between the numerical result and the corresponding analytical one. The MMF fiber allows the propagation of hundreds of modes at 850 nm. Here only four LG and LP modes are shown as examples. It is worth noting that the conclusion also applies to other modes. The errors between the power coupling coefficients from the analytical expressions and the numerical FDM are negligible. Therefore, the accuracy of the closed-form analytical expressions of power coupling coefficients is verified.

In addition, my solutions are compared with the ones in [119] and [165]. Reference [119] discusses the offset launch of the Gaussian beam into the MMF, assuming the beam waist is located at the fiber's input surface. Therefore, in our expressions, the input beam is LG_{00}, and the longitudinal spacing z_0 is $0\,\mu$m. Fig. 5.7 shows the power coupling coefficients into the fiber modes LP_{01} and LP_{11} calculated by our expression (5.29) and the solution in [119]. The radial offset values range from $0\,\mu$m (i.e., center launch) to $15\,\mu$m. Both solutions lead to the identical coupling coefficients. Reference [165] explored the influence of both beam radial offset and angular tilt of the Gaussian beam on the power coupling coefficients. It is also worth noting that their analytical expression ([165], Equation 11) derives the sum of power coupling coefficients for the LP even and odd modes. Therefore for the comparison, the power

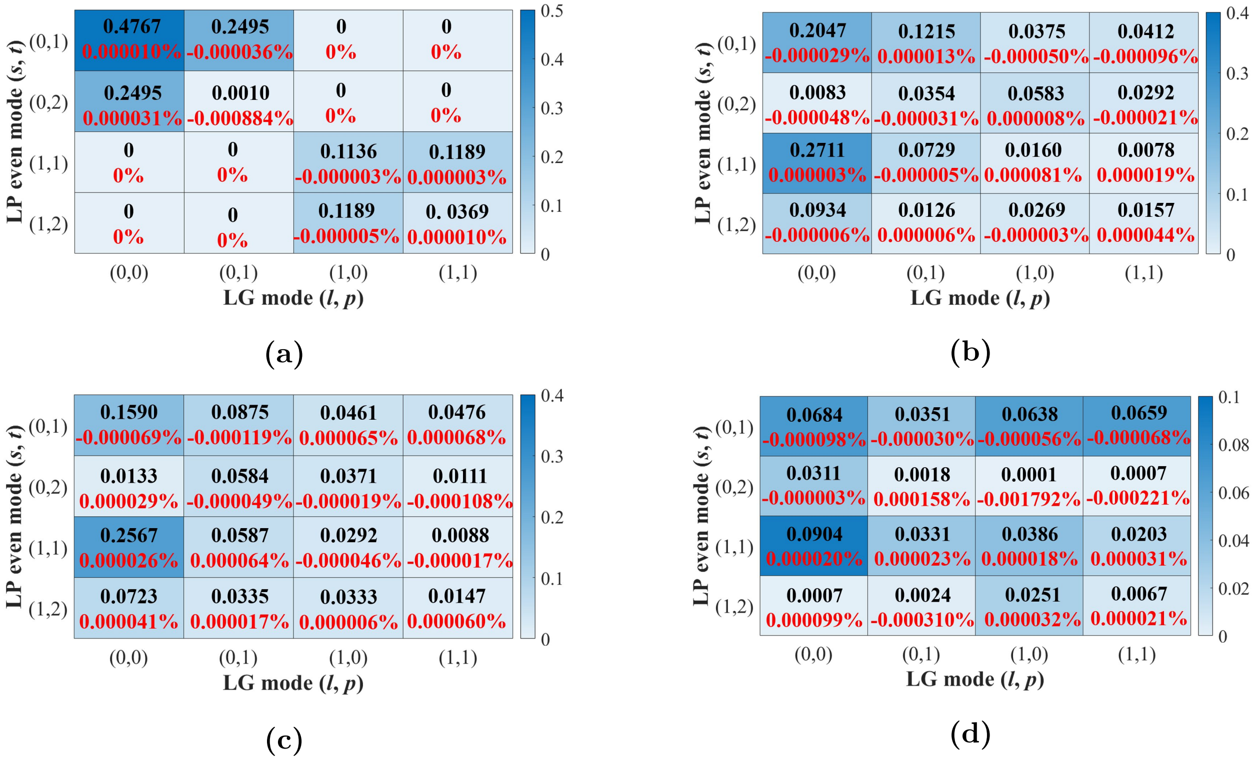

(a)

LP even mode (*s*, *t*) \ LG mode (*l*, *p*)	(0,0)	(0,1)	(1,0)	(1,1)
(0,1)	0.4767 0.000010%	0.2495 -0.000036%	0 0%	0 0%
(0,2)	0.2495 0.000031%	0.0010 -0.000884%	0 0%	0 0%
(1,1)	0 0%	0 0%	0.1136 -0.000003%	0.1189 0.000003%
(1,2)	0 0%	0 0%	0.1189 -0.000005%	0. 0369 0.000010%

(b)

LP even mode (*s*, *t*) \ LG mode (*l*, *p*)	(0,0)	(0,1)	(1,0)	(1,1)
(0,1)	0.2047 -0.000029%	0.1215 0.000013%	0.0375 -0.000050%	0.0412 -0.000096%
(0,2)	0.0083 -0.000048%	0.0354 -0.000031%	0.0583 0.000008%	0.0292 -0.000021%
(1,1)	0.2711 0.000003%	0.0729 -0.000005%	0.0160 0.000081%	0.0078 0.000019%
(1,2)	0.0934 -0.000006%	0.0126 0.000006%	0.0269 -0.000003%	0.0157 0.000044%

(c)

LP even mode (*s*, *t*) \ LG mode (*l*, *p*)	(0,0)	(0,1)	(1,0)	(1,1)
(0,1)	0.1590 -0.000069%	0.0875 -0.000119%	0.0461 0.000065%	0.0476 0.000068%
(0,2)	0.0133 0.000029%	0.0584 -0.000049%	0.0371 -0.000019%	0.0111 -0.000108%
(1,1)	0.2567 0.000026%	0.0587 0.000064%	0.0292 -0.000046%	0.0088 -0.000017%
(1,2)	0.0723 0.000041%	0.0335 0.000017%	0.0333 0.000006%	0.0147 0.000060%

(d)

LP even mode (*s*, *t*) \ LG mode (*l*, *p*)	(0,0)	(0,1)	(1,0)	(1,1)
(0,1)	0.0684 -0.000098%	0.0351 -0.000030%	0.0638 -0.000056%	0.0659 -0.000068%
(0,2)	0.0311 -0.000003%	0.0018 0.000158%	0.0001 -0.001792%	0.0007 -0.000221%
(1,1)	0.0904 0.000020%	0.0331 0.000023%	0.0386 0.000018%	0.0203 0.000031%
(1,2)	0.0007 0.000099%	0.0024 -0.000310%	0.0251 0.000032%	0.0067 0.000021%

Fig. 5.5: Power coupling coefficients between four LG beam modes and four LP even (cosine) modes for an infinite parabolic MMF. The black number in a grid is the analytical result, while the red number is the relative difference between the numerical result and the corresponding analytical one. The launch conditions are: (a) central launch; (b) offset launch with a_{off}=5 μm; (c) tilted launch with ψ=3°; (d) a generalized misalignment launch with a_{off}=5 μm, ψ=3°, and θ=90°.

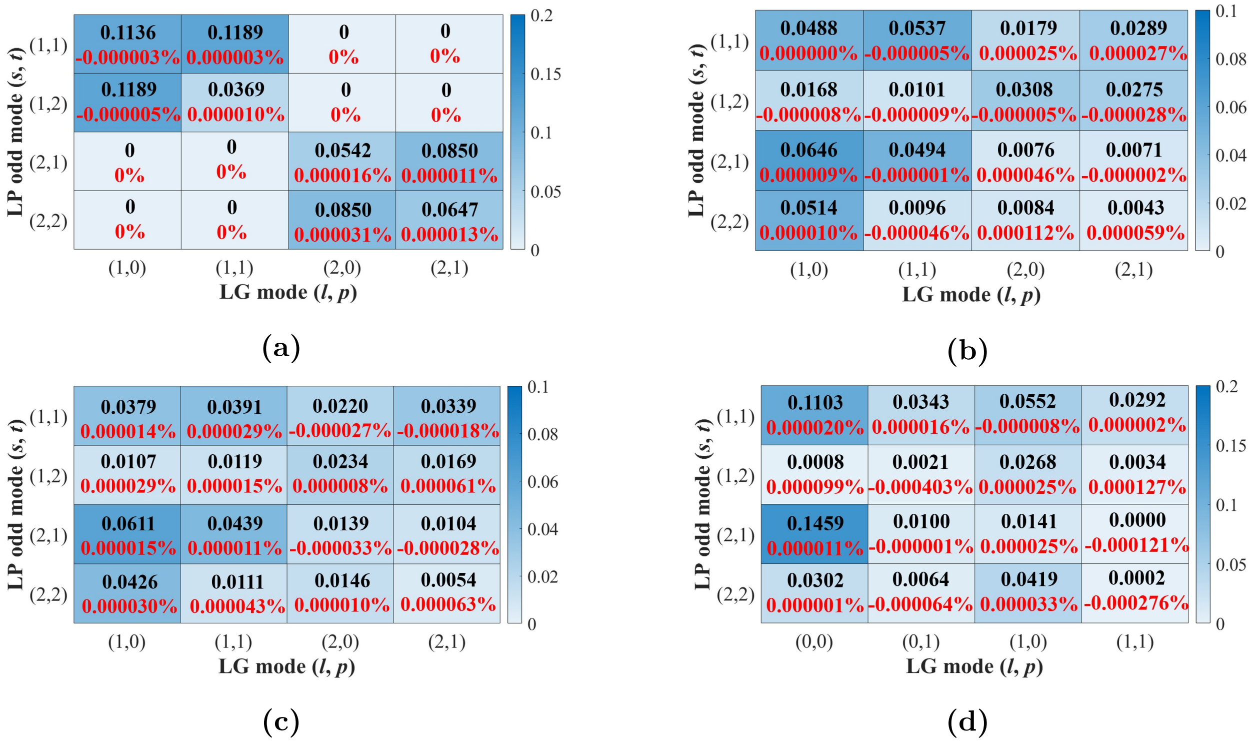

(a)

LG mode (*l*, *p*)

LP odd mode (*s*, *t*)	(1,0)	(1,1)	(2,0)	(2,1)
(1,1)	0.1136 -0.000003%	0.1189 0.000003%	0 0%	0 0%
(1,2)	0.1189 -0.000005%	0.0369 0.000010%	0 0%	0 0%
(2,1)	0 0%	0 0%	0.0542 0.000016%	0.0850 0.000011%
(2,2)	0 0%	0 0%	0.0850 0.000031%	0.0647 0.000013%

(b)

LG mode (*l*, *p*)

LP odd mode (*s*, *t*)	(1,0)	(1,1)	(2,0)	(2,1)
(1,1)	0.0488 0.000000%	0.0537 -0.000005%	0.0179 0.000025%	0.0289 0.000027%
(1,2)	0.0168 -0.000008%	0.0101 -0.000009%	0.0308 -0.000005%	0.0275 -0.000028%
(2,1)	0.0646 0.000009%	0.0494 -0.000001%	0.0076 0.000046%	0.0071 -0.000002%
(2,2)	0.0514 0.000010%	0.0096 -0.000046%	0.0084 0.000112%	0.0043 0.000059%

(c)

LG mode (*l*, *p*)

LP odd mode (*s*, *t*)	(1,0)	(1,1)	(2,0)	(2,1)
(1,1)	0.0379 0.000014%	0.0391 0.000029%	0.0220 -0.000027%	0.0339 -0.000018%
(1,2)	0.0107 0.000029%	0.0119 0.000015%	0.0234 0.000008%	0.0169 0.000061%
(2,1)	0.0611 0.000015%	0.0439 0.000011%	0.0139 -0.000033%	0.0104 -0.000028%
(2,2)	0.0426 0.000030%	0.0111 0.000043%	0.0146 0.000010%	0.0054 0.000063%

(d)

LG mode (*l*, *p*)

LP odd mode (*s*, *t*)	(0,0)	(0,1)	(1,0)	(1,1)
(1,1)	0.1103 0.000020%	0.0343 0.000016%	0.0552 -0.000008%	0.0292 0.000002%
(1,2)	0.0008 0.000099%	0.0021 -0.000403%	0.0268 0.000025%	0.0034 0.000127%
(2,1)	0.1459 0.000011%	0.0100 -0.000001%	0.0141 0.000025%	0.0000 -0.000121%
(2,2)	0.0302 0.000001%	0.0064 -0.000064%	0.0419 0.000033%	0.0002 -0.000276%

Fig. 5.6: Power coupling coefficients between four LG beam modes and four LP odd (sine) modes for an infinite parabolic MMF. The black number in a grid is the analytical result, while the red number is the relative difference between the numerical result and the corresponding analytical one. The launch conditions are: (a) central launch; (b) offset launch with a_{off}=5 μm; (c) tilted launch with ψ=3°; (d) a generalized misalignment launch with a_{off}=5 μm, ψ=3°, and θ=90°.

coupling coefficients of the LP even and odd modes are summed up, i.e., $\left|c^{0,0}_{s,t,'e'}\right|^2 + \left|c^{0,0}_{s,t,'o'}\right|^2$. Fig. 5.8 illustrates the comparison between our results and the results reported in [165] for the following launch condition: $a_{off} = 5\,\mu$m, $\psi = 3°$, and $\theta = 90°$. The obtained power coupling coefficients are identical.

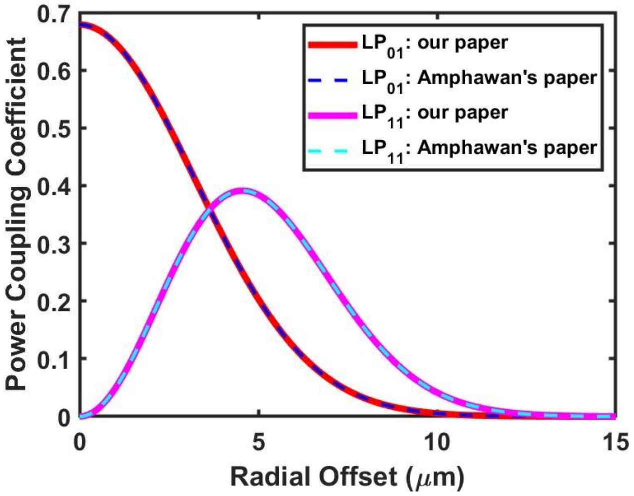

Fig. 5.7: Comparison of power coupling coefficients obtained using our analytical expressions and the result in [119] when the Gaussian beam couples into LP_{01} and LP_{11}.

In practical commercial fibers, the refractive index exponent parameter α depends on the manufacturing processes and usually has a value ranging from 1.8 to 2.2. The refractive index of the MMF has a finite power-law structure expressed by (5.3). Fig. 5.9 shows the relative power coupling coefficient difference when LG_{00} couples into the LP_{01} fiber mode. The relative coefficient difference is defined as the difference between the numerical and analytical results divided by the analytical one. The offset launch has a_{off}=5 μm; the tilted launch has ψ=3°, and the generalized misalignment launch has a_{off}=5 μm, ψ=3°, and θ=90°.

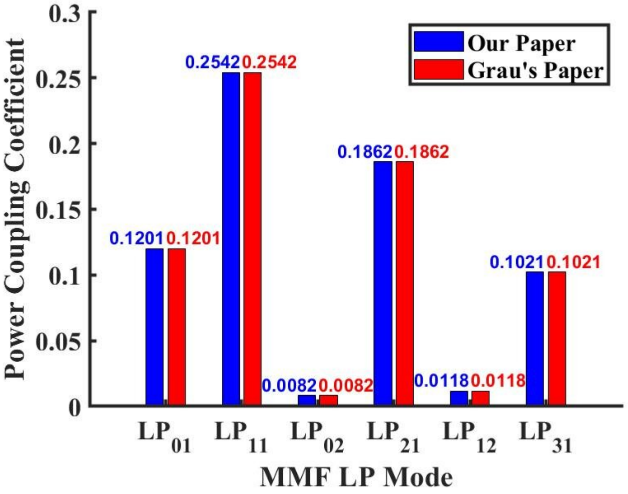

Fig. 5.8: Comparison of power coupling coefficients between our results and the results in [165], with the launch condition a_{off}=5 μm, ψ=3°, and θ=90°.

As seen in Fig. 5.9, for all launch conditions, analytical results are in good agreement with numerical results for the finite power-law MMF with α values from 1.8 to 2.2, where the maximum error is below 4%. Similarly, for high-order modes, the analytical expressions also properly calculate the power coupling coefficients for the commercially manufactured MMF. Fig. 5.10 illustrates the relative differences between the analytical and numerical results when coupling into the LP_{45} even mode. The launch conditions are the same as those in Fig. 5.9. To ensure the power coupling coefficient is over 0.01, LG_{44}, LG_{01}, LG_{01}, and LG_{11} are chosen as the input Laguerre-Gauss mode of the central launch, the offset launch, the tilted launch and the generalized launch, respectively. Based on the orthogonality of the generalized Laguerre polynomials, a conclusion can be mathematically obtained that the input mode LG_{44} is required to realize large power coupling for the central launch. When α

further deviates from 2, the relative power coefficient difference increases because of larger refractive index discrepancy between the α-exponent profile and the infinite parabolic profile. It is also worth mentioning that the curves in Fig. 5.9 and Fig. 5.10 behave quasi-linear, resulting from approximately linear dependence of the electric-field difference between the α-exponent refractive index and the infinite parabolic assumption on the value of $\alpha-2$ when α is near 2.

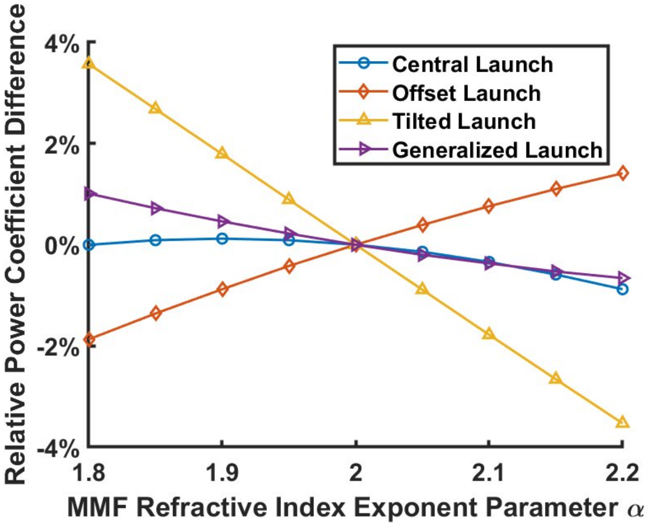

Fig. 5.9: Relative power coupling coefficient difference between the numerical results for a finite power-law MMF with α 1.8 to 2.2 and the analytical expressions, when coupling into a low-order fiber mode LP_{01}.

The simulation time are compared when using the numerical FDM and our analytical expressions obtained in Section 5.3.1-5.3.4. Each coupling coefficient is calculated 1000 times using Matlab® R2020b on an Intel® Core™ i5-7200U CPU computer. The average single-run time is obtained using the Matlab® stopwatch timer. Fig. 5.11 shows the time cost for

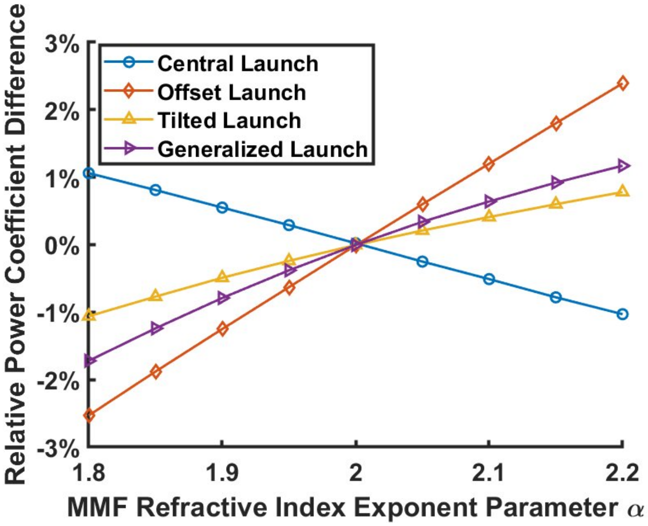

Fig. 5.10: Relative power coupling coefficient difference between the numerical results for a finite power-law MMF with α 1.8 to 2.2 and the analytical expressions, when coupling into a high-order fiber mode LP_{45}.

coupling of the LG beam mode LG_{00} into the fiber mode LP_{01} and the coupling of the LG beam mode LG_{44} into the fiber mode LP_{45}. The analytical expressions (5.14), (5.29), (5.36) and (5.47) are used to evaluate the execution time for the central launch, the offset launch, the tilted launch and the generalized launch, respectively. When coupling into LP_{01}, the analytical expressions of all four launch conditions take negligible time to calculate the power coupling coefficient. The time cost is 1 μs for the center launch, 30 μs for the tilted launch, and 50 μs for the offset launch and the generalized launch. The improvement reaches at least six orders of magnitude in comparison with the numerical FDM. Because more terms are included in the analytical expressions for the high-order MMF mode, more time is needed as shown. The time cost is 4 μs for the center launch, 0.3 ms for the tilted launch, and 10 ms for the offset launch and the generalized launch, with a significant improvement of seven, five and four orders of magnitude compared to the conventional FDM. The analytical expressions for the offset launch and the generalized launch require more arithmetical operations compared to the central launch and the tilted launch; therefore, they lead to greater execution time as shown in Fig. 5.11. Due to the large difference in computation time, especially for the coupling into high-order fiber modes, the expressions in Section 5.3.1-5.3.4 should be chosen properly given a specific application scenario.

It is worth mentioning that the number values are stored and represented by the floating-point number format in a digital computer. Most mathematical software such as MATLAB® used in this work and programming language (e.g., Java and C++) follow the IEEE Standard 754 [166] to construct the floating-point numbers. The double-precision data type is adopted here with a machine precision of 2^{-53}. Due to the limited arithmetical operations in the analytical expressions, the error caused by addition/subtraction of small numbers is expected to be negligible.

5.5 Conclusion

The closed-form expressions of power coupling coefficients have been derived for the center launch, the offset launch, the tilted launch and the generalized launch of a Laguerre-Gaussian beam into a graded-index fiber. The validity of our analytical results is confirmed by comparison with the conventional numerical FDM and can be extended to

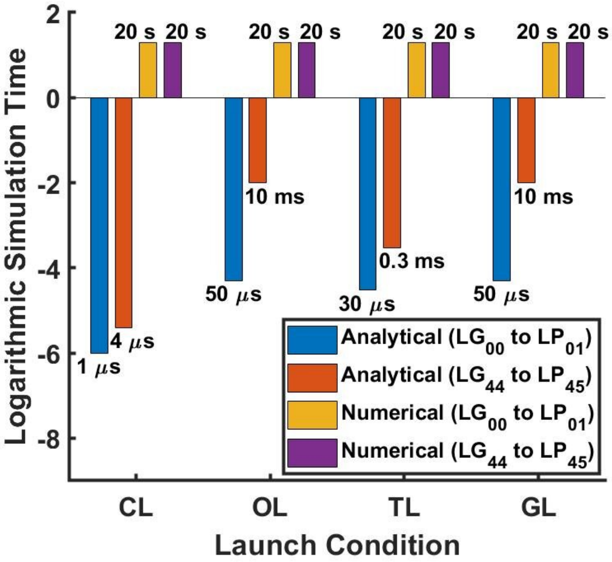

Fig. 5.11: Execution time for the calculation of the power coupling coefficient. CL: central launch; OL: offset launch; TL: tilted launch; GL: generalized launch.

calculate the power coupling coefficients for manufactured graded-index MMFs with $1.8 \leq \alpha \leq 2.2$. With analytical expressions, the calculation time cost is reduced by six orders of magnitude for the low-order fiber modes and at least four orders of magnitude for the high-order fiber modes. These analytical expressions are useful in analyzing the coupling mechanisms and parametric dependence on power coupling coefficients.

In applications such as mode selective excitation and mode division multiplexing, the launch conditions are optimized to improve transmission performance. Due to its heavy computation pressure, the numerical solutions of the power coupling coefficients are not practical to explore the optimal launch conditions considering a large number of power coupling coefficients needed to be calculated. The closed-form analytical expressions have much less computation time than the conventional numerical method. Benefiting from superior performances especially in computation time cost, the analytical expressions potentially open the door to efficiently ascertain optimal launch conditions.

In addition, the transverse electric field in the graded-index fiber exhibits the Laguerre-Gaussian mode profile. Therefore, our solutions can also benefit in the evaluation of the connector misalignment and quantify the inter-modal crosstalk induced by connector imperfection.

Chapter 6

Mitigation of Mode Partition Noise by Optimizing Launch Conditions

The multimode characteristics of vertical cavity surface emitting laser (VCSEL) sources lead to mode partition noise (MPN) impairing high-speed multimode fiber (MMF) links. A low-cost and straightforward MPN mitigation scheme is proposed by optimizing the launch condition between the VCSEL and the MMF. The dependence of the MPN on launch conditions is theoretically assessed. Simulation shows that the mode power redistribution induced by rearranging the launch condition has great potential to reduce the MPN. Experiments are carried out to demonstrate the MPN reduction. Using a 15-μm radial offset between the VCSEL and the MMF, efficient noise suppression is observed in both the frequency domain and the time domain. The work presented in this chapter has been published as a journal paper in IEEE Photonics Technology Letters [17].

6.1 Introduction

Vertical cavity surface emitting laser (VCSEL) -based multimode fiber (MMF) links dominate rack-to-rack transmission within data centers due to their low cost and low power consumption. Recently, a 1 Tbps capacity link has been demonstrated [26], and IEEE P802.3db supporting 400 Gbps operation over short-reach fiber was also projected [61]. Compared to the step-index fiber, the graded-index MMF is preferred for datacom applications, owing to its less dispersion and superior bandwidth. However, the VCSEL outputs multiple modes leading to mode competition. The power in each mode fluctuates randomly, exhibiting low-frequency intensity noise enhancement in a dispersive link, which is mode partition noise (MPN) [167, 168]. With the increasing demand of data rates and transmission distances, the noise impairment significantly influences the link performance. Equalization and forward error correction (FEC) can significantly improve the data rates and enable longer transmission reach. However, as mentioned in [70, 86, 169], conventional equalization techniques lead to MPN enhancement due to nonlinearity and randomness of the noise, which is also theoretically explained in [170]. Thus, mitigation of MPN requires to be performed before equalization in high-speed interconnects within datacenters.

As MPN is detrimental in VCSEL-MMF links, it recently attracted the attention from researchers. Authors in [134] developed a theoretical MPN model that includes the effect of modal-dispersion chromatic interaction in VCSEL-MMF channels. The impact of MPN on the performance of the received signal in MMF links was studied in [154]. Several techniques have been proposed to mitigate MPN. In [171], the use of a semiconductor optical amplifier (SOA) reduced the MPN induced by the spectral filtering effects of an Fabry–Pérot (FP) laser. In 2016, a scheme using a Mach-Zehnder interferometer (MZI) and a reflective semiconductor optical amplifier (RSOA) alleviated the noise with the improved bit error rate (BER) by three orders of the magnitude for a 10 Gbps signal [172]. These schemes inevitably require new components such as SOAs and MZIs and, thus, increase the cost of short-reach interconnects in datacenters. Encoding techniques were also introduced, shifting the electrical spectrum away from the low-frequency region. The authors in [173] demonstrated 8B/10B and Manchester encoding with PAM4 modulation format to suppress MPN. In [174], Manchester encoding in conjunction with balanced detection was employed to overcome the MPN-induced limitation. Finally, wavefront shaping techniques such as using a spatial light modulator (SLM) was used to mitigate MPN in VCSEL-MMF links [86]. The signal-to-noise ratio (SNR) improvement of a fixed sequence showed the validity of the scheme. Due to its large size, insertion loss, and cost, SLM-based technology remains challenging in deployed VCSEL-MMF link-based applications.

By optimizing the beam launch conditions at the fiber input facet, a low-cost MPN mitigation scheme is presented for VCSEL-MMF link applications. The mode power distribution over fiber is optimized, and its impact on the MPN is theoretically analyzed. With this proposed technique, the MPN mitigation is observed in the frequency domain and time domain. The low-frequency relative intensity noise (RIN), a significant frequency-domain characteristic of the MPN, is efficiently suppressed using a 15-μm beam radial offset at the fiber input facet in our experiment. The reduction in intensity noise is also observed in the time domain by measuring the signal-to-noise ratio (SNR) of an alternative zero-one bit sequence. Additionally, a 1.3-dB power penalty improvement is realized for a 10-Gbps NRZ signal after 500-m OM4 MMF transmission, benefitting from the simple MPN mitigation scheme.

6.2 Principle and theory

A simple analytical expression that estimates the level of MPN is expressed in (6.1) [175]:

$$\sigma = \frac{\kappa}{\sqrt{2}} \left[1 - e^{-(\pi \cdot B \cdot D \cdot L \cdot \Delta\lambda)^2} \right] \tag{6.1}$$

where κ is the mode partition coefficient, B is the baud rate, D is the fiber dispersion parameter, L is the fiber length, and $\Delta\lambda$ is the root-mean-square (RMS) spectral width of the VCSEL. Equation (6.1) was adopted by the IEEE 802.3 Ethernet working group as an MPN estimator [176]. It is worth noting that several assumptions are made in applying (6.1), i.e., a continuous Gaussian laser spectrum [134], a single-mode fiber channel [134,177], and an alternated zero-one sequence [177].

As these assumptions are incorrect for VCSEL-MMF links, an enhanced model suitable for VCSEL-MMF links was developed [86, 134], with the following expression:

$$\sigma^2(t) = \kappa^2 \left[\sum_{i=1}^{N} A_i \mathrm{F}_i^2(t) - \left(\sum_{i=1}^{N} A_i \mathrm{F}_i(t) \right)^2 \right] \tag{6.2}$$

where A_i is the normalized power of the ith VCSEL mode, N denotes the number of VCSEL modes. $\mathrm{F}_i(t)$ is the signal waveform modulated onto the ith VCSEL mode after propagating over the MMF and is expressed as,

$$\mathrm{F}_i(t) = \sum_{g=1}^{M} C_{ig} f_i\left(t - \tau_{ig} L\right) \tag{6.3}$$

where M is the number of MMF mode groups, C_{ig} is the power coupling coefficient between the ith VCSEL mode and the gth MMF mode group, $f_i(t)$ is the waveform before coupling to the fiber for a given bit sequence, τ_{ig} is the length-normalized temporal delay of the gth MMF mode group excited by the ith VCSEL mode, and L is the fiber length. Based on (6.2) and (6.3), it is observed that MPN strongly depends on the power coupling coefficient C_{ig} and the differential modal delay τ_{ig}. The later, τ_{ig}, is mainly determined by the fiber characteristics such as its index profile exponent parameter and its refractive index distribution. The mode group delays over MMF are quite different, directly resulting in the MPN generation. Optimization of the fiber design can reduce the differential modal delay [178] for lower MPN. Unfortunately, τ_{ig} remains invariable for a given fiber link, unless additional components are used (e.g., compensation fiber segment [179]). The power coupling coefficient, C_{ig}, is also of vital significance to MPN. Indeed, the appropriate mode group excitation will lead to an optimized fiber mode group distribution, a path to MPN alleviation. The proposed launch-condition-tuning technique exploits this aspect by optimizing mode group power distribution, due to selective excitation of the MMF mode groups under different launch conditions.

6.3 Simulation and measurement

6.3.1 Simulation Analysis

The MPN intensity is strongly dependent on the mode power distribution over the fiber, following (6.2) and (6.3). Phase manipulation using an SLM [86], a phase plate [180], or a liquid crystal on silicon (LCOS) [181] has been developed but are incompatible within datacenters due to their size, high cost, and significant loss. To overcome these drawbacks, a novel MPN mitigation method is proposed using selective launch conditions. The VCSEL beam coupling into the MMF is illustrated in Fig. 6.1(a). By optimizing the VCSEL beam launch condition at the fiber input facet, power coupling coefficients between VCSEL modes and MMF mode groups can be optimized [15, 148], and the MPN can be suppressed effectively. In the simulation, the VCSEL oxide aperture diameter is $6\,\mu$m and the spacing distance between the VCSEL and the MMF is set to $100\,\mu$m. The VCSEL beam has a center wavelength of 850 nm and a root-mean-square (rms) spectral line width of 0.65 nm. The graded-index MMF fiber, with a left-tilted mode delay profile, has a length of 500 m, a core radius of 25 μm, a maximum core refractive index of 1.47 at 850 nm, a chromatic dispersion parameter of -100 ps/(nm $\cdot$ km), and a fiber index contrast of 0.01. Fig. 6.1(b) shows the power coupling dependence on the launch conditions between the VCSEL and the MMF, where the radial offsets are 0 μm (central launch), 5 μm, 10 μm, and 15 μm, respectively. The last three launch conditions refer to so-called offset launch. The power coupling coefficients are normalized to the total power of the guided mode groups.

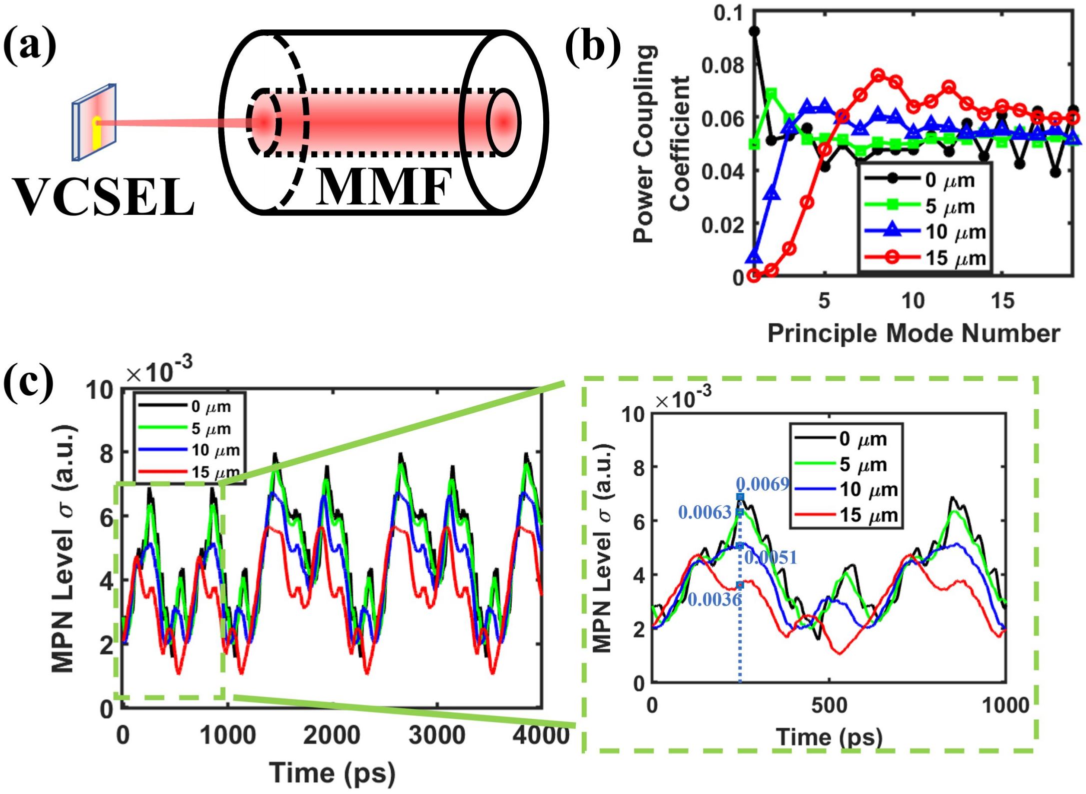

Fig. 6.1: (a) A simplified illustration of the VCSEL beam coupling into the MMF. (b) Mode group power distribution at the fiber input surface for offset values of 0 μm, 5 μm, 10 μm, and 15 μm. (c) The MPN level after 500 m MMF transmission for the offset launch values of 0 μm, 5 μm, 10 μm, and 15 μm. The sub-figure framed by dotted lines is the zoomed-in region from 0 to 1000 ps.

The power coupling coefficients differ for different launch conditions. For a large radial offset, high-order mode groups are excited where the low-order mode groups are suppressed. Comparatively, low-order mode groups earn more power from the input beam for smaller radial offsets. Selective mode excitation provides a simple possibility to suppress the MPN. The level of MPN for different launch conditions are simulated based on (6.2). The simulation uses 10 Gbps PRBS31 non-return-to-zero (NRZ) signal with the rise and fall time of 20 ps (10% to 90%). The peak-to-peak amplitude of the NRZ signal is normalized to 1. With the aforementioned modulation signal, the simulated MPN level represented by the standard deviation δ is illustrated in Fig. 6.1(c). The mode partition coefficient κ is set to 0.03, a typical value measured and used in [86, 169]. The MPN level lowers with increased radial offset values. For example, at a time delay 250 ps, the standard deviations of the MPN are 0.0069, 0.0063, 0.0051, and 0.0036 for the radial offset of 0 μm, 5 μm, 10 μm, and 15 μm. In Fig. 6.2, the averaged MPN levels over the duration of 4000 ps are calculated with different MMF refractive index exponents, output optical spectrum widths, VCSEL oxide aperture diameters, and VCSEL-to-MMF distances. The 15 μm offset launch is found to effectively mitigate the MPN.

6.3.2 Experiment Validation

Mode competition induces MPN and exhibits low-frequency noise enhancement. The RIN measurement in the low-frequency region reveals the MPN level [182]. Fig. 6.3(a) depicts

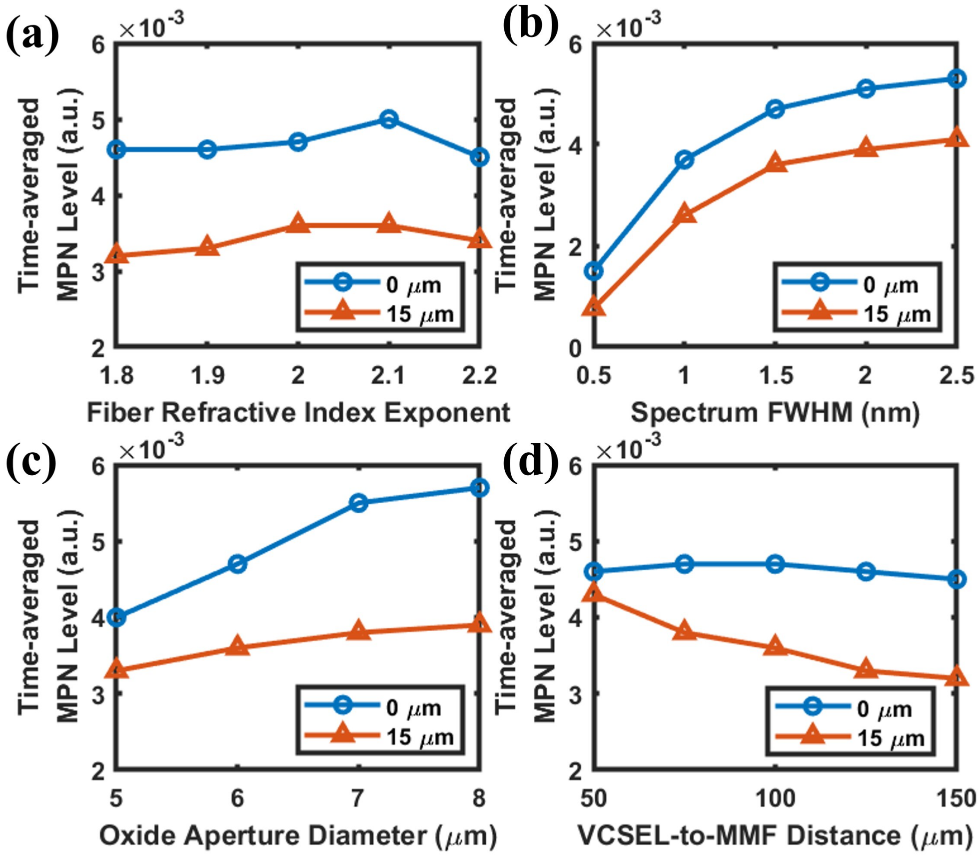

Fig. 6.2: The time-averaged MPN levels for different MMF refractive index exponents (a), optical spectrum full width at half maximum (FWHM) (b), VCSEL oxide aperture diameters (c), and VCSEL-to MMF distances (d).

an experimental setup to measure the RIN in the frequency domain. The output light of a 25-Gbps multimode VCSEL manufactured by II-VI Inc. is coupled into the MMF placed on a 6-axis micro-positioning stage with a translation resolution of 50 nm. Fig. 6.3(b) presents the laser optical spectrum with multimode behavior. The beam offset position at the fiber facet is tuned by the stage, and the tilt between the fiber and the VCSEL is controlled by a custom V-groove that can be moved. After 500-m transmission, a multimode optical receiver (Thorlabs RXM25DF) detects the optical signal. A DC block (BLK-89) removes the DC component of the electrical signal, and an electrical spectrum analyzer (ESA, Anritsu MS2668C) is used for the measurement of the RIN. The resolution bandwidth of the ESA is set to 100 kHz. The RIN is obtained from the measured power spectral density following the method proposed in [183]. Since the amplifier response is independent of the launch condition, the photoreceiver gain is simply omitted from the calculation of the RIN. Fig. 6.3(c) illustrates the calculated RIN in the frequency domain. Mode competition results in a higher RIN value at low frequencies (< 2 GHz) [167, 168]. Compared to the 0-μm offset, a 15-μm offset suppresses low-frequency RIN by 3 dB at 300 MHz and 2 dB at 1.2 GHz.

A 10 Gbps payload transmission experiment with/without the offset launch is performed. The setup configuration is shown in Fig. 6.4(a). A pulse pattern generator (PPG, Anritsu MU181020A) generates a 10 Gbps PRBS31 NRZ signal. A bias-T combines the data with a 7-mA DC current, and the VCSEL output is coupled into the MMF. At the receiver side, a multimode variable optical attenuator (VOA, Fibertronics Inc. VOA-MM50) controls the received optical power. After the optical receiver, an error detector (ED, Keysight N4903B) measures the bit error rate (BER) values as shown in Fig. 6.4(b). As observed, the transmission performance for the 15-μm radial offset is better than that for the central launch. To achieve a low BER (10^{-12}), the received optical power of -9.6 dBm is required for the 15-μm offset launch, while the power increases to -8.3 dBm for the central launch. The

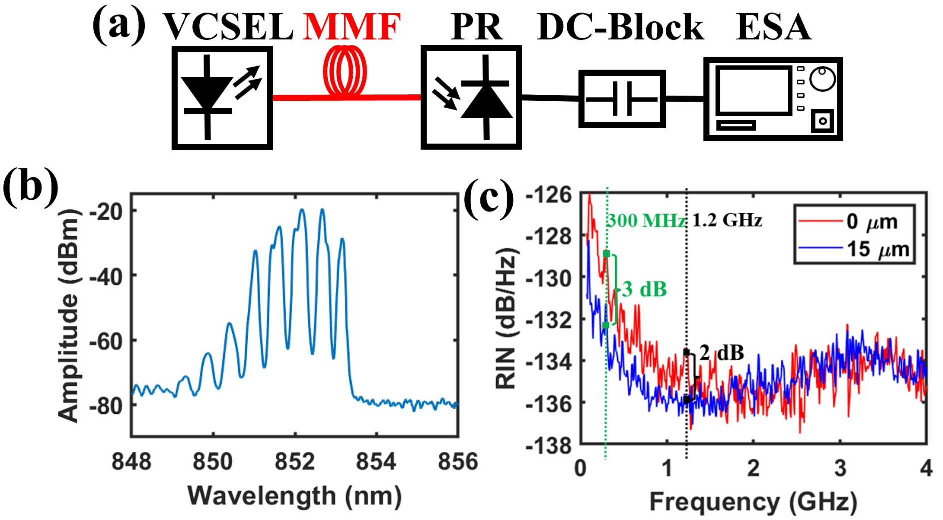

Fig. 6.3: (a) Schematic of the experiment setup for the RIN measurement. VCSEL: vertical-cavity surface-emitting laser; MMF: multimode fiber; PR: photoreceiver; ESA: electrical spectrum analyzer. (b) The VCSEL optical spectrum at 7 mA. (c) The RIN of the measured signal. The red trace represents the RIN with a 0 μm radial offset, while the blue trace shows the RIN with a 15 μm radial offset.

BER curves converge with decreasing received optical power by the fact that the receiver noise dominates the error formation at the lower optical power.

The performance improvement may also be attributed to the suppression of the dispersion-induced inter-symbol interference (ISI) by the mode-group selective excitation. To further confirm the MPN is mitigated, at the receiver side, instead of the ED, a digital communication analyzer (DCA, Agilent DCA-X 86100D) is used to measure the eye diagram as shown in Fig. 6.4(a). A data sequence (periodical bit stream of eight ones and eight zeros) at the data rate of 10 Gbps is generated by the PPG, following the method proposed by [86]. The equivalent 0.625 GHz square waveform with a 50% duty cycle

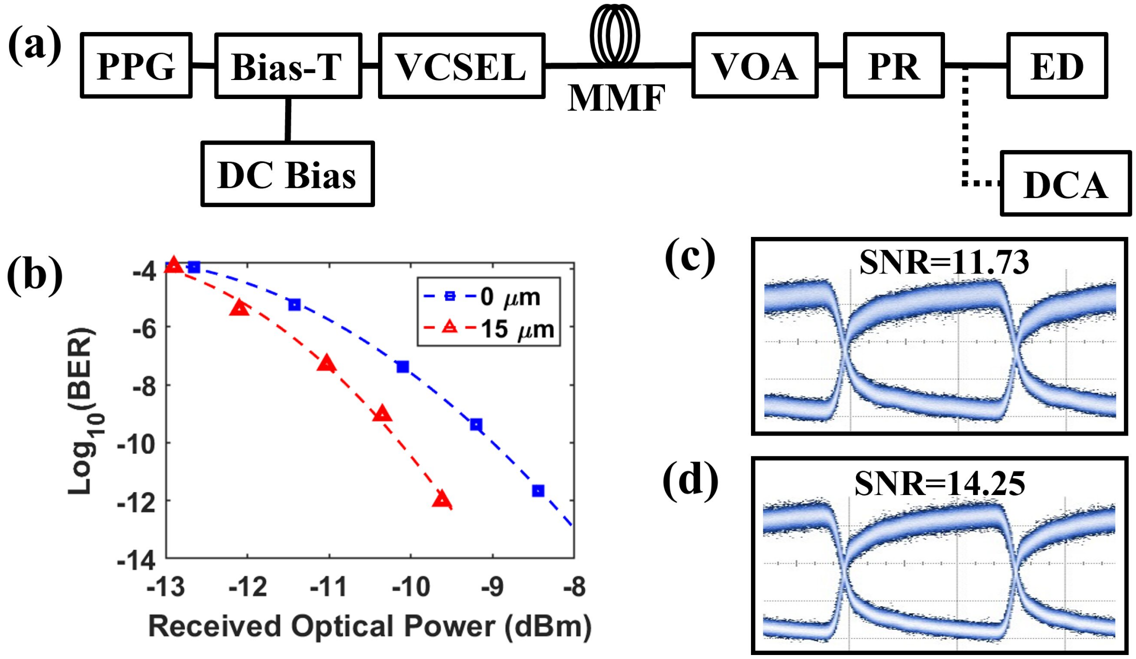

Fig. 6.4: (a) The experiment setup for the BER and eye diagram measurement. PPG: pulse pattern generator; VOA: variable optical attenuator; PR: photoreceiver; ED: error detector; DCA: digital communication analyzer. (b) BER versus received optical power for the 0-um (blue) and 15-μm (red) offset. (c) The eye diagram for radial offset value of 0 μm. (d) The eye diagram for radial offset value of 15 μm. The vertical scale is 100 mV/div, and the horizontal scale is 500 ps/div.

eliminates the influence of the dispersion-induced ISI on the transmitted data. The eye diagrams for the offset values of 0 μm and 15 μm are shown in Fig. 6.4(c) and (d). For a finite persistence of 80 s, the SNR for the 0-μm offset is 11.73, while the SNR for the 15-μm offset is 14.25. The intensity fluctuation in (d) becomes less than that in (c). The MPN, as a kind of intensity noise, is mitigated via the launch condition tuning, which leads to the SNR improvement. It should be noted that the offset launch also leads to a larger fiber bandwidth and an additional power coupling loss compared to the central launch. The measured 3-dB bandwidth is approximately 8 GHz for the central launch and 11 GHz for the 15 μm offset launch. However, in view of the low transmitted rate and the large VCSEL output power (3 dBm), these effects should have negligible effect on the measured SNR.

6.4 Conclusion

A low-cost and easily implemented scheme is validated to alleviate the MPN in a dispersive link. The MPN dependence on the mode power distribution is theoretically assessed. The MPN performance for a 15-μm beam radial offset at the fiber input facet is experimentally compared to that with the central launch. Although MMFs with various differential mode delay profiles may have different optimum launch conditions, the proof-of-principle experiments demonstrate that optimization of the launch condition can rearrange the mode power distribution and result in MPN reduction. The proposed launch-condition-tuning technique in the optical domain is transparent to the modulated data. As such, it can improve the transmission performance of the high-speed VCSEL-MMF link, reducing the complexity of the equalizer and FEC algorithm and leading to lower cost and better energy efficiency in the optical interconnects. The technique sheds light on a promising solution to mitigate the MPN for the VCSEL-MMF interconnects.

Chapter 7

Conclusion and Future Work

This chapter first summarizes the research contributions in this thesis, and then discusses some possible research direction related to VCSEL-MMF link.

7.1 Conclusion

This thesis investigates the modeling and applications of the high-speed VCSEL-MMF links for next-generation data centers.

In Chapter 2, the background information about the VCSEL-MMF link is given. First, the advances of VCSELs and MMFs are outlined. Then, multiplexing techniques, digital signal processing, advanced modulation formats, and mode selective excitation techniques are presented.

In Chapter 3, a compact high-efficient equivalent circuit model is proposed for the multi-quantum-well VCSEL. In the model, the number of nonlinear equations significantly decreases, resulting in the improved computation efficiency by 3.3-fold for three QWs-VCSEL and six-fold for five QWs VCSEL. In addition, parameter extraction becomes much more accessible than conventional MQW models as the number of parameters is reduced. The model is system-oriented and can be used as a part of the VCSEL-based link modeling.

In Chapter 4, a spectral-dependent VCSEL-MMF link model for the next-generation high-speed interconnect is proposed. Spectral-dependent coupling analysis is realized with the offset and tilt angles included. The coupling model is sensitive to mechanical misalignments (radial offset, axial offset, and 3-dimensional tilt) and optical spectra. With mode-dependent fiber effects explained, the signal evolution over the MMF is simulated by an advanced split-step small-segment method. In addition, the equivalent circuit model of a wavelength-sensitive PD, matching the multi-wavelength characteristic of the VCSEL, realizes opto-electric conversion. The link model is validated by using a 25 Gbps NRZ transmission experiment. Measured eye diagrams and bit error rates show good agreement with the simulation.

In Chapter 5, the closed-form expressions of power coupling coefficients are derived for the center launch, the offset launch, the tilted launch, and the generalized launch of a Laguerre-Gaussian beam into a graded-index fiber. The validity of our analytical results is confirmed by comparison with the conventional numerical FDM and can be extended to calculate the power coupling coefficients for manufactured graded-index MMFs with $1.8 \leq \alpha \leq 2.2$. With analytical expressions, the calculation time cost is reduced by six orders of magnitude for the low-order fiber modes and at least four orders of magnitude for the high-order fiber modes. These analytical expressions help analyze the coupling mechanisms and parametric dependence on power coupling coefficients. The launch conditions are optimized in applications such as mode selective excitation and mode division multiplexing to improve transmission performance. Due to its computation time as large as 20 s as shown in Fig. 5.11, the numerical solutions of the power coupling coefficients are not practical to explore the optimal launch conditions considering that a large number of power coupling coefficients need to be calculated. The closed-form analytical expressions spend much less computation time than the conventional numerical method. Benefiting from superior performances, especially in computation time, the analytical expressions potentially open the door to efficiently ascertain optimal launch conditions. These expressions are based on the infinite parabolic refractive index assumption; therefore, the analytical results are only limited to the manufactured graded-index telecommunication fiber, and not suitable for other kinds of fiber such as the step-index fiber and the triangular-profile graded-index fiber.

In Chapter 6, a low-cost and easily implemented scheme alleviates MPN in a dispersive link. The MPN dependence on the mode power distribution is theoretically assessed. The MPN performance for a 15-μm beam radial offset at the fiber input facet is experimentally compared to that with the central launch. Although MMFs with various differential mode delay profiles may have different optimum launch conditions, the proof-of-principle experiments demonstrate that optimization of the launch condition can rearrange the mode power distribution and result in MPN reduction. The proposed launch-condition-tuning technique in the optical domain is transparent to the modulated data. As such, it can improve the transmission performance of the high-speed VCSEL-MMF link, reducing the complexity of the equalizer and FEC algorithm and leading to lower cost and better energy efficiency in the optical interconnects. The technique sheds light on a promising solution to mitigate MPN for the VCSEL-MMF interconnects.

7.2 Future work

In this section, some possible works are presented to enhance the research of VCSEL-MMF links in the future.

First, the MIMO realization based on launch-condition tuning is an interesting topic for future research. By tuning the launch conditions of the VCSEL beams emitting from a VCSEL array, different sets of mode groups are excited to provide multiple transmission channels. The inter-channel crosstalk is an important metric to evaluate the MIMO performance. To reduce the crosstalk, the optimum launch condition can be investigated using the proposed analytical expressions proposed in Chapter 5. It is worth mentioning that although the analytical expressions have low computation burden, the calculation time is still considerable when traversing all launch conditions including the radial offset, the incidence angle and the azimuthal angle. Some intelligence algorithms, such as swarm algorithms or neural network algorithms, are expected to search for the optimum launch condition for each VCSEL beam. Moreover, the VCSEL chip distribution in one VCSEL array is well worth investigating to support the calculated launch conditions, realizing the reasonably minimum crosstalk.

Second, in Chapter 4, an advanced VCSEL-MMF link model is built. Due to the temperature effect, the VCSEL and the MMF show quite different mechanical, electrical and optical characteristics. For example, the optical output of the VCSEL with the same bias current has a lower power for a higher ambient temperature, while the fiber radius and length become larger due to thermal expansion. Also, the VCSEL has different mode emissions at different temperatures. In this sense, the link performances, such as mode power distribution, are temperature-dependent; consequently, the temperature effect on the VCSEL-MMF link is worth analyzing in the future. Up to now, there are some temperature-dependent VCSEL models; however, no well-known VCSEL-MMF link model is built to discuss the temperature effect.

Third, due to high bandwidth and low weight, the VCSEL-MMF link is preferred by the intra-satellite communication. The radiation effect from the space environment will lower the performance of the VCSEL, the MMF, and the PD. To evaluate the influence of the radiation dosage, a radiation-sensitive model is expected to assess the signal integrity over the link. To validate the model, some experimental results should be obtained for various radiation dosages. In addition, optical links designed for space applications are required to have a lifetime expectation of 15 years, which means these communication links must keep the power budget high enough to accommodate all the losses [184]. The radiation-effect-included model will help transmission performance evaluation of the intra-satellite optical communication. Because of the large temperature swing in space, the combined effect of radiation and temperature is also an intriguing theme.

Last but not the least, a record transmission date rate of 1 petabit per second over the VCSEL-MMF link is expected. Up to now, 200 Gbps per lane transmission has been realized experimentally [25]. With the multiplexing schemes including short wavelength division multiplexing (SWDM) and mode division multiplexing (MDM), the total transmission capacity is significantly enhanced. In 2017, 14.5 Tbps data was successfully transmitted over 2.2 km OM2 fiber [185]. It can be inferred that the data rate will be further increased when more advanced fiber with shorter length is used. In 2020, over 1 Pb/s C+L-band transmission was demonstrated over a 15-mode fiber [186]. With the success of 1 Pb/s transmission at the C+L band, it is believed that this data rate should also be achievable at the 850-nm band. The research on the VCSEL-MMF link will push the record of the transmission data rate higher and higher.

Appendix A

In (5.29), ${}_1\mathrm{F}_1$ is a non-elementary function in principle. Its close-form expression is derived here. Firstly, the Kummer's first property formula is given by (A-1) [161].

$$ {}_1\mathrm{F}_1\left(x\,;y\,;z\right)=\exp(z)\cdot{}_1\mathrm{F}_1\left(y-x\,;y\,;-z\right) \tag{A$-$1}$$

As such, the confluent hypergeometric function in (5.29) is transformed as.

$$\begin{aligned}&{}_1\mathrm{F}_1\left(\frac{\gamma_q{+}\mu{+}1}{2};\gamma_q{+}1;-\frac{b^2}{4\alpha}\right)\\&{=}\exp\left(-\frac{b^2}{4\alpha}\right){}_1\mathrm{F}_1\left(-\frac{\mu{-}1{-}\gamma_q}{2};\gamma_q{+}1;\frac{b^2}{4\alpha}\right)\end{aligned} \tag{A$-$2}$$

In addition, the confluent hypergeometric function is given in terms of the Laguerre polynomial by (A-3) [187].

$$\mathrm{L}_n^m\left(z\right)=\binom{n{+}m}{n}\cdot{}_1\mathrm{F}_1\left(-n;m+1;z\right) \tag{A$-$3}$$

When n and m are non-negative integers, the Laguerre polynomial $\mathrm{L}_n^m(\cdot)$ is the sum of finite terms according to the generalized Laguerre polynomial expansion (5.19). Next, I only need to prove the terms $\frac{\mu-1-\gamma_q}{2}$ and γ_q in (A-2) are non-negative integers to ensure a close-form expression.

The definitions of μ and γ_q are rewritten below. Based on (5.29), the subscript q can be 1 or 2, resulting from the two addends in (5.23). Obviously, γ_q is a non-negative integer.

$$\mu = j_1 + j_3 + s + 1 + 2j_5 + 2j_6$$

$$\gamma_1 = \left| j_1 \cdot \mathrm{sgn}\,(l) - s + 2j_4 - j_3 \right|$$

$$\gamma_2 = \left| j_1 \cdot \mathrm{sgn}\,(l) + s + 2j_4 - j_3 \right|$$

When $j_1 \cdot \mathrm{sgn}\,(l) - s + 2j_4 - j_3 \geq 0$, I have

$$\frac{\mu - 1 - \gamma_1}{2} = \frac{1 - \mathrm{sgn}\,(l)}{2} j_1 + s + j_3 - j_4 + j_5 + j_6 \tag{A−4}$$

Since $j_3 \geq j_4$, $\frac{\mu-1-\gamma_1}{2}$ can only be a non-negative integer. Likewise, when $j_1 \cdot \mathrm{sgn}\,(l) - s + 2j_4 - j_3 < 0$,

$$\frac{\mu - 1 - \gamma_1}{2} = \frac{1 + \mathrm{sgn}\,(l)}{2} j_1 + j_4 + j_5 + j_6 \tag{A−5}$$

Thus, $\frac{\mu-1-\gamma_1}{2}$ is still a non-negative integer. Similarly, $\frac{\mu-1-\gamma_2}{2}$ proves a non-negative integer as well. As a result, based on (A-2), (A-3) and (5.19), the confluent hypergeometric function

${}_1\mathrm{F}_1$ in (5.29) is given as a closed-form expression as follows.

$$\begin{aligned}
&{}_1\mathrm{F}_1\left(\frac{\gamma_q+\mu+1}{2};\gamma_q+1;-\frac{b^2}{4\alpha}\right)\\
&=\exp\left(-\frac{b^2}{4\alpha}\right)\cdot\frac{\left(\frac{\mu-1-\gamma_q}{2}\right)!\left(1+\gamma_q\right)!}{\left(\frac{\mu+1+\gamma_q}{2}\right)!}\\
&\cdot\sum_{k=0}^{\frac{\mu-1-\gamma_q}{2}}\left[\frac{(-1)^k}{k!}\binom{\frac{\mu-1+\gamma_q}{2}}{\frac{\mu-1-\gamma_q}{2}-k}\left(\frac{b^2}{4\alpha}\right)^k\right]
\end{aligned} \tag{A-6}$$

This conclusion also applies to the confluent hypergeometric functions in (5.30), (5.36), (5.37), (5.47), and (5.48).

Appendix B

Equation (5.47) is the analytical expression for the LP even mode under the generalized launch condition, while (5.29) and (5.36) are ones under the offset and tilted launch condition. Here, it is shown that (5.47) can be simplified into (5.29) and (5.36).

For the offset launch, in (5.47), $\psi = 0$ and $\theta = 0$; thus $\zeta = 0$ and $b = \left(\frac{2}{{\omega_1}^2} i - \frac{k}{R_1}\right) a_{off} \overset{\text{def}}{=} - b_{off}$. In this case, (5.47) can be converted into (B-1).

$$
\begin{aligned}
& c^{p,l}_{s,t,'e'} = \exp\left(i\Phi - ikz_0\right) \\
& \cdot \frac{\left(\sqrt{2}\right)^{|l|} \pi \cdot B \cdot C}{{\omega_1}^{|l|+1} \cdot R^s} \exp\left[\left(-\frac{1}{{\omega_1}^2} - i\frac{k}{2R_1}\right) {a_{off}}^2\right] \\
& \cdot \sum\nolimits_{j_1=0}^{|l|} \sum\nolimits_{j_2=0}^{p} \sum\nolimits_{j_3=0}^{j_2} \sum\nolimits_{j_4=0}^{j_3} \sum\nolimits_{j_5=0}^{j_2-j_3} \sum\nolimits_{j_6=0}^{t-1} \\
& \left\{ \binom{|l|}{j_1} \binom{p+|l|}{p-j_2} \binom{j_2}{j_3} \binom{j_3}{j_4} \binom{j_2-j_3}{j_5} \binom{t-1+s}{t-1-j_6} \right. \\
& \cdot \frac{(-2)^{j_2}}{j_2! {\omega_1}^{2j_2}} \frac{1}{j_6!} \left(-\frac{V}{R^2}\right)^{j_6} \left(-a_{off}\right)^{|l|-j_1+2j_2-j_3-2j_5} \\
& \cdot \sum\nolimits_{q=1}^{2} \left[\left[i \cdot \operatorname{sgn}\left(\gamma_q\right) \right]^{\gamma_q} (-1)^{\left|\gamma_q\right|+\gamma_q} \frac{\alpha^{-\frac{\left|\gamma_q\right|+\mu+1}{2}} \left(b_{off}\right)^{\left|\gamma_q\right|}}{2^{\left|\gamma_q\right|+1} \Gamma\left(\left|\gamma_q\right|+1\right)} \right. \\
& \left. \left. \cdot \Gamma\left(\frac{\left|\gamma_q\right|+\mu+1}{2}\right) {}_1\mathrm{F}_1\left(\frac{\left|\gamma_q\right|+\mu+1}{2}; \left|\gamma_q\right|+1; -\frac{b_{off}^2}{4\alpha}\right) \right] \right\}
\end{aligned}
\qquad \text{(B}-1\text{)}
$$

Due to $\left[i \cdot \operatorname{sgn}\left(\gamma_q\right)\right]^{\gamma_q} \equiv i^{\left|\gamma_q\right|}$ and $(-1)^{\left|\gamma_q\right|+\gamma_q} \equiv 1$, (B-1) becomes the same form as (5.29).

For the tilted launch, in (5.47), a_{off}=0 and θ=0; thus ζ=0. The term $\left(-a_{off}\right)^{|l|-j_1+2j_2-j_3-2j_5}$ in (5.47) is non-zero only when $|l| - j_1 + 2j_2 - j_3 - 2j_5$=0. The equality holds while j_3=0, j_2=j_5, and j_1=$|l|$. In this case, (47) is converted into (B-2).

$$
\begin{aligned}
c_{s,t,'e'}^{p,l} = {} & \exp\left(i\Phi - ikz_0\right) \cdot \frac{\left(\sqrt{2}\right)^{|l|}\pi \cdot B \cdot C}{{\omega_1}^{|l|+1} \cdot R^s} \\
& \cdot \sum\nolimits_{j_2=0}^{p} \sum\nolimits_{j_6=0}^{t-1} \left\{ \binom{p+|l|}{p-j_2} \binom{t-1+s}{t-1-j_6} \right. \\
& \cdot \frac{(-2)^{j_2}}{j_2! j_6! {\omega_1}^{2j_2}} \left(-\frac{V}{R^2}\right)^{j_6} \sum\nolimits_{q=1}^{2} \left[\left[-i\cdot\mathrm{sgn}\left(\gamma_q\right)\right]^{\gamma_q} \right. \\
& \cdot \frac{\alpha^{-\left(\left|\gamma_q\right|+\mu+1\right)\big/2} b^{\left|\gamma_q\right|}}{\Gamma\left(\left|\gamma_q\right|+1\right) 2^{\left|\gamma_q\right|+1}} \Gamma\left(\frac{\left|\gamma_q\right|+\mu+1}{2}\right) \\
& \left. \left. \cdot {}_1\mathrm{F}_1\left(\frac{\left|\gamma_q\right|+\mu+1}{2}; \left|\gamma_q\right|+1; -\frac{b^2}{4\alpha}\right) \right] \right\}
\end{aligned}
\tag{B−2}
$$

With $\left[-i\cdot\mathrm{sgn}\left(\gamma_q\right)\right]^{\gamma_q}$=$(-i)^{\left|\gamma_q\right|}$, the expression (B-2) yields (5.36).

For the LP odd mode, the expression (5.48) can also be simplified into (5.30) and (5.37) following the same derivation steps.

Bibliography

[1] Cisco, “Cisco visual networking index forecast and trends, 2017–2022 white paper,” 2019.

[2] L. Zhang, J. Chen, E. Agrell, R. Lin, and L. Wosinska, “Enabling technologies for optical data center networks: Spatial division multiplexing,” *Journal of Lightwave Technology*, vol. 38, no. 1, pp. 18–30, 2019.

[3] A. Tatarczak, *High-capacity short-range optical communication links.* PhD thesis, Ph. D. dissertation, Tech. Univ. Denmark, Kongens Lyngby, Denmark, 2016.

[4] E. Haglund, P. Westbergh, J. Gustavsson, E. Haglund, A. Larsson, M. Geen, and A. Joel, “30 GHz bandwidth 850 nm VCSEL with sub-100 fJ/bit energy dissipation at 25–50 Gbit/s,” *Electronics Letters*, vol. 51, no. 14, pp. 1096–1098, 2015.

[5] Y. Sun, R. Lingle, F. Chang, A. H. McCurdy, K. Balemarthy, R. Shubochkin, H. Nasu, T. Gray, K. Scott, W. Fan, *et al.*, “SWDM PAM4 transmission from 850 to 1066 nm over NG-WBMMF using 100g PAM4 ic chipset with real-time dsp,” *Journal of Lightwave Technology*, vol. 35, no. 15, pp. 3149–3158, 2017.

[6] J. Carpenter, B. C. Thomsen, and T. D. Wilkinson, “Degenerate mode-group division multiplexing,” *Journal of Lightwave Technology*, vol. 30, no. 24, pp. 3946–3952, 2012.

[7] R. Ryf, N. K. Fontaine, H. Chen, B. Guan, B. Huang, M. Esmaeelpour, A. Gnauck, S. Randel, S. Yoo, A. Koonen, *et al.*, “Mode-multiplexed transmission over conventional graded-index multimode fibers,” *Optics express*, vol. 23, no. 1, pp. 235–246, 2015.

[8] P. Mena, J. Morikuni, S.-M. Kang, A. Harton, and K. Wyatt, “A comprehensive circuit-level model of vertical-cavity surface-emitting lasers,” *Journal of Lightwave Technology*, vol. 17, no. 12, p. 2612, 1999.

[9] P. V. Mena, J. Morikuni, S.-M. Kang, A. Harton, and K. Wyatt, “A simple rate-equation-based thermal VCSEL model,” *Journal of lightwave Technology*, vol. 17, no. 5, p. 865, 1999.

[10] A. Vandermeer and D. Cassidy, “A rate equation model of asymmetric multiple quantum-well lasers,” *IEEE Journal of Quantum Electronics*, vol. 41, no. 7, pp. 917–924, 2005.

[11] A. Grabowski, J. Gustavsson, Z. S. He, and A. Larsson, “Large-signal equivalent circuit for datacom VCSELs,” *Journal of Lightwave Technology*, vol. 39, no. 10, pp. 3225–3236, 2021.

[12] A. Melgar, V. A. Thomas, and S. E. Ralph, “Multi-objective laser rate equation based parameter extraction using VCSEL small signal response and RIN spectra,” *Journal of Lightwave Technology*, vol. 38, no. 23, pp. 6437–6445, 2020.

[13] A. Gholami, D. Molin, and P. Sillard, “Physical modeling of 10 GbE optical communication systems,” *Journal of Lightwave Technology*, vol. 29, no. 1, pp. 115–123, 2011.

[14] S. Li, M. S. Nezami, D. Rolston, and O. Liboiron-Ladouceur, “A compact high-efficient equivalent circuit model of multi-quantum-well vertical-cavity surface-emitting lasers for high-speed interconnects,” *Applied Sciences*, vol. 10, no. 11, pp. 1–13, 2020.

[15] S. Li, M. S. Nezami, S. Mishra, and O. Liboiron-Ladouceur, “Spectral-dependent electronic-photonic modeling of high-speed VCSEL-MMF links for optimized launch conditions,” *Optics Express*, vol. 29, no. 2, pp. 2738–2756, 2021.

[16] S. Li, M. S. Nezami, and O. Liboiron-Ladouceur, “Analytical expressions for power coupling coefficients into graded-index fibers with generalized beam launch conditions,” *Journal of Lightwave Technology*, vol. 39, no. 22, pp. 7259–7273, 2021.

[17] S. Li, M. S. Nezami, and O. Liboiron-Ladouceur, “Mitigation of mode partition noise in VCSEL-MMF links by optimizing launch conditions,” *IEEE Photonics Technology Letters*, vol. 33, no. 23, pp. 1313–1316, 2021.

[18] S. Li, M. S. Nezami, B. Bourouf, D. Rolston, and O. Liboiron-Ladouceur, “A Verilog-A based VCSEL model for next generation high-speed interconnects,” in *2019 Photonics North (PN)*, vol. CFP1909V-ART, pp. 1–1, 2019.

[19] S. Li, M. S. Nezami, and O. Liboiron-Ladouceur, “Reach extension in short-reach VCSEL-MMF interconnects using a coupling-weighted approach,” in *2020 IEEE Photonics Conference (IPC)*, pp. 1–2, 2020.

[20] S. Li, H. R. Mojaver, and O. Liboiron-Ladouceur, “Tilted-beam-enabled optical equalization for PAM-4 transmission in VCSEL-MMF links,” in *2021 OSA Advanced Photonics Congress(APC)*, pp. 1–2, 2021.

[21] H. R. Mojaver, S. Li, V. Tolstikhin, K.-W. Leong, and O. Liboiron-Ladouceur, “High radix SOA-based lossless optical switch prototyping for 25 GBaud PAM4 transmission in modern intra-datacenter applications,” in *2021 Optical Fiber Communications Conference and Exhibition (OFC)*, pp. 1–3, 2021.

[22] Cisco, “Cisco global cloud index, forecast and methodology, 2016–2021 white paper,” 2018.

[23] D. Mahgerefteh, C. Thompson, C. Cole, G. Denoyer, T. Nguyen, I. Lyubomirsky, C. Kocot, and J. Tatum, “Techno-economic comparison of silicon photonics and multimode VCSELs,” *Journal of Lightwave Technology*, vol. 34, no. 2, pp. 233–242, 2016.

[24] J. Lavrencik, V. A. Thomas, S. Varughese, and S. E. Ralph, “DSP-enabled 100 Gb/s PAM-4 VCSEL MMF links,” *Journal of Lightwave Technology*, vol. 35, no. 15, pp. 3189–3196, 2017.

[25] T. Zuo, T. Zhang, S. Zhang, and L. Liu, "850-nm VCSEL based single-lane 200-Gbps PAM-4 transmission for datacenter intra-connections," *IEEE Photonics Technology Letters*, 2021.

[26] J. Lavrencik, S. Varughese, V. A. Thomas, and S. E. Ralph, "Scaling VCSEL-MMF links to 1 Tb/s using short wavelength division multiplexing," *Journal of Lightwave Technology*, vol. 36, no. 18, pp. 4138–4145, 2018.

[27] W. Fu, H. Wu, D. Wua, M. Feng, and D. Deppe, "Cryogenic oxide-VCSEL for pam-4 optical data transmission over 50 Gb/s at 77 k," *IEEE Photonics Technology Letters*, 2021.

[28] E. Heidari, H. Dalir, M. Ahmed, M. H. Teimourpour, V. J. Sorger, and R. T. Chen, "45 GHz VCSEL with multiple transverse-coupled-cavities," in *CLEO: Applications and Technology*, pp. JTh2D–5, Optical Society of America, 2020.

[29] N. Suzuki, H. Hatakeyama, K. Fukatsu, T. Anan, K. Yashiki, and M. Tsuji, "25Gbit/s operation of InGaAs-based VCSELs," *Electronics Letters*, vol. 42, no. 17, pp. 975–976, 2006.

[30] K. Yashiki, N. Suzuki, K. Fukatsu, T. Anan, H. Hatakeyama, and M. Tsuji, "1.1-μm-range high-speed tunnel junction vertical-cavity surface-emitting lasers," *IEEE Photonics Technology Letters*, vol. 19, no. 23, pp. 1883–1885, 2007.

[31] T. Anan, N. Suzuki, K. Yashiki, K. Fukatsu, H. Hatakeyama, T. Akagawa, K. Tokutome, and M. Tsuji, “High-speed 1.1-μm-range InGaAs VCSELs,” in *OFC/NFOEC 2008-2008 Conference on Optical Fiber Communication/National Fiber Optic Engineers Conference*, pp. 1–3, IEEE, 2008.

[32] A. Mutig, G. Fiol, P. Moser, D. Arsenijevic, V. Shchukin, N. Ledentsov, S. Mikhrin, I. Krestnikov, D. Livshits, A. Kovsh, *et al.*, “120 °C 20 Gbit/s operation of 980 nm VCSEL,” *Electronics Letters*, vol. 44, no. 22, pp. 1305–1306, 2008.

[33] R. H. Johnson and D. M. Kuchta, “30 Gb/s directly modulated 850 nm datacom VCSELs,” in *Conference on Lasers and Electro-Optics*, p. CPDB2, Optical Society of America, 2008.

[34] Y.-C. Chang and L. A. Coldren, “Efficient, high-data-rate, tapered oxide-aperture vertical-cavity surface-emitting lasers,” *IEEE Journal of Selected Topics in Quantum Electronics*, vol. 15, no. 3, pp. 704–715, 2009.

[35] P. Westbergh, J. S. Gustavsson, A. Haglund, A. Larsson, F. Hopfer, G. Fiol, D. Bimberg, and A. Joel, “32 Gbit/s multimode fibre transmission using high-speed, low current density 850 nm VCSEL,” *Electronics letters*, vol. 45, no. 7, pp. 366–368, 2009.

[36] A. Mutig, S. Blokhin, A. Nadtochiy, G. Fiol, J. Lott, V. Shchukin, N. Ledentsov, and D. Bimberg, “Frequency response of large aperture oxide-confined 850 nm vertical cavity surface emitting lasers,” *Applied Physics Letters*, vol. 95, no. 13, p. 131101, 2009.

[37] P. Westbergh, J. S. Gustavsson, B. Kögel, A. Haglund, A. Larsson, A. Mutig, A. Nadtochiy, D. Bimberg, and A. Joel, “40 Gbit/s error-free operation of oxide-confined 850 nm VCSEL,” *Electronics Letters*, vol. 46, no. 14, pp. 1014–1016, 2010.

[38] L. A. Graham, H. Chen, D. Gazula, T. Gray, J. K. Guenter, B. Hawkins, R. Johnson, C. Kocot, A. N. MacInnes, G. D. Landry, *et al.*, “The next generation of high speed VCSELs at Finisar,” in *Vertical-Cavity Surface-Emitting Lasers XVI*, vol. 8276, p. 827602, International Society for Optics and Photonics, 2012.

[39] P. Westbergh, R. Safaisini, E. Haglund, B. Kögel, J. S. Gustavsson, A. Larsson, M. Geen, R. Lawrence, and A. Joel, “High-speed 850 nm VCSELs with 28 GHz modulation bandwidth operating error-free up to 44 Gbit/s,” *Electronics Letters*, vol. 48, no. 18, pp. 1145–1147, 2012.

[40] J.-W. Shi, J.-C. Yan, J.-M. Wun, J. Chen, and Y.-J. Yang, “Oxide-relief and Zn-diffusion 850-nm vertical-cavity surface-emitting lasers with extremely low energy-to-data-rate ratios for 40 Gbit/s operations,” *IEEE Journal of Selected Topics in Quantum Electronics*, vol. 19, no. 2, pp. 7900208–7900208, 2012.

[41] C. Xie, N. Li, S. Huang, C. Liu, L. Wang, and K. P. Jackson, "The next generation high data rate VCSEL development at SEDU," in *Vertical-Cavity Surface-Emitting Lasers XVII*, vol. 8639, p. 863903, International Society for Optics and Photonics, 2013.

[42] P. Westbergh, R. Safaisini, E. Haglund, J. S. Gustavsson, A. Larsson, M. Geen, R. Lawrence, and A. Joel, "High-Speed Oxide Confined 850-nm VCSELs Operating Error-Free at 40 Gb/s up to 85°," *IEEE Photonics Technology Letters*, vol. 25, no. 8, pp. 768–771, 2013.

[43] P. Westbergh, E. P. Haglund, E. Haglund, R. Safaisini, J. S. Gustavsson, and A. Larsson, "High-speed 850 nm VCSELs operating error free up to 57 Gbit/s," *Electronics Letters*, vol. 49, no. 16, pp. 1021–1023, 2013.

[44] H. Dalir and F. Koyama, "29 GHz directly modulated 980 nm vertical-cavity surface emitting lasers with bow-tie shape transverse coupled cavity," *Applied Physics Letters*, vol. 103, no. 9, p. 091109, 2013.

[45] F. Tan, M.-K. Wu, M. Liu, M. Feng, and N. Holonyak, "850 nm oxide-VCSEL with low relative intensity noise and 40 Gb/s error free data transmission," *IEEE Photonics Technology Letters*, vol. 26, no. 3, pp. 289–292, 2013.

[46] H. Li, P. Wolf, P. Moser, G. Larisch, J. A. Lott, and D. Bimberg, "Temperature-stable 980-nm VCSELs for 35-Gb/s operation at 85 °C with 139-fJ/bit dissipated heat," *IEEE photonics technology letters*, vol. 26, no. 23, pp. 2349–2352, 2014.

[47] P. Moser, J. Lott, P. Wolf, G. Larisch, H. Li, and D. Bimberg, “Error-free 46 Gbit/s operation of oxide-confined 980 nm VCSELs at 85 °C,” *Electronics Letters*, vol. 50, no. 19, pp. 1369–1371, 2014.

[48] K.-L. Chi, J.-L. Yen, J.-M. Wun, J.-W. Jiang, I.-C. Lu, J. Chen, Y.-J. Yang, and J.-W. Shi, “Strong wavelength detuning of 850 nm vertical-cavity surface-emitting lasers for high-speed (¿40 Gbit/s) and low-energy consumption operation,” *IEEE Journal of Selected Topics in Quantum Electronics*, vol. 21, no. 6, pp. 470–479, 2015.

[49] D. M. Kuchta, A. V. Rylyakov, C. L. Schow, J. E. Proesel, C. W. Baks, P. Westbergh, J. S. Gustavsson, and A. Larsson, “A 50 Gb/s NRZ modulated 850 nm VCSEL transmitter operating error free to 90 °C,” *Journal of Lightwave technology*, vol. 33, no. 4, pp. 802–810, 2015.

[50] M. Liu, C. Y. Wang, M. Feng, and N. Holonyak, “850 nm oxide-confined VCSELs with 50 Gb/s error-free transmission operating up to 85 °C,” in *CLEO: Science and Innovations*, pp. SF1L–6, Optical Society of America, 2016.

[51] G. Larisch, P. Moser, J. A. Lott, and D. Bimberg, “Impact of photon lifetime on the temperature stability of 50 Gb/s 980 nm VCSELs,” *IEEE Photonics Technology Letters*, vol. 28, no. 21, pp. 2327–2330, 2016.

[52] K.-L. Chi, G. Stepniak, J. P. Turkiewicz, J.-W. Shi, Y.-X. Shi, X.-N. Chen, J. J. Chen, Y.-J. Yang, J.-R. Kropp, N. Ledentsov, M. Agustin, and N. N. Ledentsov,

"Single-mode 850-nm VCSELs for 54-Gb/s ON–OFF keying transmission over 1-km multi-mode fiber," *IEEE Photonics Technology Letters*, vol. 28, no. 12, pp. 1367–1370, 2016.

[53] E. Simpanen, J. Gustavsson, E. Haglund, E. Haglund, A. Larsson, W. Sorin, S. Mathai, and M. Tan, "1060 nm single-mode vertical-cavity surface-emitting laser operating at 50 Gbit/s data rate," *Electronics Letters*, vol. 53, no. 13, pp. 869–871, 2017.

[54] R. Rosales, M. Zorn, and J. A. Lott, "30-GHz bandwidth with directly current-modulated 980-nm oxide-aperture VCSELs," *IEEE Photonics Technology Letters*, vol. 29, no. 23, pp. 2107–2110, 2017.

[55] N. Haghighi, G. Larisch, R. Rosales, M. Zorn, and J. A. Lott, "35 GHz bandwidth with directly current modulated 980 nm oxide aperture single cavity VCSELs," in *2018 IEEE International Semiconductor Laser Conference (ISLC)*, pp. 1–2, IEEE, 2018.

[56] H.-L. Wang, W. Fu, J. Qiu, and M. Feng, "850 nm VCSELs for 50 Gb/s NRZ error-free transmission over 100-meter OM4 and up to 115 °C operation," in *Optical Fiber Communication Conference*, pp. W3A–1, Optical Society of America, 2019.

[57] L. Chorchos, N. Ledentsov, J. R. Kropp, V. A. Shchukin, V. P. Kalosha, A. Lewandowski, J. Turkiewicz, and N. N. Ledentsov, "Energy efficient 850 nm VCSEL based optical transmitter and receiver link capable of 80 Gbit/s NRZ multi-mode fiber

data transmission," *Journal of Lightwave Technology*, vol. 38, no. 7, pp. 1747–1752, 2020.

[58] L. M. Giovane, J. Wang, M. R. Murty, A. L. Harren, A.-N. Cheng, D. Dolfi, Z.-W. Feng, N. Leong, A. Sridhara, S.-J. Taslim, *et al.*, "Development of Next Generation Data Communication VCSELs," in *Optical Fiber Communication Conference*, pp. M3D–5, Optical Society of America, 2020.

[59] N. Ledentsov, L. Chorchos, O. Makarov, J.-R. Kropp, V. Shchukin, V. Kalosha, J. Turkiewicz, N. Cherkashin, and N. Ledentsov, "Quantum-dot oxide-confined 850-nm VCSELs with extreme temperature stability operating at 25 Gbit/s up to 180deg c," in *Vertical-Cavity Surface-Emitting Lasers XXIV*, vol. 11300, p. 113000H, International Society for Optics and Photonics, 2020.

[60] *Differential Mode Delay Measurement of Multimode Fiber in the Time Domain.* Telecommunications Industry Association, 2003.

[61] IEEE 802.3 Ethernet working group, "IEEE P802.3db 100 Gb/s, 200 Gb/s, and 400 Gb/s short reach fiber task force."

[62] C. Urricariet, "SWDM: The lowest total cost solution for 40G/100G in the enterprise data center," *Finisar White Paper*, 2017.

[63] K. Takenaga, Y. Arakawa, S. Tanigawa, N. Guan, S. Matsuo, K. Saitoh, and M. Koshiba, "Reduction of crosstalk by trench-assisted multi-core fiber," in *Optical Fiber Communication Conference*, p. OWJ4, Optical Society of America, 2011.

[64] G. Xie, Y. Ren, Y. Yan, H. Huang, N. Ahmed, L. Li, Z. Zhao, C. Bao, M. Tur, S. Ashrafi, *et al.*, "Experimental demonstration of a 200-Gbit/s free-space optical link by multiplexing laguerre–gaussian beams with different radial indices," *Optics letters*, vol. 41, no. 15, pp. 3447–3450, 2016.

[65] K. Benyahya, C. Simonneau, A. Ghazisaeidi, N. Barré, P. Jian, J.-F. Morizur, G. Labroille, M. Bigot, P. Sillard, J. G. Provost, *et al.*, "Multiterabit transmission over OM2 multimode fiber with wavelength and mode group multiplexing and direct detection," *Journal of lightwave technology*, vol. 36, no. 2, pp. 355–360, 2018.

[66] J. Lavrencik, E. Simpanen, N. Haghighi, S. Varughese, J. S. Gustavsson, E. Haglund, W. Sorin, S. Mathai, M. Tan, J. A. Lott, *et al.*, "Error-free 850nm to 1060nm VCSEL links: feasibility of 400Gbps and 800Gbps 8λ-SWDM," in *45th European Conference on Optical Communication (ECOC 2019)*, pp. 1–4, IET, 2019.

[67] S. A. Gebrewold, A. Josten, B. Baeuerle, M. Stubenrauch, S. Eitel, and J. Leuthold, "PAM-8 108 Gbit/s transmission using an 850nm multi-mode VCSEL," in *The European Conference on Lasers and Electro-Optics*, p. CI_4_6, Optical Society of America, 2017.

[68] N. Bamiedakis, X. Dong, D. Cunningham, I. White, and R. Penty, “Single-lane > 100 Gb/s CAP-based data transmission over VCSEL-MMF links using low-complexity equalization,” in *Metro and Data Center Optical Networks and Short-Reach Links IV*, vol. 11712, p. 117120L, International Society for Optics and Photonics, 2021.

[69] L. Chorchos, N. Ledentsov Jr, O. Makarov, P. Scholz, U. Hecht, C. Kottke, V. Jungnickel, R. Freund, V. A. Shchukin, V. P. Kalosha, *et al.*, “NRZ, DB, and DMT performance for short-reach VCSEL-based optical interconnects,” in *Optical Interconnects XXI*, vol. 11692, p. 116920D, International Society for Optics and Photonics, 2021.

[70] F. Tian, Q. Zhou, and C. Yang, “Gaussian mixture model-hidden markov model based nonlinear equalizer for optical fiber transmission,” *Optics express*, vol. 28, no. 7, pp. 9728–9737, 2020.

[71] Q. Zhou, F. Zhang, and C. Yang, “AdaNN: Adaptive neural network-based equalizer via online semi-supervised learning,” *Journal of Lightwave Technology*, vol. 38, no. 16, pp. 4315–4324, 2020.

[72] L. Ge, W. Zhang, C. Liang, and Z. He, “Threshold-based pruned retraining volterra equalization for 100 Gbps/lane and 100-m optical interconnects based on VCSEL and MMF,” *Journal of Lightwave Technology*, vol. 37, no. 13, pp. 3222–3228, 2019.

[73] L. Ge, W. Zhang, C. Liang, and Z. He, "Compressed neural network equalization based on iterative pruning algorithm for 112-Gbps VCSEL-enabled optical interconnects," *Journal of Lightwave Technology*, vol. 38, no. 6, pp. 1323–1329, 2020.

[74] W.-J. Huang, W.-F. Chang, C.-C. Wei, J.-J. Liu, Y.-C. Chen, K.-L. Chi, C.-L. Wang, J.-W. Shi, and J. Chen, "93% complexity reduction of Volterra nonlinear equalizer by ι_1-regularization for 112-Gbps PAM-4 850-nm VCSEL optical interconnect," in *2018 Optical Fiber Communications Conference and Exposition (OFC)*, pp. 1–3, IEEE, 2018.

[75] X. Dong, N. Bamiedakis, D. G. Cunningham, R. V. Penty, and I. H. White, "A novel equalizer for 112 Gb/s CAP-based data transmission over 150 m MMF links," *Journal of Lightwave Technology*, vol. 37, no. 23, pp. 5937–5944, 2019.

[76] X. Dong, N. Bamiedakis, D. Cunningham, R. Penty, and I. White, "112 Gb/s CAP-based data transmission over 100 m MMF links using an artificial neural network equalizer," in *CLEO: Science and Innovations*, pp. SM1G–3, Optical Society of America, 2019.

[77] D. H. Sim, Y. Takushima, and Y. C. Chung, "Transmission of 10-Gb/s and 40-Gb/s signals over 3.7 km of multimode fiber using mode-field matched center launching technique," in *Optical Fiber Communication Conference*, p. OTuL3, Optical Society of America, 2007.

[78] M. Kim, B. G. Kim, S. Bae, and Y. C. Chung, “112-Gb/s PAM4 transmission over 1 km of MMF with mode-field matched center-launching in 850-nm band,” *IEEE Photonics Technology Letters*, vol. 33, no. 1, pp. 23–26, 2020.

[79] J. Carpenter and T. D. Wilkinson, “Holographic offset launch for dynamic optimization and characterization of multimode fiber bandwidth,” *Journal of Lightwave Technology*, vol. 30, no. 10, pp. 1437–1443, 2012.

[80] J. Carpenter and T. D. Wilkinson, “Adaptive enhancement of multimode fibre bandwidth by twin-spot offset launch,” in *Conference on Lasers and Electro-Optics/Pacific Rim*, p. C413, Optical Society of America, 2011.

[81] N. Sheffi and D. Sadot, “Tilted gaussian beams multiplexer for graded-index multimode fiber in data-centers interconnections,” *IEEE Photonics Journal*, vol. 7, no. 3, pp. 1–16, 2015.

[82] L. Geng, C. Kwok, S. Lee, J. Ingham, R. Penty, I. White, and D. Cunningham, “Efficient line launch for bandwidth improvement of 10 Gbit/s multimode fibre links using elliptical gaussian beam,” in *36th European Conference and Exhibition on Optical Communication*, pp. 1–3, IEEE, 2010.

[83] C.-A. Bunge, S. Choi, and K. Oh, “Analysis of ring launching scheme using hollow optical fibre mode converter for 10 Gbps multimode fibre communication,” *Optical Fiber Technology*, vol. 12, no. 1, pp. 48–58, 2006.

[84] T. Joseph and J. John, "Modified twin-spot launching: an improved launching technique for enhancing data rates in multimode fiber," *Applied Optics*, vol. 56, no. 4, p. 838, 2017.

[85] J. Harriman, S. Serati, and J. Stockley, "Comparison of transmissive and reflective spatial light modulators for optical manipulation applications," in *Optical Trapping and Optical Micromanipulation II*, vol. 5930, p. 59302D, International Society for Optics and Photonics, 2005.

[86] C. Liang, W. Zhang, L. Ge, and Z. He, "Mode partition noise mitigation for VCSEL-MMF links by using wavefront shaping technique," *Optics Express*, vol. 26, no. 22, p. 28641, 2018.

[87] A. Amphawan and Y. Fazea, "Laguerre-Gaussian mode division multiplexing in multimode fiber using SLMs in VCSEL arrays," *Journal of the European Optical Society-Rapid publications*, vol. 12, no. 1, pp. 1–11, 2016.

[88] L. Geng, S. Lee, K. William, R. Penty, I. White, and D. Cunningham, "Symmetrical 2-D hermite-gaussian square launch for high bit rate transmission in multimode fiber links," in *2011 Optical Fiber Communication Conference and Exposition and the National Fiber Optic Engineers Conference*, pp. 1–3, IEEE, 2011.

[89] W. H. Hofmann, P. Moser, and D. Bimberg, "Energy-efficient VCSELs for interconnects," *IEEE Photonics Journal*, vol. 4, no. 2, pp. 652–656, 2012.

[90] A. Suzuki, Y. Wakazono, T. Ishikawa, Y. Hashimoto, H. Masuda, S. Suzuki, M. Tamura, T. i. Suzuki, K. Kikuchi, H. Nakagawa, M. Aoyagi, and T. Mikawa, "Low-cost optical subassembly using VCSEL pre-self-aligned with optical fiber for optical interconnect applications," *Journal of Lightwave Technology*, vol. 27, no. 20, pp. 4516–4523, 2009.

[91] G. Kanakis, N. Iliadis, W. Soenen, B. Moeneclaey, N. Argyris, D. Kalavrouziotis, S. Spiga, P. Bakopoulos, and H. Avramopoulos, "High-speed VCSEL-based transceiver for 200 GbE short-reach intra-datacenter optical interconnects," *Applied Sciences*, vol. 9, no. 12, p. 2488, 2019.

[92] H.-Y. Kao, Y.-C. Chi, C.-T. Tsai, S.-F. Leong, C.-Y. Peng, H.-Y. Wang, J. J. Huang, J.-J. Jou, T.-T. Shih, H.-C. Kuo, W.-H. Cheng, C.-H. Wu, and G.-R. Lin, "Few-mode VCSEL chip for 100-Gb/s transmission over 100 m multimode fiber," *Photonics Research*, vol. 5, no. 5, p. 507, 2017.

[93] M. Raj, M. Monge, and A. Emami, "A modelling and nonlinear equalization technique for a 20 Gb/s 0.77 pJ/b VCSEL transmitter in 32 nm SOI CMOS," *IEEE Journal of Solid-State Circuits*, vol. 51, no. 8, pp. 1734–1743, 2016.

[94] G. Belfiore, M. Khafaji, R. Henker, and F. Ellinger, "A 50 Gb/s 190 mW asymmetric 3-tap FFE VCSEL driver," *IEEE Journal of Solid-State Circuits*, vol. 52, no. 9, pp. 2422–2429, 2017.

[95] C. Qi, X. Shi, and G. Wang, "Thermal circuit model of MQW VCSEL laser," in *2010 International Conference on Microwave and Millimeter Wave Technology*, IEEE, 2010.

[96] A. Horri and R. Faez, "Large signal analysis of double quantum well transistor laser," *Optical and Quantum Electronics*, vol. 45, no. 5, pp. 389–399, 2012.

[97] S. Hu, X. He, Y. He, J. Su, C. Li, A. Hu, and X. Guo, "Impact of damping on high speed 850 nm VCSEL performance," *Journal of Semiconductors*, vol. 39, no. 11, pp. 1–4, 2018.

[98] C.-C. Shen, T.-C. Hsu, Y.-W. Yeh, C.-Y. Kang, Y.-T. Lu, H.-W. Lin, H.-Y. Tseng, Y.-T. Chen, C.-Y. Chen, C.-C. Lin, C.-H. Wu, P.-T. Lee, Y. Sheng, C.-H. Chiu, and H.-C. Kuo, "Design, modeling, and fabrication of high-speed VCSEL with data rate up to 50 Gb/s," *Nanoscale Research Letters*, vol. 14, no. 1, pp. 276–281, 2019.

[99] C. Zhang, R. ElAfandy, and J. Han, "Distributed bragg reflectors for GaN-based vertical-cavity surface-emitting lasers," *Applied Sciences*, vol. 9, no. 8, p. 1593, 2019.

[100] E. P. Haglund, *Vertical-Cavity Surface-Emitting Lasers: Large Signal Dynamics and Silicon Photonics Integration.* PhD thesis, Chalmers University of Technology, Gothenburg, Sweden, 2016.

[101] J. A. Brum and G. Bastard, "Resonant carrier capture by semiconductor quantum wells," *Physical Review B*, vol. 33, no. 2, pp. 1420–1423, 1986.

[102] Y. Zhang, *Self-heating control of edge emitting and vertical cavity surface emitting lasers*. PhD thesis, University of Central Florida, Orlando, FL, USA, 2014.

[103] D. McDonald and R. O'Dowd, "Comparison of two- and three-level rate equations in the modeling of quantum-well lasers," *IEEE Journal of Quantum Electronics*, vol. 31, no. 11, pp. 1927–1934, 1995.

[104] P. Weetman, *Modelling Quantum Well Lasers*. PhD thesis, the University of Waterloo, Waterloo, ON, Canada, 2002.

[105] M. A. Hopkins, D. W. E. Allsopp, M. J. Kappers, R. A. Oliver, and C. J. Humphreys, "The ABC model of recombination reinterpreted: Impact on understanding carrier transport and efficiency droop in InGaN/GaN light emitting diodes," *Journal of Applied Physics*, vol. 122, no. 23, p. 234505, 2017.

[106] J. Yan, J. Wang, C. Tang, X. Liu, G. Zhang, and Y. He, "An electrooptothermal-coupled circuit-level model for VCSELs under pulsed condition," *IEEE Transactions on Industrial Electronics*, vol. 66, no. 2, pp. 1315–1324, 2019.

[107] S. Entezam, A. Zarifkar, and M. H. Sheikhi, "Thermal equivalent circuit model for coupled-cavity surface-emitting lasers," *IEEE Journal of Quantum Electronics*, vol. 51, no. 4, pp. 1–8, 2015.

[108] T. T. Bich-Ha and J.-C. Mollier, "Noise equivalent circuit of a two-mode semiconductor laser with the contribution of both the linear and the nonlinear gain," *IEEE Journal of Selected Topics in Quantum Electronics*, vol. 3, no. 2, pp. 304–308, 1997.

[109] S. K. Pavan, J. Lavrencik, and S. E. Ralph, "New model for mode partition noise in VCSEL-MMF links based on langevin-driven spatio-temporal rate equations," *Journal of Lightwave Technology*, vol. 34, no. 16, pp. 3733–3751, 2016.

[110] A. Tatarczak, X. Lu, and I. T. Monroy, "Improving the capacity of short-reach VCSEL-based MMF optical links," in *Latin America Optics and Photonics Conference*, OSA, 2016.

[111] A. Liu, P. Wolf, J. A. Lott, and D. Bimberg, "Vertical-cavity surface-emitting lasers for data communication and sensing," *Photonics Research*, vol. 7, no. 2, p. 121, 2019.

[112] M. M. P. Fard, C. Williams, G. Cowan, and O. Liboiron-Ladouceur, "High-speed grating-assisted all-silicon photodetectors for 850 nm applications," *Optics Express*, vol. 25, no. 5, p. 5107, 2017.

[113] M. Webster, L. Raddatz, I. White, and D. Cunningham, "A statistical analysis of conditioned launch for gigabit ethernet links using multimode fiber," *Journal of Lightwave Technology*, vol. 17, no. 9, pp. 1532–1541, 1999.

[114] L. Raddatz, I. White, D. Cunningham, and M. Nowell, “An experimental and theoretical study of the offset launch technique for the enhancement of the bandwidth of multimode fiber links,” *Journal of Lightwave Technology*, vol. 16, no. 3, pp. 324–331, 1998.

[115] T. Joseph and J. John, “Mode-field matched twin spot launch for enhancing data rates in multimode fibers,” in *2016 Twenty Second National Conference on Communication (NCC)*, IEEE, 2016.

[116] C. W. Oh, S. Moon, S. P. Veetil, and D. Y. Kim, “An angular offset launching technique for bandwidth enhancement in multimode fiber links,” *Microwave and Optical Technology Letters*, vol. 50, no. 1, pp. 165–168, 2007.

[117] B. J. Shastri, C. Chen, K. D. Choquette, and D. V. Plant, “Circuit modeling of carrier–photon dynamics in composite-resonator vertical-cavity lasers,” *IEEE Journal of Quantum Electronics*, vol. 47, no. 12, pp. 1537–1546, 2011.

[118] L. Vincetti and L. Rosa, “A simple analytical model for confinement loss estimation in hollow-core tube lattice fibers,” *Optics Express*, vol. 27, no. 4, p. 5230, 2019.

[119] A. Amphawan, F. Payne, D. O'Brien, and N. Shah, “Derivation of an analytical expression for the power coupling coefficient for offset launch into multimode fiber,” *Journal of Lightwave Technology*, vol. 28, no. 6, pp. 861–869, 2010.

[120] A. Spalvieri, P. Boffi, S. Pecorino, L. Barletta, M. Magarini, A. Gatto, P. Martelli, and M. Martinelli, “Analog nonlinear MIMO receiver for optical mode division multiplexing transmission,” *Optics Express*, vol. 21, no. 21, p. 25174, 2013.

[121] N. Sheffi and D. Sadot, “Energy-efficient VCSEL array using power and offset allocation of spatial multiplexing in graded-index multimode fiber,” *Journal of Lightwave Technology*, vol. 35, no. 11, pp. 2098–2108, 2017.

[122] W. Zhou, D. Gong, Q. Sun, D. Guo, G. Huang, K. Jin, C. Liu, J. Liu, T. Liu, M. Qi, X. Sun, J. Thomas, L. Xiao, and J. Ye, “LOCld65, a dual-channel VCSEL driver ASIC for detector front-end readout,” *IEEE Transactions on Nuclear Science*, vol. 66, no. 7, pp. 1115–1122, 2019.

[123] J. Lavrencik, J. S. Gustavsson, E. Haglund, A. Larsson, and S. E. Ralph, “Optimum VCSEL apertures for high-speed multimode fiber links,” in *Optical Fiber Communication Conference*, OSA, 2018.

[124] D. Molin, M. Bigot-Astruc, and P. Sillard, “Chromatic dispersion compensation in regular and bend-insensitive multimode fibers,” in *Optical Fiber Communication Conference*, OSA, 2012.

[125] G. R. Hadley, “Effective index model for vertical-cavity surface-emitting lasers,” *Optics Letters*, vol. 20, no. 13, p. 1483, 1995.

[126] G. Sialm, D. Lenz, D. Erni, G.-L. Bona, C. Kromer, M. Jungo, T. Morf, F. Ellinger, and H. Jackel, "Comparison of simulation and measurement of dynamic fiber-coupling effects for high-speed multimode VCSELs," *Journal of Lightwave Technology*, vol. 23, no. 7, pp. 2318–2330, 2005.

[127] A. W. Snyder and J. Love, *Optical waveguide theory.* Springer Science & Business Media, 2012.

[128] H. Kogelnik and T. Li, "Laser beams and resonators," *Applied Optics*, vol. 5, no. 10, p. 1550, 1966.

[129] A. Gerrard and J. M. Burch, *Introduction to matrix methods in optics.* Dover Publications, 2012.

[130] S. Tripathi, A. Kumar, R. Varshney, Y. Kumar, E. Marin, and J.-P. Meunier, "Strain and temperature sensing characteristics of single-mode–multimode–single-mode structures," *Journal of Lightwave Technology*, vol. 27, no. 13, pp. 2348–2356, 2009.

[131] R. Olshansky and D. B. Keck, "Pulse broadening in graded-index optical fibers," *Applied Optics*, vol. 15, no. 2, p. 483, 1976.

[132] G. Yabre, "Comprehensive theory of dispersion in graded-index optical fibers," *Journal of Lightwave Technology*, vol. 18, no. 2, pp. 166–177, 2000.

[133] J. M. Castro, R. Pimpinella, B. Kose, and B. Lane, "Investigation of the interaction of modal and chromatic dispersion in VCSEL–MMF channels," *Journal of Lightwave Technology*, vol. 30, no. 15, pp. 2532–2541, 2012.

[134] J. Castro, R. Pimpinella, B. Kose, and B. Lane, "Mode partition noise and modal-chromatic dispersion interaction effects on random jitter," *Journal of Lightwave Technology*, vol. 31, no. 15, pp. 2629–2638, 2013.

[135] S. Bottacchi, *Noise and Signal Interference in Optical Fiber Transmission Systems*. John Wiley & Sons, Ltd, 2008.

[136] R. Olshansky and S. M. Oaks, "Differential mode attenuation measurements in graded-index fibers," *Applied Optics*, vol. 17, no. 11, p. 1830, 1978.

[137] K. Balemarthy, A. Polley, and S. E. Ralph, "Electronic equalization of multikilometer 10-Gb/s multimode fiber links: Mode-coupling effects," *Journal of Lightwave Technology*, vol. 24, no. 12, pp. 4885–4894, 2006.

[138] X. Jin, A. Gomez, K. Shi, B. C. Thomsen, F. Feng, G. S. D. Gordon, T. D. Wilkinson, Y. Jung, Q. Kang, P. Barua, J. Sahu, S. ul Alam, D. J. Richardson, D. C. O'Brien, and F. P. Payne, "Mode coupling effects in ring-core fibers for space-division multiplexing systems," *Journal of Lightwave Technology*, vol. 34, no. 14, pp. 3365–3372, 2016.

[139] G. Paiano and M. Pellicoro, "Closed WKB formulas for weakly guiding optical fibers," *Journal of Lightwave Technology*, vol. 21, no. 1, pp. 286–292, 2003.

[140] B. Kose, J. Castro, R. Pimpinella, P. Huang, F. Jia, and B. Lane, "characterization of modal-chromatic dispersion compensation in 400gbase-sr8 channels," OSA, 2020.

[141] I. S. Gradshteyn and I. M. Ryzhik, *Tables of Integrals, Series, and Products.* Academic Press, 2014.

[142] J. Martin-Regalado, F. Prati, M. S. Miguel, and N. Abraham, "Polarization properties of vertical-cavity surface-emitting lasers," *IEEE Journal of Quantum Electronics*, vol. 33, no. 5, pp. 765–783, 1997.

[143] M. E. Brinson and S. Jahn, "Qucs: A GPL software package for circuit simulation, compact device modelling and circuit macromodelling from DC to RF and beyond," *International Journal of Numerical Modelling: Electronic Networks, Devices and Fields*, vol. 22, no. 4, pp. 297–319, 2009.

[144] M. Conforti, C. M. Arabi, A. Mussot, and A. Kudlinski, "Fast and accurate modeling of nonlinear pulse propagation in graded-index multimode fibers," *Optics Letters*, vol. 42, no. 19, p. 4004, 2017.

[145] N. Ledentsov, Ł. Chorchos, V. Shchukin, V. Kalosha, J. P. Turkiewicz, and N. N. Ledentsov, “Development of VCSELs and VCSEL-based links for data communication beyond 50Gb/s,” in *Optical Fiber Communication Conference (OFC) 2020*, OSA, 2020.

[146] W. Miao, S. D. Lucente, J. Luo, H. Dorren, and N. Calabretta, “Low latency and efficient optical flow control for intra data center networks,” *Optics Express*, vol. 22, no. 1, p. 427, 2014.

[147] C. Williams, G. Zhang, R. Priti, G. Cowan, and O. Liboiron-Ladouceur, “Modal crosstalk in silicon photonic multimode interconnects,” *Optics Express*, vol. 27, no. 20, p. 27712, 2019.

[148] Y. Fazea and V. Mezhuyev, “Selective mode excitation techniques for mode-division multiplexing: A critical review,” *Optical Fiber Technology*, vol. 45, pp. 280–288, 2018.

[149] C. Xia, G. Tong, X. Zhao, and J. Zhu, “Vortex mode excitation in a multimode fiber by the Laguerre-Gaussian laser beams,” *Optical and Quantum Electronics*, vol. 51, no. 8, pp. 1–9, 2019.

[150] Z. Guo, Z. Wang, M. I. Dedo, and K. Guo, “The orbital angular momentum encoding system with radial indices of laguerre–gaussian beam,” *IEEE Photonics Journal*, vol. 10, no. 5, pp. 1–11, 2018.

[151] L. G. Wright, Z. M. Ziegler, P. M. Lushnikov, Z. Zhu, M. A. Eftekhar, D. N. Christodoulides, and F. W. Wise, "Multimode nonlinear fiber optics: massively parallel numerical solver, tutorial, and outlook," *IEEE Journal of Selected Topics in Quantum Electronics*, vol. 24, no. 3, pp. 1–16, 2018.

[152] T. Becker, O. Ziemann, R. Engelbrecht, and B. Schmauss, "Optical strain measurement with step-index polymer optical fiber based on the phase measurement of an intensity-modulated signal," *Sensors*, vol. 18, no. 7, p. 2319, 2018.

[153] T. Chen, Q. Zhang, Y. Zhang, X. Li, H. Zhang, and W. Xia, "All-fiber passively mode-locked laser using nonlinear multimode interference of step-index multimode fiber," *Photonics Research*, vol. 6, no. 11, pp. 1033–1039, 2018.

[154] P. Pepeljugoski, "Dynamic behavior of mode partition noise in multimode fiber links," *Journal of lightwave technology*, vol. 30, no. 15, pp. 2514–2519, 2012.

[155] M. S. Kim, B. G. Kim, S. H. Bae, and Y. C. Chung, "Effects of multi-level format in MMF system based on mode-field matched center-launching technique," *IEEE Photonics Technology Letters*, vol. 30, no. 22, pp. 1972–1975, 2018.

[156] Y. Yue, Y. Yan, N. Ahmed, J.-Y. Yang, L. Zhang, Y. Ren, H. Huang, K. M. Birnbaum, B. I. Erkmen, S. Dolinar, *et al.*, "Mode properties and propagation effects of optical orbital angular momentum (OAM) modes in a ring fiber," *IEEE Photonics Journal*, vol. 4, no. 2, pp. 535–543, 2012.

[157] A. Trichili, K.-H. Park, M. Zghal, B. S. Ooi, and M.-S. Alouini, “Communicating using spatial mode multiplexing: Potentials, challenges, and perspectives,” *IEEE Communications Surveys & Tutorials*, vol. 21, no. 4, pp. 3175–3203, 2019.

[158] G. Goubau and F. Schwering, “On the guided propagation of electromagnetic wave beams,” *IRE Transactions on Antennas and Propagation*, vol. 9, no. 3, pp. 248–256, 1961.

[159] J. Nishizawa and I. Sasaki, “Focusing fiber with some inhomogeneity in radial direction,” *Japanese Patent Appl*, vol. 39064040.

[160] A. Amphawan, “Holographic mode-selective launch for bandwidth enhancement in multimode fiber,” *Optics express*, vol. 19, no. 10, pp. 9056–9065, 2011.

[161] M. A. Rakha, A. K. Rathie, and P. Chopra, “On some new contiguous relations for the Gauss hypergeometric function with applications,” *Computers & Mathematics with Applications*, vol. 61, no. 3, pp. 620–629, 2011.

[162] H. Bateman, *Higher transcendental functions [volumes i-iii]*, vol. 1. McGraw-Hill Book Company, 1953.

[163] R. J. LeVeque, *Finite difference methods for ordinary and partial differential equations: steady-state and time-dependent problems.* SIAM, 2007.

[164] Y.-C. Lu, L. Yang, W.-P. Huang, and S.-S. Jian, “Improved full-vector finite-difference complex mode solver for optical waveguidesof circular symmetry,” *Journal of lightwave technology*, vol. 26, no. 13, pp. 1868–1876, 2008.

[165] G. Grau, O. Leminger, and E. Sauter, “Mode excitation in parabolic index fibres by gaussian beams,” *Archiv Elektronik und Uebertragungstechnik*, vol. 34, pp. 259–265, 1980.

[166] “IEEE standard for floating-point arithmetic,” *IEEE Std*, vol. 754, no. 2019, pp. 1–70, 2019.

[167] L.-G. Zei, S. Ebers, and J.-R. Kropp, “Noise performance of multimode VCSELs,” *Journal of Lightwave Technology*, vol. 19, no. 6, p. 884, 2001.

[168] S. E. Hashemi, “Relative intensity noise (RIN) in high-speed VCSELs for short reach communication,” Master’s thesis, 2012.

[169] J. Lavrencik, S. K. Pavan, V. A. Thomas, and S. E. Ralph, “Noise in VCSEL-based links: Direct measurement of VCSEL transverse mode correlations and implications for MPN and RIN,” *Journal of Lightwave Technology*, vol. 35, no. 4, pp. 698–705, 2016.

[170] J. Castro, R. Pimpinella, B. Kose, and B. Lane, “The interaction of modal and chromatic dispersion in VCSEL based multimode fiber channel links and its effect on mode partition noise,” *Proceedings of the 61 IWCS 2012*, 2012.

[171] K. Sato and H. Toba, “Reduction of mode partition noise by using semiconductor optical amplifiers,” *IEEE Journal of Selected Topics in Quantum Electronics*, vol. 7, no. 2, pp. 328–333, 2001.

[172] S.-H. Yoo, S.-R. Moon, M. Kye, and C.-H. Lee, “Reduction of mode partition noise of FP-LD by using Mach-Zehnder interferometer for RSOA-based DWDM applications,” *Optics express*, vol. 24, no. 13, pp. 14494–14505, 2016.

[173] V. Vujicic, A. P. Anthur, A. Saljoghei, V. Panapakkam, R. Zhou, Q. Gaimard, K. Merghem, F. Lelarge, A. Ramdane, and L. P. Barry, “Mitigation of relative intensity noise of quantum dash mode-locked lasers for PAM4 based optical interconnects using encoding techniques,” *Optics express*, vol. 25, no. 1, pp. 20–29, 2017.

[174] M. E. Chaibi, L. Bramerie, S. Lobo, and C. Peucheret, “Mitigation of mode partition noise in quantum-dash fabry-perot mode-locked lasers using manchester encoding and balanced detection,” *Optics express*, vol. 25, no. 14, pp. 16300–16309, 2017.

[175] K. Ogawa, “Analysis of mode partition noise in laser transmission systems,” *IEEE Journal of Quantum electronics*, vol. 18, no. 5, pp. 849–855, 1982.

[176] J. Petrilla, “Example MMF link model,” in *IEEE 802.3 bm 40Gb/s and 100Gb/s Fiber Optic Task Force*, 2012.

[177] J. Castro, R. Pimpinella, B. Kose, and B. Lane, “Advances in characterization of the VCSEL mode partition noise penalty in optical fiber channels,” in *Optical Fiber Communication Conference*, pp. Th2A–13, Optical Society of America, 2014.

[178] Y. Liu, L. Ma, W. Xiao, R. Wang, J. Xiong, J. Luo, and Z. He, “Wideband multimode fiber with an optimized core size and fluorine-doped cladding for high-speed SWDM and CWDM transmission,” *Optics express*, vol. 27, no. 11, pp. 15433–15443, 2019.

[179] P. Sillard, D. Molin, M. Bigot-Astruc, A. Amezcua-Correa, K. de Jongh, and F. Achten, “DMGD-compensated links,” in *2017 Optical Fiber Communications Conference and Exhibition (OFC)*, pp. 1–3, IEEE, 2017.

[180] C. Liang, W. Zhang, S. Yao, Q. Wang, and Z. He, “Optical equalization using spatial phase manipulation for VCSEL-MMF based links,” in *CLEO: Science and Innovations*, pp. STh4B–2, Optical Society of America, 2018.

[181] B. Franz and H. Bulow, “Experimental evaluation of principal mode groups as high-speed transmission channels in spatial multiplex systems,” *IEEE photonics technology letters*, vol. 24, no. 16, pp. 1363–1365, 2012.

[182] C.-Y. Huang, C.-T. Tsai, J.-H. Weng, C.-H. Cheng, H.-Y. Wang, C.-H. Wu, M. Feng, and G.-R. Lin, “Temperature and noise dependence of tri-mode VCSEL carried 120-Gbit/s QAM-OFDM data in back-to-back and OM5-MMF links,” *Journal of Lightwave Technology*, vol. 38, no. 24, pp. 6746–6758, 2020.

[183] R. Hui and M. O'Sullivan, *Fiber optic measurement techniques.* Academic Press, 2009.

[184] G. Blanchette, M. S. Nezami, D. Rolston, and B. Reid, "Intra-satellite optical interconnect space market and technical challenges," in *Optical Interconnects XX*, vol. 11286, p. 1128604, International Society for Optics and Photonics, 2020.

[185] K. Benyahya, C. Simonneau, A. Ghazisaeidi, N. Barré, P. Jian, J.-F. Morizur, G. Labroille, M. Bigot, P. Sillard, J. Renaudier, and G. Charlet, "14.5 Tb/s mode-group and wavelength multiplexed direct detection transmission over 2.2 km OM2 fiber," in *2017 European Conference on Optical Communication (ECOC)*, pp. 1–3, 2017.

[186] G. Rademacher, B. J. Puttnam, R. S. Luís, T. A. Eriksson, N. K. Fontaine, M. Mazur, H. Chen, R. Ryf, D. T. Neilson, P. Sillard, F. Achten, Y. Awaji, and H. Furukawa, "1.01 Peta-bit/s C+L-band transmission over a 15-mode fiber," in *2020 European Conference on Optical Communications (ECOC)*, pp. 1–4, 2020.

[187] G. B. Arfken and H.-J. Weber, *Mathematical methods for physicists.* Elsevier Academic, 2005.